Thermoplastic Polymer Nanocomposites

by

Mahesh Baburao Parit

A thesis submitted to the Graduate Faculty of
Auburn University
in partial fulfillment of the
requirements for the Degree of
Master of Science

Auburn, Alabama
December 10, 2016

Keywords: single-walled carbon nanotubes, cellulose nanocrystals, spray freeze drying, polypropylene, poly(ethylene-co-vinyl alcohol), polylactic acid

Approved by

Virginia A. Davis, Chair, Alumni Professor of Chemical Engineering
Allan David, Assistant Professor of Chemical Engineering
James Radich, Assistant Professor of Chemical Engineering

Abstract

This thesis describes the use of non-covalent functionalization of nanomaterials and pre-processing methods for improving thermal and mechanical properties of melt processed thermoplastic polymer nanocomposites. The effects of non-covalent functionalization and pre-processing methods were studied for thermoplastic polymers: polypropylene (PP), poly(ethylene-co-vinyl alcohol) (EVOH) and polylactic acid (PLA); using a combination of morphology, thermal and rheological methods.

The effects of non-covalent functionalization and pre-processing methods were evaluated by incorporating polyvinylpyrrolidone (PVP) and sodium dodecyl sulfate (SDS) functionalized single-walled carbon nanotubes (SWNT) in polymer in conjunction with the rotary evaporation or spray freeze drying methods employed prior to melt processing. The initial investigation of PP nanocomposites through rotary evaporation method revealed that the PVP functionalized SWNT dispersed poorly in the PP matrix compared to pristine SWNT. This was the result of the incompatibility between the dispersing agent and polymer matrix as well as the aggregation caused by capillary and van der Waals forces during rotary evaporation. SWNT dispersion state was slightly improved in the case of PP/SDS-SWNT, due to compatibility between SDS and PP. On the other hand, the spray freeze drying method produced porous nanotube bundles reducing the aggregation effect of capillary and van der Waals forces and resulted in a more uniform dispersion state of SWNT in PP as well as EVOH nanocomposites. Consequently, significant changes in thermal and rheological properties of PP and EVOH nanocomposites were observed. For 0.75

vol.% PP/SDS-SWNT, largest increase of 38 °C was observed in thermal degradation temperature along with maximum increase (~3 orders of magnitude) in storage modulus. 0.75 vol.% EVOH/PVP-SWNT showed similar increase in storage modulus. Moreover, a noticeable difference between storage modulus and complex viscosity of EVOH/PVP-SWNT and EVOH/SWNT was observed as a result of the compatibility between PVP and EVOH.

Direct comparison of spray freeze drying with some other promising pre-processing methods (including masterbatch mixing, spray drying, and freeze drying) was carried out for PLA/cellulose nanocrystals (CNC) nanocomposites. Poor dispersion of CNC in PLA using spray drying and freeze drying methods did not cause any noticeable change in rheological behavior of PLA. Improved dispersion state of spray freeze dried CNC in PLA caused a larger increase in storage modulus compared to other pre-processing methods which further showed the effectiveness of spray freeze drying method. Additionally, it further demonstrated that the extent of changes in rheological properties of nanocomposites did not necessarily correlate with the changes in their thermal properties.

The results of this research highlight the importance of spray freeze drying as a pre-processing method for producing melt processed nanocomposites and its effectiveness in translating the uniform dispersion of non-covalently functionalized/pristine nanomaterials in solvent to final nanocomposites.

Acknowledgements

First, I would like to thank Dr. Virginia Davis for providing me with the opportunity to chase my curiosities within this research and for providing critical suggestions which helped me to improve as a graduate researcher. Additionally, I would like to thank my committee members for providing both their time and knowledge in the preparation and critical review of this manuscript.

I am also thankful to Nano to Micro research group members Joyanta Goswami, Partha Saha, Sara Grace Simpson, Alexander Haywood, and Matt Noor for all their help and good times during lab. I would like to thank Dr. Edward Davis for his help in research with regards to characterization. I would also like to thank Dr.Yoon Lee for granting access to equipment that was crucial in this research.

I am very grateful to my parents and brother for their constant moral support and encouragement throughout my stay at Auburn, Alabama.

Table of Contents

List of Figures

List of Tables

Chapter 1

Introduction

The purpose of this research is to understand how non-covalent functionalization and pre-processing methods affect the thermal and mechanical properties of thermoplastic polymer nanocomposites. The following specific systems were explored; single-walled carbon nanotubes (SWNT) in polypropylene (PP) and poly(ethylene-co-vinyl alcohol) (EVOH), and cellulose nanocrystals (CNC) in polylactic acid (PLA). Thermoplastics, polymers that can be reformed by melting, are used in a wide array of everyday applications, such as packaging materials, kitchen appliances, toys, containers, and numerous consumer products [1-3]. The incorporation of nanomaterials such as single-walled carbon nanotubes (SWNT) and cellulose nanocrystals (CNC) into thermoplastics has the potential to improve their thermal and mechanical properties of thermoplastics. Such improvements could enable their use in a broad range of high performance applications. Potential applications include light weight and high strength materials for the automobile parts such as bumpers, fascia, door trims, instrument panels, consoles etc., wear resistant artificial turfs, biocompatible and high strength materials for surgical implants, and tanks with better strength and improved barrier properties for fuel storage [4-10].

The three polymers used in this research, polypropylene (PP), poly(ethylene-co-vinyl alcohol) and polylactic acid have distinct properties and potential applications. PP is one of the most widely used thermoplastics [6, 11], EVOH is used in many barrier applications including fuel

tanks[5, 12, 13], and PLA is of increasing interest in a number of markets because it is produced from natural materials and is biodegradable [4, 9, 14, 15]. To date, much of the thermoplastic nanocomposite research has focused on dry mixing pristine or covalently functionalized nanomaterials and polymers prior to melt processing [16-21]. In contrast, this research focused on understanding the effects of non-covalent SWNT functionalization, CNC surface-modification, and the rotary evaporation (RE) and spray freeze drying (SFD) pre-processing methods on nanomaterial dispersion and nanocomposite properties.

Investigation of non-covalent SWNT functionalization focused on the use of polyvinylpyrrolidone (PVP) and sodium dodecyl sulfate (SDS). PVP is one of the best-known polymers for improving SWNT dispersion in water and is a promising choice for improving the dispersion state of SWNT in PP and EVOH nanocomposites. Additionally, it is inexpensive and biocompatible. As shown by O'Connell et al. [22], PVP interacts with SWNT due to a hydrophobic effect and CH-π interactions; such non-covalent interactions between the PVP and SWNT have been shown to be tight and uniform over the nanotube surface. SDS was used due to its low molecular weight and possible compatibility with polypropylene. SWNT were non-covalently functionalized by employing the procedure used by Kayatin et al. for PVP [23] with some modifications to meet the scale-up requirements for producing PP and EVOH nanocomposites. Surface modified CNC as well as CNC-PEO masterbatches were used for producing PLA nanocomposites. Low molecular weight PEO acts as miscible carrier for CNC in PLA matrix. PEO-CNC masterbatches were produced using the method described and used by Arias et al. [24].

Pre-processing using RE was based on the promising results by Radhakrishnan et al. [16, 25, 26]. Compared to dry mixing and the complicated hot coagulation method, the RE method was able to improve the dispersion state of SWNT in polypropylene without causing any degradation

or necessitating the use of large quantities of dichlorobenzene [25]. SFD was chosen based on the results by Khoshkava et al. [27]. They reported significant improvements in rheological properties of PP and PLA nanocomposites using spray freeze dried CNC. All nanocomposites were prepared through melt extrusion using a counter rotating Haake minilab twin screw extruder and were characterized by a combination of morphological, rheological, and thermal methods. Additionally, PLA/CNC nanocomposite filaments were produced to make nanocomposite structures through fused deposition modeling (FDM).

This thesis is organized as follows. Chapter 2 contains background information on SWNT, CNC, thermoplastic polymers, nanomaterial functionalization and dispersion, pre-processing methods, FDM additive manufacturing and characterization techniques. Chapter 3 provides information on materials, experimental details, and sample characterization. Chapter 4 discusses the effects of non-covalent functionalization of SWNT and pre-processing methods on polypropylene nanocomposites. Chapter 5 explains spray freeze dried PVP functionalized SWNT and poly (ethylene-co-vinyl alcohol) nanocomposites. Chapter 6 compares PLA/CNC nanocomposites as prepared through different pre-processing methods. Finally, Chapter 7 provides conclusions and suggestions for future research.

Chapter 2

Background

This chapter provides the general background information regarding topics relevant in this research. Topics covered include materials, dispersion and functionalization of carbon nanotubes, polymer processing, spray freeze drying, methods of characterization.

2.1 Materials

2.1.1 Carbon nanotubes

The discovery of carbon nanotubes (CNT) is often attributed to Iijima in 1991 [28]; however, some sources cite that they were discovered by Bethune at IBM [29]. Additionally, TEM (transmission electron microscopy) evidence of tubular, nanosized carbon filaments was reported by Russian scientists, Radushkevich and Lukyanovich, in 1952 [29, 30]. CNT are long cylinders of sp^2 hybridized carbon atoms covalently bonded to each other. They are classified as single-walled carbon nanotubes (SWNT), double-walled carbon nanotubes (DWNT), or multi-walled carbon nanotubes (MWNT), depending on whether they are made up of one, two, or multiple coaxial cylinders, respectively. A SWNT can be described as a graphene sheet rolled up into a one-dimensional cylinder. SWNT typically have a diameter of approximately 0.5 - 2 nanometers and lengths that range from hundreds of nanometers to a few microns. Their small size, large specific surface area, stiffness, and robust carbon-carbon bonds result in extraordinary thermal, mechanical

and electronic properties. Table 2.1 compares various properties of SWNT with several other nanomaterials.

The thermal conductivity of an individual SWNT is more than 3000 W/K·m, which is higher than that of diamond and basal plane of graphite (both 2000 W/K·m) [31, 32]. The Young's modulus and tensile strength for an individual nanotube, calculated based on the normalized applied force per nanotube are ~0.64 TPa and ~37 GPa, respectively. These values are close to Young's modulus of ~ 0.66 TPa obtained for silicon carbide nanofiber and tensile strength of ~53 GPa for silicon carbide nanorods. However, density-normalized modulus and strength of SWNT, which are important for applications requiring strong and light structural materials are ~2.4 and ~1.7 times that of silicon carbide nanorods and ~19 and ~56 times that of steel wire, respectively [33-36].

Property	**Carbon fibers**	**VGCF**	**MWNT**	**SWNT**
Diameter (nm)	7k - 10k	50-200	10-50	1-2
Length (μm)	> 1k	10-100	10-50	1-5
Surface area (m^2/gm)	~1000	20-30	300-400	1315
Density (gm/cm^3)	2-2.2	1.95	2.1	1.45
Tensile strength (GPa)	0.6-0.75	2.92	11-63	150-180
Modulus (GPa)	30-32	240	270-950	600-1200
Thermal conductivity (W/mK)	1000	1950	830	>3000
Electrical resistivity (Ω.cm)	10^{-5}	10^{-4}	10^{-4}	10^{-4}
Cost ($/gm)*	0.02	0.8	120	750

Table 2.1. Estimated or measured physical properties of carbon fibers, vapor grown carbon fibers (VGCF), MWNT and SWNT [16].

* Cost represented for research grades.

SWNT also possess excellent electric current carrying capacity due to their 1-dimensionality and long lengths. The electrical conductivity of nanotubes are highly dependent on their chiral angle [37]. The diameter of the nanotube is determined by the chiral vector [38]. The chiral vector C_h is defined in Equation 1 and is specified by n and m, a pair of integers with $0 \leq |m| \leq n$, and two unit cell base vectors of the graphene sheet $\mathbf{a}_1$ and $\mathbf{a}_2$, as shown in Figure 2.1.

$$\mathbf{C}_h = n\mathbf{a_1} + m\mathbf{a_2} \quad (1)$$

Depending on sheet rolling, a nanotube can be classified as zigzag, chiral, or armchair (Figure 2.1). If $m = 0$, then the resulting nanotube formed is zigzag. For example, a zigzag nanotube is formed if the origin (0, 0) is folded to meet another point (11, 0). If $n = m$, then the nanotube that forms is armchair. This is shown in Figure 2.1, wherein the origin (0, 0) is folded along the dotted line labeled "armchair" to meet a projected point (11, 11) not shown in the figure. All other tubes are classified as chiral nanotubes. The line labeled "H" indicates the direction of the closest hexagon rows to the tube axis. The angle between the tube axis T and H is the chiral angle (or wrapping angle Φ). Armchair nanotubes have a chiral angle of 0°, while zigzag nanotubes have a chiral angle of 30°. The chiral angle of chiral nanotubes ranges between 0° and 30°. Armchair nanotubes ($n = m$) are metallic in nature, as they have electronic bands crossing the Fermi level. For armchair nanotubes, the conduction and valence band overlap, and they are ballistic conductors (i.e., no scattering), providing excellent conduction with no heating [38, 39]. Chiral and zigzag nanotubes are generally considered metallic if they satisfy the condition $(n - m) = 3l$, where l is an integer; in reality, they have a very small band gap [40]. If they do not satisfy the condition then they are semiconducting with a band gap that is inversely proportional to the nanotube diameter [41]. Carbon nanotubes' unique combination of mechanical, thermal, and electrical properties make them attractive for a broad range of electronic, energy, and high strength material applications.

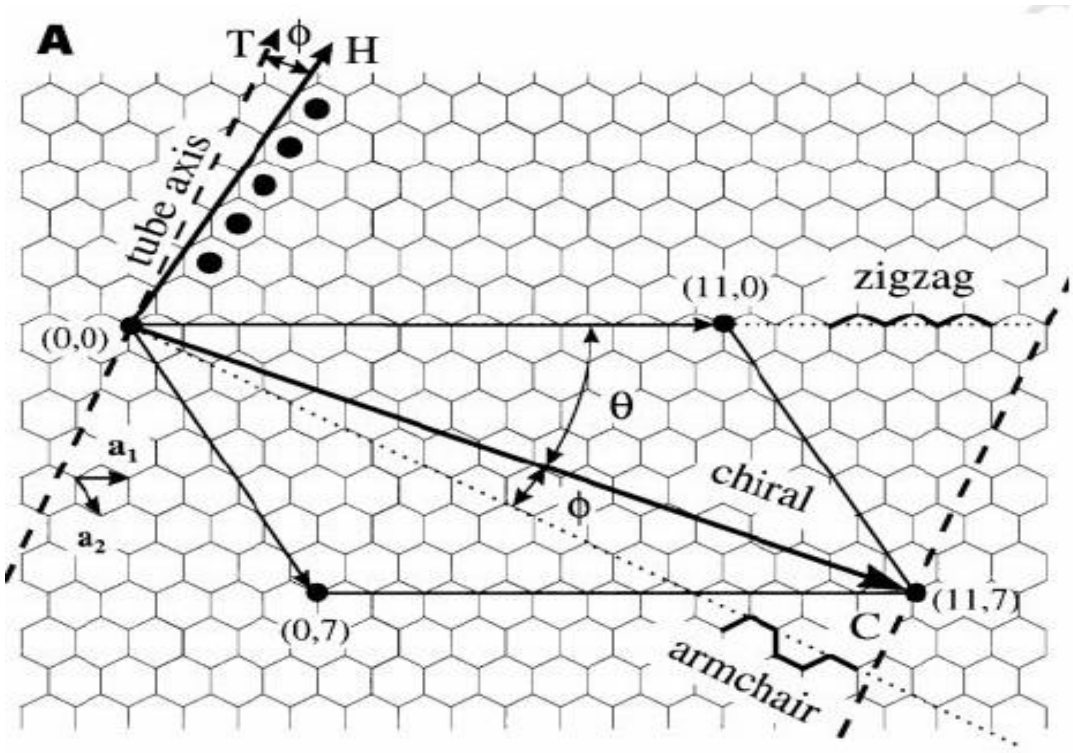

Figure 2.1. Construction of carbon nanotube from single graphene sheet [38].

2.1.2 Cellulose Nanocrystals

Cellulose nanocrystals (CNC) (also referred as whiskers, nanowhiskers or nanocrystalline cellulose) are abundant, renewable, bio-based materials contained in cellulose. The main sources for obtaining cellulose are plants; however, cellulose can also be produced from bacteria, algae, and some sea animals. CNC are inexpensive compared to many other nanomaterials including carbon nanotubes and nanofibers. CNC have Young's modulus of ~150 GPa, which is higher than glass fibers (~70 GPa) and within an order of magnitude of that of carbon nanotubes. They also have bending strength of ~10 GPa, which is $1/6^{th}$ of carbon nanotubes [42, 43].

CNC are synthesized using acid hydrolysis of cellulose, which preferentially removes amorphous regions of cellulose and extracts the CNC, as shown in Figure 2.2. Sulfuric acid and

hydrochloric acid have been extensively used for this purpose. CNC treated with hydrochloric acid have a limited ability for dispersing in an aqueous medium, and their aqueous suspension tends to flocculate. Conversely, CNC treated with sulfuric acid a have high dispersibility in water, due to the presence of negatively charged sulfate groups on its surface. The large solubility of CNC in an aqueous medium has utility in producing nanocomposites of water soluble polymers. However, it is challenging to achieve a homogeneous and uniform dispersion of CNC in hydrophobic polymer matrices [44]. Surface functionalization CNC is usually carried out to it improve its dispersion state in such polymers [45, 46]. Due to its biocompatibility, strength, and optical properties, CNC are widely used in fields such as biomedical engineering, material sciences, and electronics [47].

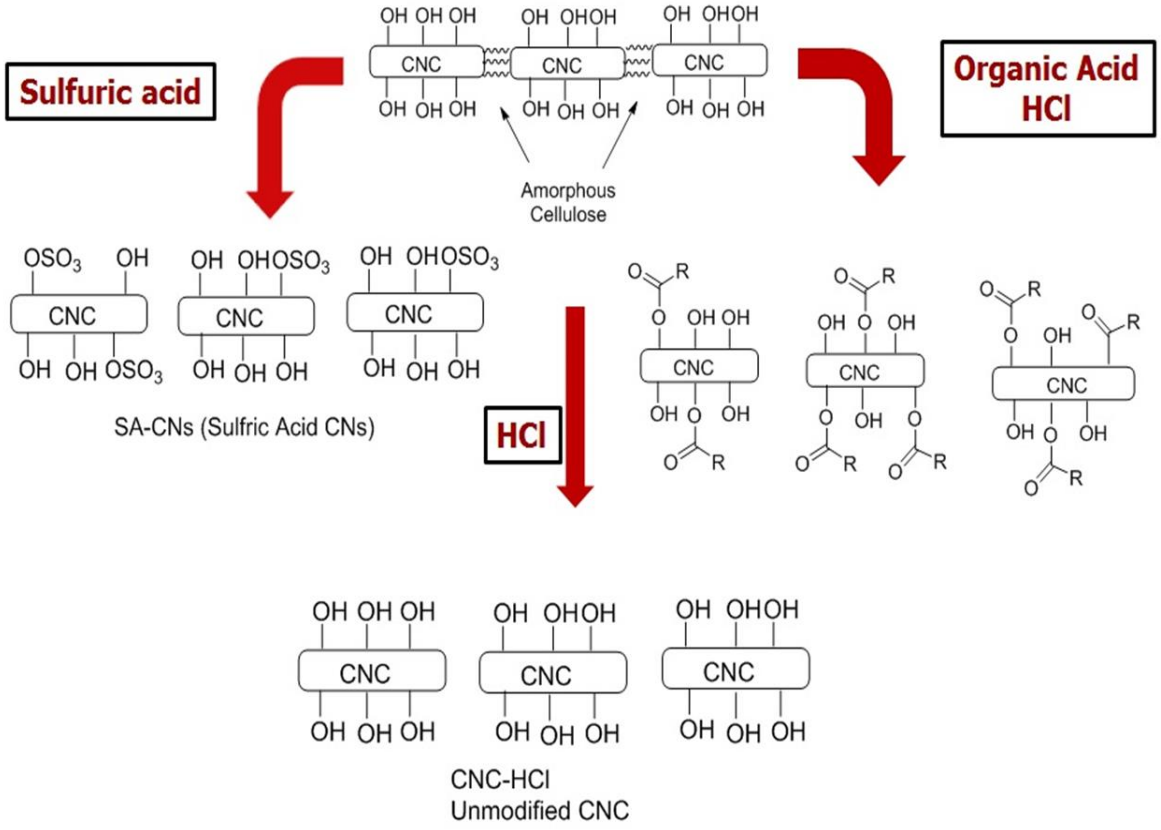

Figure 2.2. Modified and unmodified forms of cellulose nanocrystals produced from cellulose [48].

2.1.3 Polypropylene

Polypropylene is among the most widely-used thermoplastic polymer. As of 2015, the annual U.S production of polypropylene was ~20 billion pounds contributing a significant share in ~ 95 billion pounds overall annual thermoplastics production [11, 49]. Due to the wide range of molecular weights, diverse copolymer formations, significant stability after addition of stabilizers, and ease of processing, PP is one of the most widely-used thermoplastics [6]. It is used in a variety of applications, including food containers, kitchen appliances, toys, sports equipment, automobile parts, chemical tanks, and cable insulations. However, neat PP is not considered to be a high-performance polymer and cannot be used without modification in most high performance applications requiring enhanced thermal and mechanical properties [8, 50].

Polypropylene (PP) was first polymerized in 1955 by Natta et al. [51] from organo-metallic catalysts based on titanium and aluminum. The various forms of polypropylene are distinguished by tacticity—namely isotactic, syndiotactic, and atactic, as shown in Figure 2.3. Isotactic polypropylene is the most common commercial form of polypropylene. It has all the pendant methyl groups on the same side of the zigzag plane. Syndiotactic polypropylene has the pendant methyl group positioned alternatively on either side of the chain, while atactic polypropylene is classified by the random positioning of the pendant methyl group on either side of the chain.

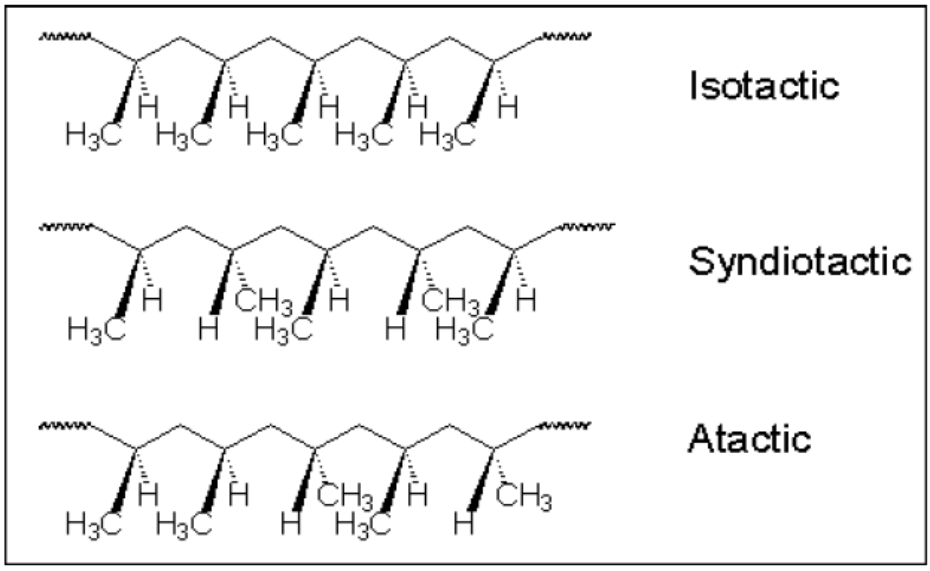

Figure 2.3. Stereo configurations of polypropylene: isotactic, syndiotactic, and atactic [52].

Isotactic polypropylene is more crystalline than other forms of PP. Higher crystallinity improves the mechanical properties of PP, giving it a tensile strength of ~30 MPa; however, loss of PP's mechanical properties can occur during processing, as result of degradation resulting in reduced molecular weight. Due to the presence of the tertiary hydrogen on the carbon atom bonded to the methyl group, the primary common mechanism of PP degradation is oxidation, a free radical chain reaction particularly during melt processing [53]. The presence of stress, heat, oxygen, or metal catalysts can result in hemolytic cleavage of the carbon-hydrogen or carbon-carbon bond, thus causing the formation of free radicals. The degradation chain reaction is propagated through the formation of a hydroperoxide, and it is accompanied by the formation other free radicals. In subsequent reactions, the hydroperoxide decomposes in the presence of heat or metal catalyst to form an alkoxy radical. Oxidative chain scission is believed to occur through the disintegration of this alkoxy radical. Oxidation in PP can be readily prevented by the use of antioxidants. Typically

two types antioxidants are used. Primary antioxidants act as free radical scavengers to prevent oxidation reactions; secondary antioxidants react with the hydroperoxide groups to convert them to non-radical products [54]. In addition, commercial PP may contain UV stabilizers and colorants for the purpose of improving its stability during use and slip agents for the purpose of reducing surface friction.

2.1.4 Poly(ethylene-co-vinyl alcohol)

Poly(ethylene-co-vinyl alcohol) (EVOH) is a semicrystalline copolymer of ethylene and vinyl alcohol; EVOH's structure is shown in Figure 2.4. Different EVOH grades possess different levels of ethylene and vinyl monomer contents. EVOH with lower ethylene mole % has a higher gas barrier, density, and melting point temperature, whereas EVOH with higher ethylene mole % provides greater flexibility and ease of processing.

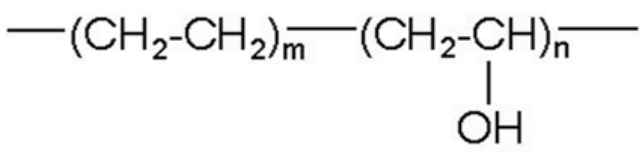

Figure 2.4. EVOH copolymer molecular structure [55].

EVOH provides the higher than most commodity thermoplastics—approximately 10,000 times that of polyethylene. Table 2.2 compares the transmission rates of gas through EVOH, polyethylene terephthalate (PET), and low-density polyethylene (LDPE). Figure 2.5 compares the oxygen transmission rates of EVOH with other barrier polymers. EVOH's primary application is in laminated gas barrier packaging films for containing and preserving food. It is also used in blow-molded or thermoformed rigid containers for a variety of storage purposes, including gasoline storage tanks for automobiles [56]. The excellent barrier properties of EVOH minimize fuel vapor permeation from fuel tanks, lines, and filler pipes, enabling manufacturers to comply with increasingly strict fuel vapor emission standards.

	Gas Transmission Rates at 0% RH (cm^3.20μm/m^2.day.atm)			
Films	N_2 (25°C)	O_2 (25°C)	CO_2 (25°C)	H_2 (25°C)
EVOH (32 mol% ethylene)	0.017	0.27	0.81	160
EVOH (44mol% ethylene)	0.13	1.23	7.1	410
PET	8	54	110	3100
LDPE	3100	12000	42000	28000

Table 2.2. Gas transmission rate comparison of EVOH grades with some commonly used thermoplastics [55] —PET and LDPE.

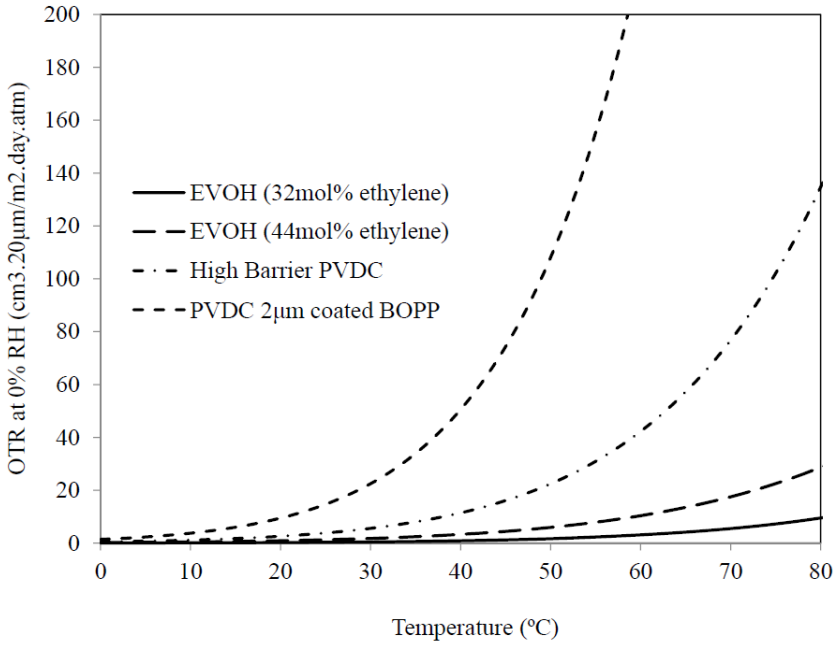

Figure 2.5. Oxygen transmission rate (OTR) of two EVOH grades with two other barrier polymers—polyvinylidene chloride (PVDC) and biaxially oriented polypropylene (BOPP) [55].

2.1.5 Polylactic acid

Polylactic acid (PLA) is a biodegradable thermoplastic aliphatic polyester derived from renewable resources, such as corn starch and sugarcane. The aliphatic polylactide structure is depicted in Figure 2.6. PLA is one of the polymers most widely used in fused deposition modeling, an additive manufacturing technology. Due to its biocompatibility, biodegradability, and relatively good mechanical and barrier properties, PLA is useful in a broad range of applications, especially in making packaging materials and biomedical devices [7, 57].

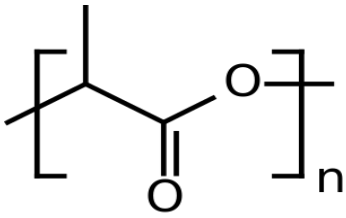

Figure 2.6. Polylactic acid monomer structure.

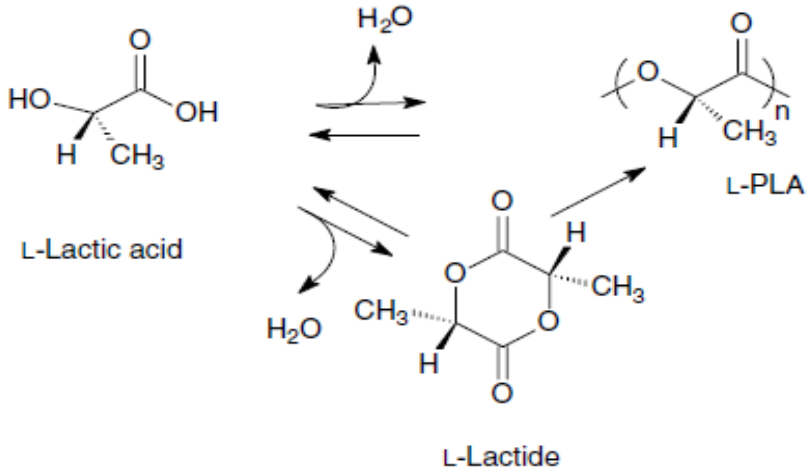

Figure 2.7. PLA synthesis routes [58].

PLA can be synthesized using two routes: direct condensation of lactic acid and ring-opening polymerization of the cyclic lactide dimer, as shown in Figure 2.7. Since the direct condensation route is an equilibrium reaction, removing trace amounts of water in later stages of polymerization is difficult and generally limits the ultimate molecular weight achievable by this approach. Therefore, ring opening polymerization is the preferred way of producing PLA industrially. This process uses ring opening of the lactide (cyclic dimmer of lactic acid) in the presence of a catalyst to obtain a high molecular weight of PLA. Ring opening polymerization consists of three steps: polycondensation of lactic acid monomers to low-molecular weight PLA,

depolymerization of the PLA into lactides, and polymerization of these lactides to produce larger PLA molecules using metal catalysts [58].

2.2 Dispersion and Functionalization of SWNT and CNC

Most carbon nanotube synthesis and purification methods result in micron- to millimeter-sized bundles and/or aggregates containing nanotubes of different lengths, diameters, and chiralities. In general, applications of SWNT (such as in conductive and high-strength nanocomposites, electronic devices, energy storage, and conversion devices) require them to be dispersed uniformly in a fluid, break free from aggregates, and remain in individual or small bundles. Moreover, SWNT that are monodisperse with respect to chirality, diameter, length, and electronic character are expected to provide the maximum performance in electronic applications [59]. However, SWNTs' high aspect ratio, strong intertube van der Waals attraction (20-40 k_bT/nm)[60, 61], and high stiffness make them difficult to disperse. This difficulty of dispersion can be reduced by employing mechanical methods and different functionalization schemes.

Mechanical methods include ultrasonication, ball milling, high speed stirring, extrusion, and calendaring. Ultrasonication is the most commonly used method to disperse nanotubes in a liquid medium, but can result in reductions in nanotube length or molecular weight degradation of other components in the fluid. Ultrasonication method uses implosion of cavitation bubbles to break up aggregates of nanotubes. Other methods predominantly apply high shear forces to assist in debundling and distributing nanotubes throughout the fluid phase.

SWNT functionalization can be used to create steric or electrostatic repulsion between SWNT and to improve thermodynamic compatibility with solvents and polymer matrices. There are two types of functionalization schemes: non-covalent and covalent. Non-covalent approaches

include the adsorption of a surfactant, biomacromolecule, or polymer on a nanotube surface. Covalent approaches include sidewall, defect site, and open end chemistries [62, 63].

In non-covalent approaches, the interaction between the dispersing agent and the carbon nanotube is mainly due to π-π overlapping of the conjugate system of the nanotubes and dispersing agent, while in some surfactants, non-specific hydrophobic interactions are exploited [64]. For example, surfactants such as sodium dodecyl sulfate (SDS) can form micelles around SWNT with their hydrophobic hydrocarbon tails facing hydrophobic sidewalls of SWNT. The surfactants then disperse them as individuals in certain concentrations, which is evident from spectral-based characterizations of ultrasonicated and centrifuged supernatants [61]. Adsorption of biomacromolecules (e.g., DNA, proteins) and polymers onto SWNT has been used to achieve dispersion and stabilization of carbon nanotubes with solubilities up to 0.36 mg/ml [22, 65-68]. Wrapping has been suggested to be thermodynamically favorable for DNA and polymers (e.g., polyvinylpyrrolidone, polystyrene sulfonate).

Covalent functionalization can be divided into two categories: end/defect site functionalization and sidewall functionalization. End and defect site covalent functionalizations take advantage of the fact that nanotubes are more reactive at the ends and at defect sites; π-orbital misalignment between carbon atoms at these sites is one of the main causes for increased reactivity of CNT. Moreover, π-orbital misalignments are inversely proportional to the nanotube diameter, which further increases reactivity in smaller diameter nanotubes [69]. End and defect site covalent functionalizations are usually carried out under oxidizing acid media. Typically, mixtures of nitric and sulfuric acids are used to attach the acidic functionalities to the defect sites [70]. Oxidation can be a starting point for additional reactions intended for attaching species such as amides and

esters via chemical reactions or adsorption [71, 72]. Figure 2.8 shows the scheme of reactions carried out at end and defect sites.

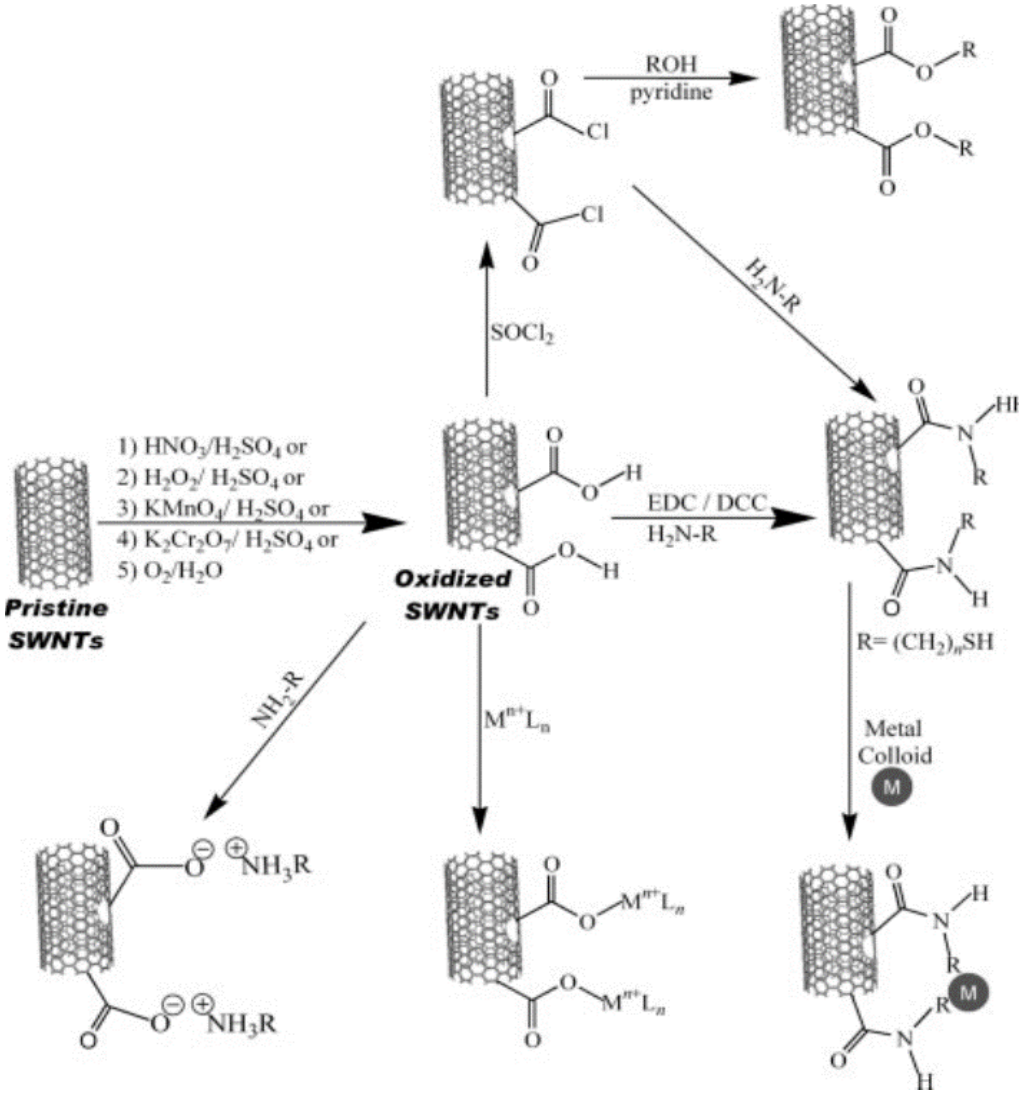

Figure 2.8. Schematic of common functionalization routes used to derivatize SWNT at end and defect sites [73].

Sidewall functionalization is an option to reduce the effect of the functionalization process on the nanotube length. Some of the more common sidewall functionalizations include esterification, fluorination, ozonolysis, and alkylation. For example, Billups reaction (Figure 2.9), one of the routes for reductive alkylation of SWNT, is carried out by using lithium in liquid ammonia, wherein the reduced nanotube salts react with alkyl halide groups to functionalize the nanotubes. A key advantage of the Billups reaction is that the lithium intercalates the SWNT bundles enabling separation and functionalization of individual SWNT. Billups functionalization typically results in one alkyl group attached to the sidewalls of the nanotube for every 17 to 35 carbon atoms [74]. Billups reaction is scalable and is convenient compared to other functionalization routes since it is carried out without sonication, thus maintains the aspect ratio of pristine SWNT.

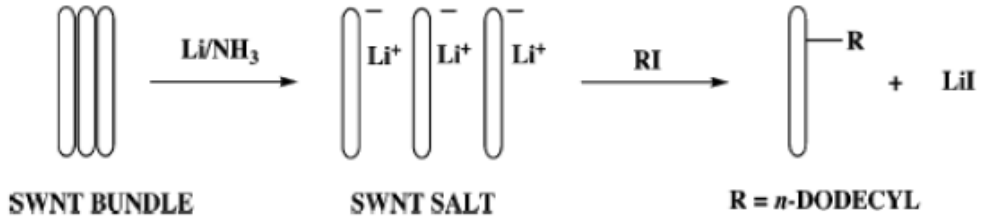

Figure 2.9. Reductive alkylation functionalization mechanism [74].

Another common route for sidewall functionalization is sidewall esterification of SWNT via Bingel reaction shown in Figure 2.10. In this reaction, SWNT bundles are broken up using bath sonication in 1,2 dichlorobenzene. These unbundled SWNT are functionalized using diethyl malonate, activated by an organic base [23]. A disadvantage of this scheme is that sonopolymer formed by the DCB can be very difficult to remove from the SWNT. Descriptions of additional functionalization schemes can be found in Banerjee et al. [75].

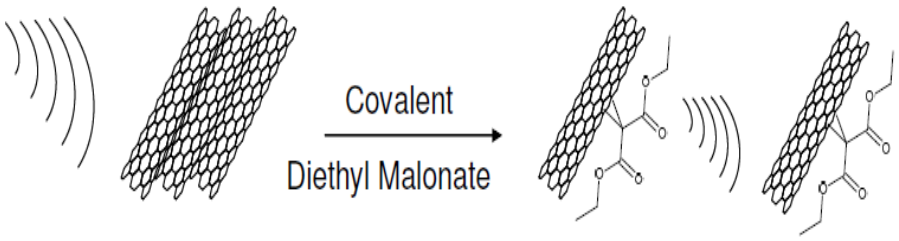

Figure 2.10. Reaction scheme of sidewall esterification of SWNT via Bingel reaction [23].

Cellulose nanocrystals are promising nanomaterial derived from the most abundant natural polymer cellulose. Functionalization can be used to facilitate dispersion and compatibility with specific solvents and polymer matrices including hydrophobic materials. Surface functionalization of CNC introduces stable negative or positive electrostatic charges on their surface to improve their dispersion in solvents; it can also tune surface energy characteristics of CNC to improve compatibility with nonpolar or hydrophobic polymer matrices in nanocomposites. Due to the presence hydroxyl groups on the surface of CNC, covalent functionalization schemes include esterification, hydrolysis, etherification, oxidation, silylation, and polymer grafting [76-79]. Figure 2.11 shows the esterification and hydrolysis reactions carried out at the hydroxyl groups of CNC. Fischer esterification of hydroxyl groups simultaneously with the hydrolysis of amorphous cellulose chains has been introduced as a viable one-pot reaction methodology which allows isolation of acetylated CNC in a single-step process [42]. Similarly, CNC produced using sulfuric acid hydrolysis introduce negatively charged sulfate groups on the surface of CNC which aids their dispersal in polar solvents.

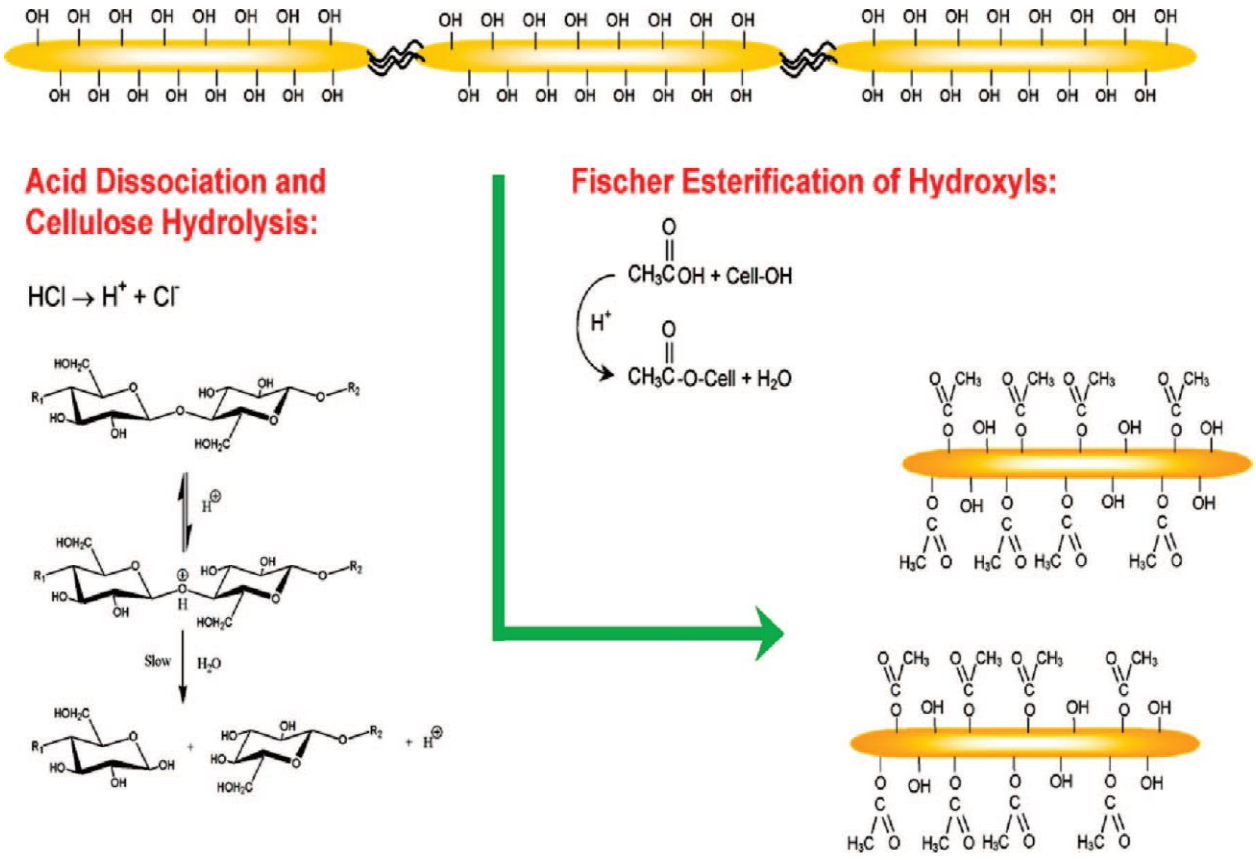

Figure 2.11. Reaction scheme illustrating the cellulose hydrolysis and esterification reactivity of hydroxyl groups [42]

2.3 Polymer Processing

The most common techniques for making nanocomposites are in situ polymerization, solution processing, and melt processing. In situ polymerization requires the dispersion of the nanomaterial in a monomer, followed by the polymerization of the monomers. For carbon nanotubes, sonication is often used to aide in the dispersion in a solvent [80, 81]. The sonicated nanotube suspension is then added to the monomer, where, in some cases, the nanotubes act as an initiator for

polymerization. Better interaction between nanotubes and polymers are achieved using this approach compared to other processing methods.

Solution mixing is executed in three steps. First, the nanomaterial and polymer are dispersed separately in a common solvent. Next, the nanotube suspension is mixed with the polymer solution. Finally, the composite is cast into a sheet, and the solvent is allowed to evaporate. Nanotube dispersion in the solvent and polymer solution is typically achieved by using ultrasonication, magnetic stirring, or high shear mixers.

The most commonly-used melt processing techniques include melt extrusion [18, 82], blow molding [83], and injection molding [84, 85]. Melt processing is used to mix molten polymers and nanomaterials and can be used to form nanocomposites. Typical melt processing methods involve melting followed by the incorporation of the nanomaterials and any other additives, with the aid of high shear.

2.4 Spray freeze drying

Spray freeze drying (SFD) is an atomization technique. It is different from spray drying in that it is carried out in a cryogenic medium. This technique consists of two main steps. Initially, an aqueous solution is atomized or sprayed directly into a cryogenic medium such as liquid nitrogen. This is followed by freeze drying the frozen slurry below the triple point of water. The typical schematic for cryogenic atomization is shown in Figure 2.12.

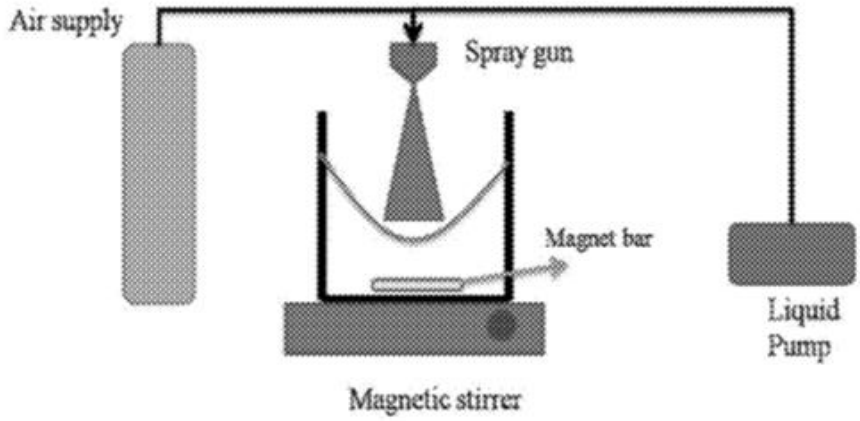

Figure 2.12**.** Schematic of typical cryogenic atomization in the spray freeze drying process [86].

This technique has been widely used in the food and pharmaceutical industries [87-89]. However, it had not been used for composites until recently. Khoshkava et al. used spray freeze drying of CNC dispersions to make PP/CNC composites through melt processing. The spray freeze dried CNC were highly porous compared to spray dried CNC (Figure 2.13) and had a lower agglomerate strength. Both of these factors assisted in easy melt infiltration of molten polymer into porous CNC agglomerates, thereby enhancing the dispersion state during processing. The resulting CNC dispersion state was more uniform than that achieved with other promising techniques, such as spray drying and freeze drying. As seen from a frequency sweep in Figure 2.14, three orders of magnitude increase in the storage modulus of polypropylene was found by using 5 wt.% spray freeze dried CNC. Moreover, the percolation threshold concentration was also significantly reduced, which is indicative of a higher aspect ratio, due to more finely dispersed CNC.

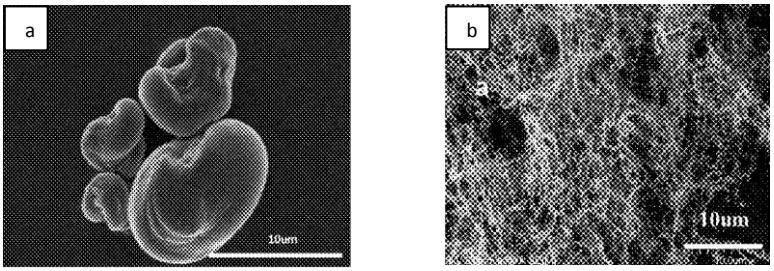

Figure 2.13. (a) Spray dried CNC lumps (b) porous structure of spray freeze dried CNC [86].

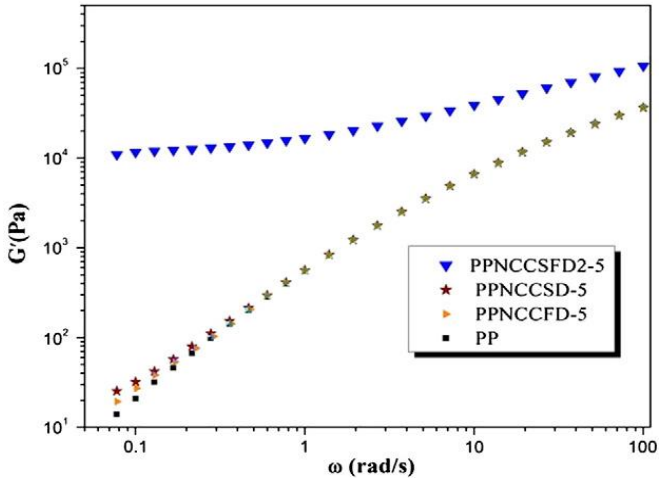

Figure 2.14. Storage modulus vs angular frequency plot for 5 wt.% PP/NCC composites using spray freeze drying (PPNCCSFD2), spray drying (PPNCCSD) and freeze drying (PPNCCFD) techniques [90].

2.5 Fused deposition modeling

Fused deposition modeling is a type of additive manufacturing used in the 3D printing of thermoplastic polymers to make three dimensional solid objects from computer aided design (CAD) models. 3D printing of thermoplastic materials is achieved using additive processes, where an object is created by laying down successive layers of this material. 3D printing is considered distinct from traditional machining techniques (subtractive processes), which rely mostly on the

removal of material by drilling, cutting, etc. 3D printing is usually performed by a materials printer using digital technology. This technology is being used in many fields including jewelry, footwear, industrial design, architecture, engineering, construction, automotive manufacturing, aerospace manufacturing, dental and medical industries, and civil engineering [91].

The schematic of a FDM-based 3D printer is shown in Figure 2.15. Parts are built layer by layer, from bottom to top by depositing the polymer on the base. The printer gets its signal from a computer where a special software cuts a CAD model into layers and calculates the way the printer's extruder should build each layer. The printer heats polymer between its melting point and glass transition temperature and extrudes it throughout the nozzle onto the base along the calculated path. The 3D printer's computer translates the dimensions of an object into X, Y, and Z coordinates and controls the calculated path that the nozzle and the base follow during printing. When the thin layer of plastic binds to the layer beneath it, it cools down and hardens. Once the layer is finished, the base is lowered to start building the next layer. With introduction of this 3D printing method, it became possible to build objects with complex geometries and cavities [92].

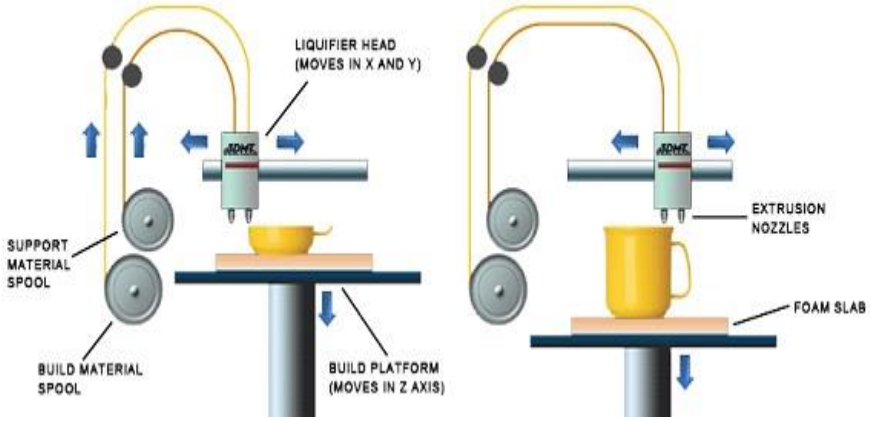

Figure 2.15**.** Schematic of FDM based 3D printer [91].

2.6 Methods of characterization

2.6.1 Ultraviolet-visible spectroscopy

Ultraviolet-visible (UV-vis) spectroscopy is an analytical tool used to detect molecular fingerprints based on the electronic transitions. The range of wavelength considered under UV-vis technique starts from the near UV range of 200-380 nm, and covers the entire visible range, 380-780 nm. The electronic transition involves the transition from ground levels to excitation levels. Transition occurs during the interaction with photons in the UV-Vis range having energy equal to the energy gap between the levels.

In the case of SWNT, the electronic transitions occur between the peaks of the density of states (electron residing levels) in the valence and conduction band [93]. These electronic transitions are responsive to the wavelengths in the visible and near infra-red range. It has been shown that the UV-vis spectra can assist in monitoring the aggregation state of SWNT in dispersion. Individually dispersed SWNT show a number of well-resolved peaks (van Hove singularities) in the visible-infra-red region [61, 94]. The intensities of the peaks indicate concentrations of the individually-dispersed SWNT [94]. The peaks observed in the UV-vis spectra can be used to determine chirality of the nanotubes based on the absorption energy using the Kataura plot. The metallic nanotubes have a higher energy gap between the van Hove singularities than the semiconducting nanotubes [93].

The intensities of UV-vis peaks can indicate the degree of dispersion of SWNT in a solvent due to its sonication and non-covalent functionalization. In this research, a Thermo Scientific Nanodrop 2000C UV-vis spectrometer was used for this purpose.

2.6.2 Thermogravimetric analysis -

Thermogravimetric analysis (TGA) measures the amount and rate of change in the weight of a material as a function of temperature or time in an air/inert atmosphere. Measurements are primarily used to determine the composition of materials and to predict their thermal stability. The thermal stability of polymer using TGA can be monitored by examining several criteria, such as the onset temperature, 50% weight loss temperature, or the temperature corresponding to maximum rate of weight% loss of polymer. In this work, 5% weight loss temperature and temperature corresponding to maximum rate of weight% loss were extracted from TGA data. The excellent thermal properties of carbon nanotubes (including their high thermal conductivity and high temperature stability) render them promising reinforcement materials to improve the thermal stability of polymers. The presence of nanotubes in the polymer matrix stabilizes the polymer chains at the interphase region against the thermal degradation, thereby improving the thermal stability of the polymer nanocomposite. Radhakrishnan et al. observed as much as a 27 $^{\circ}$C increase in the thermal degradation temperature for rotary evaporated PP/SWNT nanocomposites with 0.75 vol.% SWNT [26]. Non-covalently functionalized SWNT might improve dispersion state of SWNT in polymer matrix thus stabilizing more polymer chains at SWNT/polymer interphase and further improving thermal stability of polymer.

2.6.3 Differential scanning calorimetry

Differential scanning calorimetry is widely used to measure crystallization, glass transition, and melt temperature. It is also commonly used in the study of the crystallization kinetics of polymers. The device consists of two heaters, which are loaded with sealed pans—a sample pan containing the polymer and an empty reference pan. The two pans are heated at the same rate (usually 10 $^{\circ}$C/min) with high precision. A computer records the required heat input applied to the pans that is

necessary to maintain the specified heating rate. The melting and crystallization temperature is found using sharp peaks in the observed heat flow due to the absorption and release of heat, respectively.

In general, the incorporation of carbon nanotubes in polymer matrices can result in an increase in glass transition temperature, crystallization temperature, and melt temperature. Polymer crystallization occurs by a process referred to as "nucleation and chain growth." Nucleation can be thought of as the first step in the formation of crystals. In fact, nucleation is subdivided in to primary and secondary nucleation. The crystallite nuclei are formed as a result of variations in the order or density of the molten polymer during primary nucleation. These crystallite nuclei grow in size by further induction of polymer chains during secondary nucleation.

Primary nucleation can occur in two ways. If there is no surface on which the polymer chains can form nuclei, then the only option for nucleation is super-cooling the solution to enable spontaneous nucleation of the polymer crystals. This is referred to as homogeneous nucleation. On the other hand, in heterogeneous nucleation, the presence of impurities or nanomaterials in polymer solution provides new surfaces on which polymer chains can facilitate nucleation. The addition of carbon nanotubes to a polymer melt provides nucleation sites, consequently influencing the crystalline structure, crystallization temperature, and crystallization kinetics. Bhattacharya et al. have found that a PP crystallization rate with 0.8 wt. % SWNT was much faster than for neat PP. Additionally, there was a 10 $^{\circ}$C increase in the crystallization temperature [95]. Radhakrishnan et al. found a 12 $^{\circ}$C increase in the crystallization temperature of PP/SWNT nanocomposites prepared through hot coagulation process [25]. Valentini et al. observed that SWNT had a considerable effect on PP crystallization kinetics. They found the crystallization rate increased by measuring the decrease in crystallization half time, from 840 s to 115 s [96].

2.6.4 Microscopy

Microscopy techniques such as optical microscopy and scanning electron microscopy (SEM) are widely used in studying the morphology of polymer nanocomposites. Optical microscopy under reflected light is often used to image micro-scale distribution of nanotubes; however, optical microscopy is incapable of imaging below 0.2 to 0.5 μm so it cannot be used to directly observe smaller nanotube aggregates.

SEM on the other hand is not limited by the wavelength of visible light and can provide magnifications as high as 200kX with resolutions of 5-10 nm, which helps in identifying small nanotube bundles. SEM uses an electron gun to shoot electrons into an evacuated container. A condensing lens focuses the electrons into a beam, which is directed at the sample by scan coil. The electron beam moves across the specimen, and secondary electrons are disengaged from the specimen surface. These secondary electrons are collected and counted by a detector. The information thus gained is used to reproduce an image of the specimen surface. SEM images of polyurethane/MWNT nanocomposites are shown in Figure 2.16. A submicron level distribution of nanotubes in polymer matrix is clearly noticeable from these images.

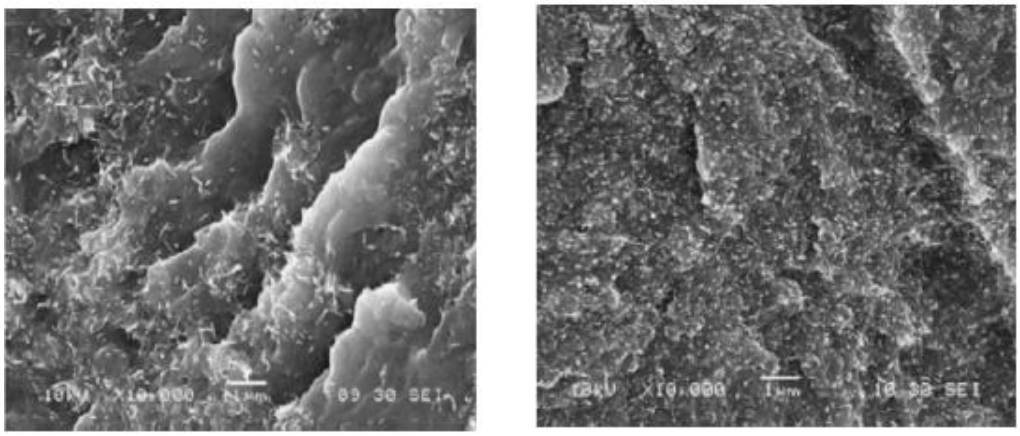

Figure 2.16. SEM micrographs of Polyurethane/MWNT nanocomposites (a) 10 wt.% pristine MWNT and (b) 20 wt.% MWNT-COOH [97].

2.6.5 Raman spectroscopy

Raman is an inelastic scattering event of a photon. It is rare event occurring once in every 10^6 - 10^8 photon scattering events [98]. Raman spectroscopy is a required characterization for carbon nanotubes as they have characteristic Raman vibrational modes as shown in Figure 2.17.

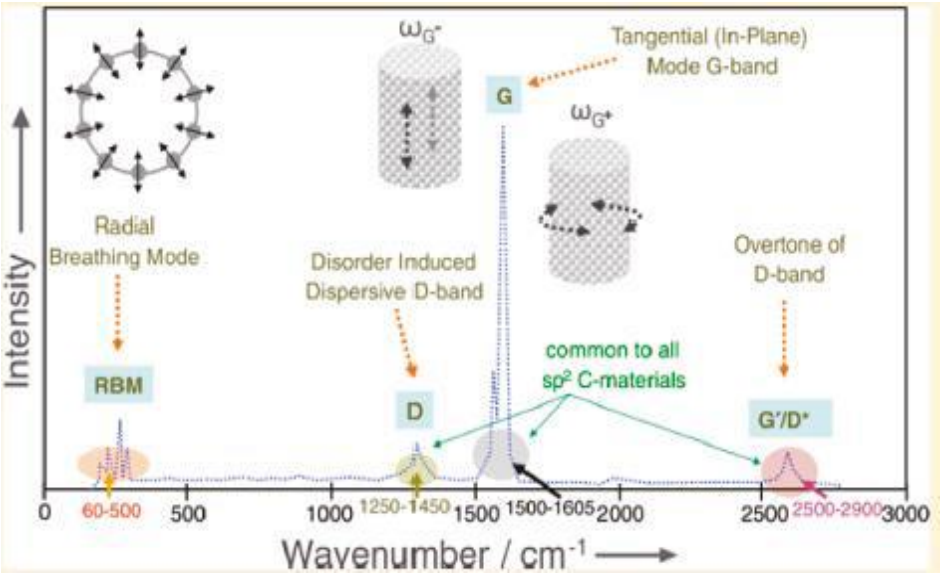

Figure 2.17. Characteristic vibrational modes for carbon nanotubes [99].

The characteristic Raman vibration modes of SWNT such as tangential vibrational modes and defect modes provides insight of nanotube surface modification and defects. Tangential modes (G-bands) encompass the vibration of C-C bonds along the tube axis (G^+) and along the circumference (G^-). The D-band vibrational mode arises from defects in the nanotube structure (e.g., sp3 hybridization, missing C-atom). The ratio of intensity of the D and G bands (I_D/I_G) gives an idea about the extent of nanotube surface modification or defects, as hybridization of C atoms will change from sp^2 to sp^3, thus increasing the D band intensity. The Raman spectroscopy instrument used in this study was a Renishaw (Gloucestershire, UK) inVia microRaman with 514 and 785 nm lasers [100].

2.6.6 Melt Rheology

Unlike microscopy techniques, rheological characterization is not limited to a certain area of a sample. It also provides better insight on the dispersion state of nanomaterials in a polymer matrix as well as information on nanomaterial-polymer interactions. Moreover, rheological characterization helps in understanding the flow behavior and microstructure of nanocomposites. An Anton Paar (Ashland, VA) MCR 301 rotational rheometer with a 25 mm parallel plate measuring system was used in this research. A schematic of the parallel plates is shown in Figure 2.18. The sample is loaded between the two plates, and any excess is trimmed off to form a flat edge. The top fixture is rotated at a desired rate to apply the necessary steady or dynamic shear on the sample, and the torque and normal forces are measured by the rheometer. Rheological properties of interest (such as viscosity, elastic, and viscous modulus) can be calculated from the knowledge of the shear applied, torque generated, gap between fixtures, and fixture geometry.

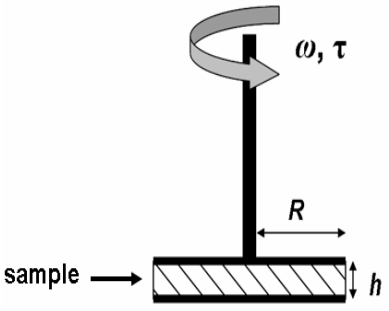

Figure 2.18. Parallel plate geometry [16].

The shear stress and shear rate on a parallel plate are calculated using following relationships-

$$\tau(R) = \frac{2M}{\pi R^3}$$

$$\dot{\gamma} = \frac{\omega R}{h}$$

Where $\dot{\gamma}$ = shear rate (1/s)

τ = shear stress (Pa)

M = Torque (N.m)

R = Radius of measuring plate (m)

h = gap between plates (m) ω = Rotational speed (s^{-1})

The rheological characterization of polymers is typically carried out by initially running an amplitude sweep test where the sample is subjected to different strains at a constant angular frequency. The changes in storage and viscous modulus are monitored at different strains applied on the sample. A typical amplitude sweep plot for polymers exhibit an initial plateau region at lower strains followed by an exponential decrease in value of storage/loss modulus at higher strain. The linear viscoelastic limit of a strain is typically taken as the strain value at which there is an approximate 5% decrease in the constant storage modulus value of a plateau region. This linear viscoelastic limit of the sample is useful while running dynamic tests, which are performed to probe the microstructure of the sample.

In dynamic tests, the sample is subjected to an oscillatory shear of constant amplitude within the linear viscoelastic region. The sample's response at high frequencies relates to the behavior of the sample at short time intervals, while the response obtained at low frequencies corresponds to the sample behavior at long time intervals. When an oscillating strain is applied on the sample, the resulting stress will also oscillate with the same frequency but will have a phase

lag of angle δ, with respect to strain. This data can be resolved into two components: a solid-like component (storage modulus denoted as G′) that is in phase with the input, and a liquid-like component (loss modulus denoted as G″) that is out of phase with the input. When the shear is applied on a material, part of the shear energy applied is stored within the sample. This allows the material to regain its structure when the shear is removed while the rest of the energy is lost as heat. The energy that is stored within the sample is known as storage (elastic) modulus, and the lost energy is known as loss (viscous) modulus.

The following equations relate these moduli to the applied strain, shear stress, and phase angle.

$$G' = \left(\frac{\tau}{\gamma}\right)\cos\delta$$

$$G'' = \left(\frac{\tau}{\gamma}\right)\sin\delta$$

Where,

γ = Shear strain (%)

δ = Phase angle

τ = Shear stress

Complex viscosity (η^*) is another important parameter obtained from the storage and loss modulus values and is given as follows:

$$\eta^* = \frac{\tau(t)}{\gamma(t)} = \frac{\sqrt{G'^2 + G''^2}}{\omega}$$

η^* is the measure of total resistance of the sample to a dynamic shear rate.

Dynamic oscillatory shear tests (frequency sweeps) at a fixed amplitude in the linear viscoelastic regime can be used to study the microstructure of the sample. The formation of an interconnected network inside polymer matrix upon the addition of nanofillers can be identified by the formation of a plateau region at a lower frequency, along with significant improvements in the storage modulus and complex viscosity of the sample [101, 102].

For melt processed 2 wt.% polycarbonate/MWNT nanocomposites, Potschke et al. found a step increase in storage modulus and complex viscosity, as shown in Figures 2.19 and 2.20, respectively. Further, the complex viscosity curves showed a non-Newtonian behavior at much lower frequencies with a higher decrease in complex viscosity. This is due to the formation of an interconnected network of MWNT within polycarbonate, such network formation is known rheological percolation [70, 103].

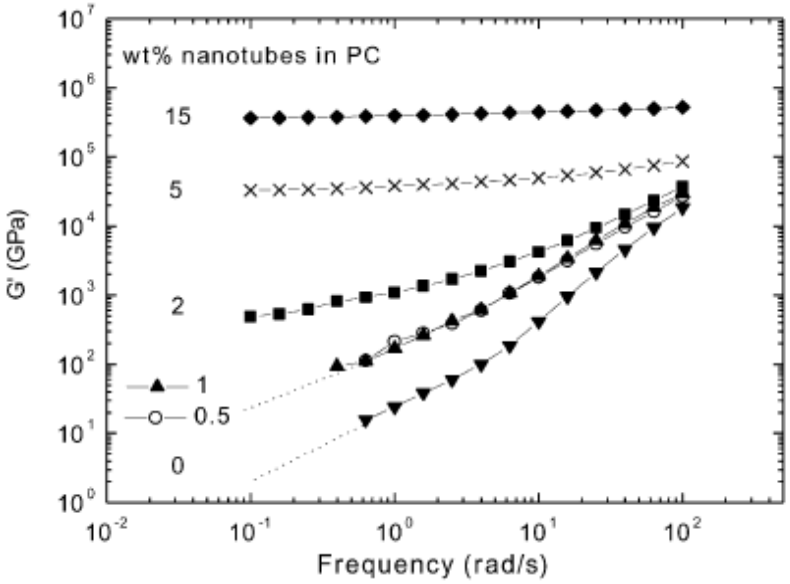

Figure 2.19. Storage modulus vs frequency of polycarbonate/MWNT nanocomposites at 260°C [103].

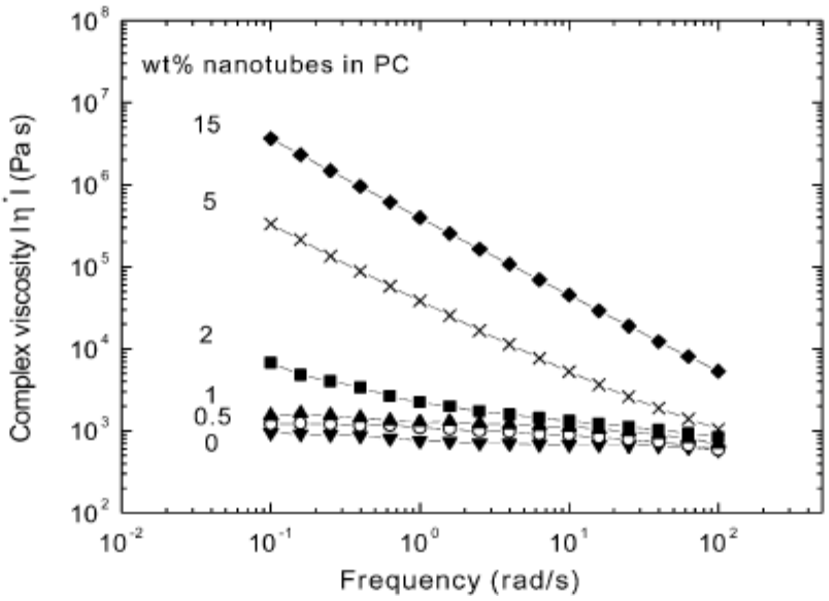

Figure 2.20. Complex viscosity versus frequency for polycarbonate/MWNT nanocomposites at 260 °C [103].

Chapter 3

Experimental Section

3.1 Materials

SWNT used in this research were manufactured through the CoMoCat process and were obtained from South West Nano Technologies (Norman, OK). Two different grades of SWNT were used: CG200 (Lot L04 and L14) and CG300 (Lot L3). CG200 has a purity of ~90%, aspect ratio of 1000, density 1.45 g/cm^3, and D/G ratio of 0.1. CG300 has a purity of >95%, aspect ratio of 940, density of 1.45 g/cm^3, and D/G ratio of 0.07. Polyvinylpyrrolidone (PVP) with an average molecular weight of 40,000 and sodium dodecyl sulfate were purchased from Sigma-Aldrich (St. Louis, MO. Polypropylene (PP) (density = 0.90 g/cm^3) was obtained as flakes (Melt Flow Index = 12, M_n= 63,000) from Total Petrochemicals (Houston, TX). Ethylene vinyl alcohol copolymer EVOH grade EVAL G176 (48 mol% ethylene) was obtained from Kuraray America (Houston, TX). Additives including Irganox 225B and Irgastab FS301 were obtained from BASF (Tarrytown, NY) and were dry blended with PP to produce nanocomposites with enhanced thermo-oxidative stability.

Based on the composition of primary and secondary antioxidants, FS301 acted as a processing stabilizer, whereas Irganox 225B was a processing and long-term thermal stabilizer. The primary antioxidant was a phenolic -OH group that worked as a free radical scavenger and prevented oxidation. The secondary antioxidant reacted with any hydroperoxides which had

formed during oxidation and converted them into non-radical products. All reference information for pure PP and EVOH is based on measurements of the resulting stabilized blends. Polylactic acid grade Ingeo™ Biopolymer 4043D was purchased from NatureWorks, LLC (Minnetonka, MN), and it had a density of 1.24 g/cm^3. Three different types of cellulose nanocrystals were used in this research. Spray dried powder of BioPlus-L® Crystals (lignin-coated cellulose nanocrystals) and an aqueous gel of BioPlus-L® crystals (regular CNC without surface modification) were obtained from American Process, Inc. An aqueous gel of sulfonated cellulose nanocrystals in were obtained from the University of Maine's Process Development Center.

3.2 Effect of Non-Covalent Functionalization of Single-Walled Carbon Nanotubes and Pre-Processing Methods on Polypropylene Nanocomposites

The materials used in this investigation were Total Petrochemical's isotactic polypropylene flakes, Irganox 225B, Irgastab FS301, CoMoCAT SWNT of grade CG200 from SouthWest Nanotechnologies, polyvinylpyrrolidone (PVP), and sodium dodecyl sulfate (SDS) from Sigma Aldrich. The SWNT were non-covalently functionalized using PVP and SDS in water. The pre-processing methods used were rotary evaporation and spray freeze drying prior to the melt processing of nanocomposites in a Haake Minilab twin screw extruder.

3.2.1 Non-covalent functionalization of SWNT

Non-covalent functionalization of SWNT was carried out by implementing optimization and modifications to the procedure used by Kayatin et al.[23] as discussed in Chapter 4. 2 mg/ml PVP/water stock solution was initially prepared by magnetically stirring the required quantities of PVP in distilled water for 10 minutes; 15 ml of this solution was taken in a vial followed by the

addition of SWNT in 1:1 ratio (by weight) with PVP. This mixture was then bath sonicated for 20 minutes in order to wet the nanotubes' surfaces and to keep them in dispersion. This was then ultra-sonicated using a SONICS vibra-cell tip sonicator for 30 minutes. The sonication process induced cavitation in a medium, which debundled the SWNT by overcoming the van der Waals force of attraction and allowed PVP to wrap on the SWNT surfaces. The sonication was carried out at 60% amplitude (~60W), with cycles of 5 seconds on and 3 seconds off. A similar procedure was used for SWNT functionalization using SDS. In order to study the effect of non-covalent functionalization of SWNT on nanocomposite properties, 2 mg/ml aqueous SWNT dispersions were prepared by using same sonication treatment.

3.2.2 Pre-processing methods

SWNT dispersions needed to be pre-processed with polymer in order to enhance their uniform dispersion state in final nanocomposites. Two different pre-processing techniques were investigated in this research—rotary evaporation and spray freeze drying. These two techniques were compared in terms of their effects on nanotube dispersion state in polymer matrix and thermal, and rheological properties of resultant nanocomposites.

The rotary evaporation technique was chosen based on the works of Radhakrishnan et al.[25]. This technique was shown to produce a more uniform SWNT dispersion state than mere dry mixing of nanotubes with polymer during melt processing. Also unlike the hot-coagulation technique, rotary evaporation did not require treatment with harsh solvents which induce degradation during processing [25]. Figure 3.1 shows the morphology of the samples produced with different pre-processing techniques from previous work on initial mixing methods. Rotary evaporated samples produced a uniform coating of SWNT on the polymer surface without causing

any degradation, unlike the hot-coagulation technique. Simple dry mixing provided the poorest SWNT distribution.

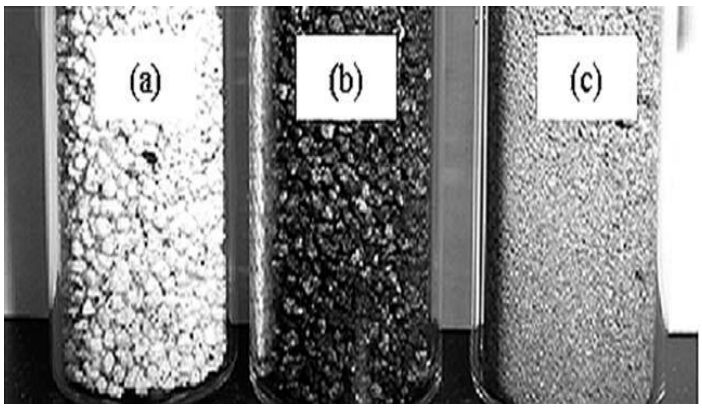

Figure 3.1. Macroscale appearance of PP–SWNT after initial mixing but before melt extrusion for (a) dry mixing, (b) rotary evaporation, and (c) hot coagulation [25].

The rotary evaporation pre-treated polymer-nanotube mixtures were produced by initially mixing polymer with 2 mg/ml aqueous dispersions of non-covalently functionalized or pristine SWNT using magnetic stirring for 10 minutes. The quantity of polymer was added in order to get 0.75 vol.% concentration of SWNT in final nanocomposite. The solvent in this mixture was evaporated at 100 °C under vacuum in a Buchi RE-121 rotary evaporator for a period of time dependent on the amount of solvent. Rotary evaporation provided continuous movement of the mixture during solvent evaporation, finally producing polymer with a uniform coating of SWNT. To further assure complete solvent removal, the nanotube-coated PP was vacuum dried overnight at 80 $^{\circ}$C for 6 hours.

The spray freeze drying technique was used by Khoshkava et al. [27] for making PLA/CNC nanocomposites. It produced a highly porous morphology of spray freeze dried CNC, which was

useful during melt processing. Such porous structures allowed an enhanced melt filtration, thereby improving the dispersion state of nanomaterials in the polymer matrix. This technique was of interest in this research, as it helped in delivering a uniform dispersion of SWNT in a solvent to final nanocomposite, reducing the aggregation during the pre-processing stage [16-19].

The spray freeze dried samples of SWNT were produced by using a fine spray bottle to spray 2 mg/ml aqueous dispersions of SWNT (both non-covalently functionalized and pristine) into a container with liquid nitrogen. The fine droplets obtained from the spray nozzle formed a frozen slurry in the container, which was kept in suspension using magnetic stirring. This slurry was then transferred to freeze drying flasks and freeze dried using a Labconco 4.5 Freezone apparatus. The freeze drying time varied from 24 hours to 48 hours, depending on the volume of the sample. The spray freeze dried samples were then kept at 80 $^{\circ}$C under vacuum for 6 hours to remove any residual moisture. These samples were then blended with PP flakes by manually shaking in a vial for 1 minute.

3.2.3 Polymer melt Processing

Pre-processed samples were extruded using a Haake Minilab counter rotating twin screw extruder, as shown in Figure 3.2. Thermal and processing additives (including Irganox 225B and Irgastab FS301) were added to the pre-processed polymer samples at 0.25 wt.% and 0.15 wt.%, respectively. Additives were dry mixed with the pre-processed polymer samples prior to extrusion.

The extruder barrel temperature, screw speed, and time of extrusion were the controlled parameters during extrusion. The combined action of the high temperature and the shear produced by the rotating screws melted the polymer broke apart the nanomaterial aggregates, and distributed the nanomaterials in the polymer matrix as the materials flowed down the barrel. The advantages

of using the Minilab extruder were that it required a very low volume of materials (~ 5 cm^3) and that the availability of a backchannel allowed for the material recirculation through the barrel until the desired level of mixing was achieved.

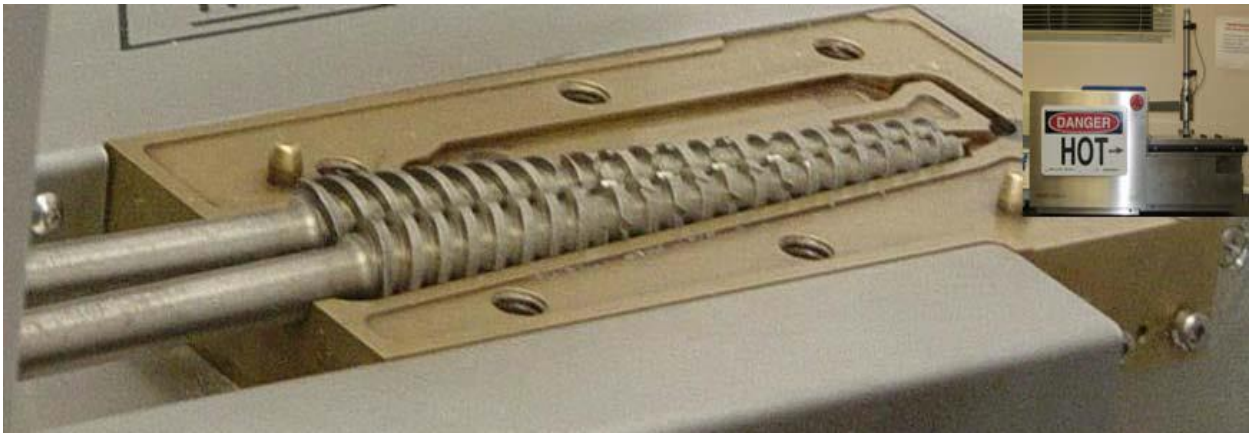

Figure 3.2 Inside of the Haake Minilab Twin screw extruder.

For melt processing of PP nanocomposites in an extruder, the processing conditions were chosen as 190 °C and 100 rpm for 30 minutes. These were based on the design of experiments by Radhakrishnan et al. for polypropylene nanocomposites [16], where the optimized processing condition provided maximum improvement in thermal properties for the similar SWNT loading used in this research.

All nanocomposites were prepared at a concentration of 0.75 vol. % (~1.2 wt.%). This value was chosen based on the anticipated ability to achieve percolation for nanocomposites in which the SWNT existed as small bundles. In previous studies on PP, post-processing (6 hour bath sonication) SWNT aspect ratios, as established from AFM analysis, were in the range of 200 – 400; for this range of aspect ratios, the critical volume fraction for percolation was achieved at a $0.0035 < \Phi < 0.007$ [16, 104]. Since SWNT in this research underwent 30 minutes of

ultrasonication, a concentration of 0.75 vol. % was considered enough to allow for some bundle formations with a percolated network and yet not too high to facilitate re-aggregation.

3.3 Polyvinylpyrrolidone functionalized SWNT – Poly (Ethylene-co-Vinyl alcohol) Nanocomposites

The materials used in this study were EVOH (EVAL G176) pellets obtained from Kurraray, Irganox 225B, Irgastab FS301, CoMoCAT SWNT of grade CG300 from SouthWest Nanotechnologies, and polyvinylpyrrolidone from Sigma Aldrich. PVP functionalized SWNT were produced using the procedure as explained in 3.2.1. In this case, the pre-processing of PVP functionalized SWNT was carried out using a spray freeze drying method, (as mentioned in 3.2.2) followed by processing using a Haake Minilab twin screw extruder, as was performed for PP nanocomposites.

3.4 Polylactic Acid-Cellulose Nanocrystals Nanocomposites

The materials used in this investigation were PLA (4043D) pellets and three types of cellulose nanocrystals – lignin coated, sulfonated, and unmodified regular CNC. PEO with a molecular weight of 1000 was used to make the masterbatches with sulfonated CNC. Unmodified regular CNC and lignin-coated CNC were obtained from American Process (Atlanta, GA) and have an average particle size of 4-5 nm wide and 50-500 nm long. Sulfonated CNC were obtained from University of Maine, Process Development Center. The pre-processing methods used were spray drying, freeze drying, spray freeze drying prior to the melt processing of nanocomposites in a Haake Minilab twin screw extruder.

3.4.1 CNC dispersion

3 mg/ml CNC dispersions were prepared in water by initial overnight magnetic stirring, followed by ultrasonication for 5 minutes at 30% amplitude and cycles of 5 seconds on and 3 seconds off using SONICS Vibra-cell tip sonicator. The concentration of CNC was chosen based on the BET results shown by Khoshkava et al. [86], where the 3 mg/ml concentration of CNC/water dispersion resulted in the maximum surface area in spray freeze dried CNC due to its high porosity. These dispersions were used in producing spray dried, freeze dried, and spray freeze dried CNC powder during pre-processing.

3.4.2 Pre-processing methods

Pre-processing was carried out by using spray drying, freeze drying and spray freeze drying of the CNC dispersions. Spray drying has been widely used in obtaining fine powdered samples from solutions or suspended dispersions [89, 105]. 3 mg/ml CNC/water dispersions were used to produce spray dried powder using a B-290 from Buchi mini spray dryer. The schematic of a typical spray dryer is shown in Figure 3.3. The dispersion was pumped through a nozzle to form a fine spray of liquid with the aid of an air/nitrogen medium. The fine droplets thereby produced were dried in a chamber at a temperature of 120 °C. The dried particles were collected in an another chamber with the aid of a cyclone. The particle size of such spray dried powder is typically 2-25 µm for the true solutions and ~50 µm for the suspensions [106].

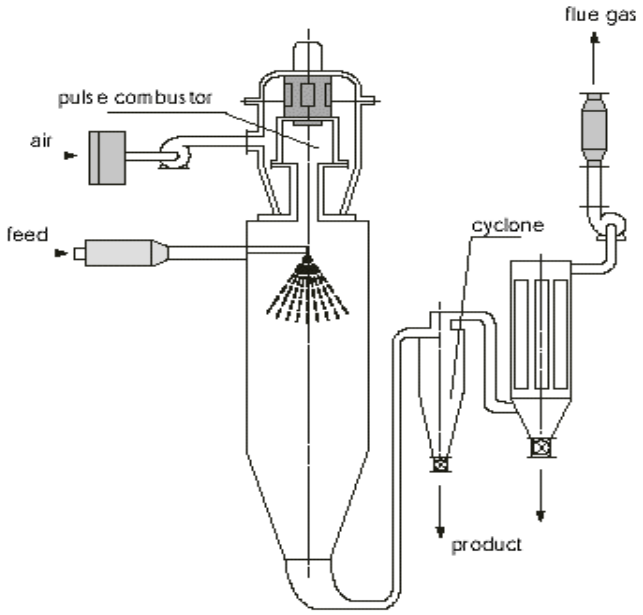

Figure 3.3 Schematic of spray dryer.

Freeze dried CNC samples were produced by initially freezing the 3 mg/ml CNC/water dispersion in a liquid nitrogen medium. The frozen sample was then dried in a Labconco 4.5 Freezone apparatus to obtain the porous network of freeze dried CNC. Spray freeze dried CNC samples were produced from 3 mg/ml CNC/water dispersion using a procedure similar to that which was explained in Section 3.2.2.

In order to produce the PLA/CNC nanocomposites through masterbatch mixing, PEO/CNC masterbatches were prepared by making 3 wt.% PEO solution in water followed by the addition of CNC to this solution. A weight ratio of 1.25:1 (PEO to CNC) was maintained in the dispersion. This ratio was based on the procedure used by Arias et al. [24], where a highly uniform dispersion state of CNC in PLA was observed at this ratio. This mixture was then magnetically stirred overnight and then subjected to ultrasonication for 5 minutes at 30% amplitude for cycles of 5

seconds on and 3 seconds off using SONICS Vibra-cell tip sonicator. The resulting dispersion was then spray freeze dried (using the procedure mentioned in 3.2.2) to obtain PEO/CNC masterbatch.

Spray dried, freeze dried, spray freeze dried CNC samples, and PEO/CNC masterbatch were dry mixed with PLA pellets. The quantity of added PLA was such that 8 wt.% CNC concentration was obtained in final nanocomposites. This mixture was vacuum dried at 80 ˚C for 4 hours. The drying of PLA pellets was critical since the PLA was a condensation polymer, any residual moisture would have caused PLA degradation through hydrolysis at higher temperatures [107].

3.4.3 Polymer melt processing

The pre-processed sample mixtures were extruded at 190 ˚C, 60 rpm, 20 minutes in a Haake minilab twin screw extruder. No additives were added during melt processing in order to retain the biocompatibility of PLA/CNC nanocomposites.

Solution processed samples were also prepared in order to compare them with the melt processed nanocomposites. Solution processing has been widely used by researchers [108, 109] since it produces highly uniform dispersions of nanofillers in the polymer matrix. The solution-processed 8 wt.% PLA/SA-CNC nanocomposites were produced by separately making solutions of 1 wt.% SA-CNC/chloroform and 10 wt.% PLA/chloroform. A 1 wt.% SA-CNC/chloroform dispersion was ultrasonicated at 30% amplitude and for cycles of 5 seconds on and 3 seconds off using SONICS Vibra-cell tip sonicator for 10 minutes. A 10 wt.% PLA/chloroform solution was magnetically stirred for 6 hours to create the uniform PLA/chloroform solution. The two mixtures were then mixed together and magnetically stirred for 2 hours to create the uniform PLA/SA-CNC/chloroform solution. This solution was then cast into thin films in a Petri dish and kept in a

hood overnight to evaporate most of the chloroform. These partially dried films were subsequently vacuum dried at 45 °C for 10 days to completely remove the remaining chloroform.

3.4.4 Nanocomposite filament preparation and FDM

PLA/CNC nanocomposite filaments with diameters of 1.75 ± 0.1 mm were obtained using the die plate with a 1.5 mm diameter at the extruder outlet. The increased diameter of the filament was due to a die-swelling effect wherein polymer chains relaxed after coming out of the die and thus increased the size of the filament. The die-swelling effect using 1.5 mm die in the case of plain PLA and all PLA/CNC nanocomposites was such that the resultant filament diameter obtained was ~1.6 mm to 1.8 mm. This was close to the Cube 3 filament diameter specification of 1.75 ±0.05 mm and was still printable.

The focus of this research was on the production of 3D-printed scaffolds from these filaments for algae growth. PLA is a biodegradable polymer, and its nanocomposites with CNC were thought to potentially improve scaffolds' mechanical strength and thermal and environmental stability, thus prolonging their use for algae growth. Moreover, due to the hydrophilic nature of CNC, algae growth was expected to enhance in this study. PLA/CNC nanocomposite scaffolds were under investigation, and their effects on PLA/CNC algae growth have yet to be determined.

3.5 Characterization

A Nikon (Melville, NY) Eclipse 80I optical microscope with reflected light was used to capture an image of the dispersion state of the SWNT in the polymer matrix. The samples for optical microscopy were prepared by pressing the nanocomposite melt between the heated extruder surface and the microscope slide at 190 ˚C. A 20x objective (0.45 NA) and 2x magnification before the camera (translating to an effective magnification of 40x) were used to image the samples. SEM

images were obtained using a JEOL (Tokyo, Japan) 7000-F Field Emission Scanning Electron Microscope; pre-processed SWNT and CNC dispersion samples, and polymer nanocomposite films were sputter-coated with gold before taking images.

Melting and crystallization temperatures were measured on a TA Instruments (New Castle, DE) Q100 Differential Scanning Calorimeter (DSC) at a scan rate of 10 °C/min over a temperature range of 20 to 200 °C, using aluminum pans/lids. The sample was first heated at 10 °C/min to 200 °C and held for 5 minutes. It was then cooled at 10 °C /min to 20 °C with a hold of 5 minutes before it was again heated at 10 °C/min to 200 °C. The heat-cool-heat cycle was performed to ensure the melting of all crystallites and to remove thermal history. Isothermal crystallization studies for PP was performed by heating the sample to 200 °C at 10°C/min with an isothermal hold of 5 minutes to ensure the melting of all crystallites, followed by rapid cooling at 100 °C/min to the desired crystallization temperature and holding isothermally for 30 minutes. In case of PLA, isothermal cold crystallization kinetics was studied, in which the sample was heated to 190 °C at 100 °C/min with an isothermal hold of 5 minutes, followed by cooling at 100 °C/min to 20 °C with an isothermal hold of 5 minutes. Finally, the sample was again heated at 100 °C/min to the desired crystallization temperature and held isothermally for 30 minutes.

Thermal decomposition was studied using a TA Instruments (New Castle, DE) Q5000 Thermal Gravimetric Analyzer (TGA). All TGA tests occurred under a constant nitrogen balance protection with a flow rate of 10 cm^3/min and a sample gas (nitrogen) flow rate of 25 cm^3/min. Samples were heated with ramp rate of 10 °C/min to 120 °C. They were then held isothermally at 120°C to ensure residual moisture removal. Samples were again ramped to 800 °C at 10 °C /min followed by an isothermal hold for 45 minutes. A sample size of ~20 mg was used for every TGA test in order to avoid any potential deviations in heat flow or accuracy associated with sample size.

Rheological characterization was performed on an Anton Paar (Ashland, VA) MCR 301 rotational rheometer. This was equipped with a CTD 450 convection temperature control device, using 25 mm parallel plates at a temperature of 200 $^{\circ}$C for PP and EVOH nanocomposites and 190 $^{\circ}$C for PLA nanocomposites. Initially, amplitude sweeps were performed in order to determine the linear viscoelastic regime (LVR) limit of the samples. The LVR strain limit was chosen as the strain at which the storage modulus is 95% of its constant value in the plateau region of the amplitude sweep plot. Frequency sweeps between 0.1 – 600 s^{-1} were performed at percent strain well within the LVR region, usually chosen as an order magnitude of a lower value of strain (%) than that of LVR strain (%) limit obtained from the amplitude sweep.

Chapter 4

Effect of Non-Covalent functionalization of Single-Walled Carbon Nanotubes and Pre-Processing methods on Polypropylene Nanocomposites

This chapter focuses on improving the dispersion state of SWNT in melt processed PP nanocomposites using a non-covalent functionalization approach and different pre-processing methods. The dispersion state of nanotubes in polymer melts is governed by thermodynamic, mechanical, and kinetic factors. Therefore, improving the thermodynamic compatibility of nanotubes with the polymer matrix and facilitating exfoliation of nanotube bundles are the key factors for improving the dispersion state. These factors have been assessed based on the non-covalent functionalization of SWNT using PVP and SDS in conjunction with rotary evaporation or spray freeze drying as the pre-processing methods for making PP nanocomposites.

Many attempts to make melt processed nanocomposites have used dry mixing of pristine or covalently functionalized nanotubes with polymer prior to melt processing [16-18, 20]. This has typically resulted in a poor dispersion state of nanotubes in the polymer matrix and/or poor interfacial interactions, and led to only modest improvements in nanocomposite properties.

Several attempts have been made to improve the nanotube dispersion in polymer matrices by using different pre-processing methods and/or nanotube functionalizations. Zhang et al. employed the method of spraying the aqueous dispersion of sodium dodecyl sulfate functionalized SWNT directly onto polymer followed by vacuum drying. The more uniform distribution of

nanotubes prior to melt processing resulted in an improved dispersion state which led to reduction in rheological and electrical percolation thresholds [110]. The rotary evaporation (RE) method used by Radhakrishnan et al. (a slight modification of spray drying) improved thermal and rheological properties of PP/SWNT nanocomposites compared to the dry mixing method; however, in their study, this method unexpectedly resulted in a poor dispersion state for SWNT covalently functionalized with dodecane groups using the Billups reaction [16]. The spray freeze drying (SFD) technique has been recently used by Khoshkava et al. for making PLA/CNC nanocomposites; a highly uniform dispersion state of CNC was observed causing three orders of magnitude improvement in the storage modulus compared to spray dried and freeze dried CNC and PLA nanocomposites at similar loadings [90]. The spray freeze dried CNC samples were found to be more highly porous than the spray dried and freeze dried CNC samples. Such highly porous and weak agglomerates allowed melt infiltration of polymer and breaking during processing to occur more easily.

Although pre-processing and functionalization approaches have been used to improve nanomaterial dispersion state in melts, there have been only limited attempts to improve the dispersion state of nanotubes through combination of functionalization (especially through non-covalent functionalization) and pre-processing methods.

In this study, PP nanocomposites were prepared using non-covalently functionalized SWNT through SFD and RE methods. SFD and RE are two promising methods for incorporation of nanomaterials in polymer melts. Moreover, non-covalently functionalized SWNT would assist in further improving the dispersion state in polymer matrix through nanotube compatibilization. The resulting PP nanocomposites were compared based on their morphology, rheology, and thermal properties.

4.1 Optimization and scale up of SWNT non-covalent functionalization

PVP was used for the non-covalent functionalization of SWNT, since it is not only inexpensive and biocompatible, but also forms tight and uniform physical wrapping around the nanotube surface. O'Connell et al. [22] showed that PVP-SWNT demonstrates a robust physical interaction compared to some other polymers. A modified flow field-flow fractionation technique was used to test the stability of the polymers on the nanotubes' surfaces. In the case of PVP-SWNT, most of the PVP remained intact, even after the intensive washing step, while other polymers were not retained on the SWNT surface. Kayatin et al. [23] developed a process for PVP/SWNT dispersion in water and showed that the freeze dried form of these PVP functionalized nanotubes had solubility as high as 150 mg/ml in UPR (unsaturated polyester resin), highlighting its potential use in making nanocomposites for this commercially-relevant polymer resin [23]. PVP-functionalized graphene was used by Green et al. for making PVP-graphene nanocomposites through in-situ polymerization of N-vinyl pyrrolidone. They found a 37 % increase in Young's modulus and 7 orders of magnitude increase in electrical conductivity [111].

The procedure for making dispersions in this research was the modification of a procedure developed by Kayatin et al., where a lower concentration of SWNT (0.33 mg/ml) was used to make the dispersions with an excess of PVP, with a PVP to SWNT ratio of 30 [23]. Since non-covalent attachment has well been established in the literature, characterization focused on the relative amounts of PVP that could not be readily removed. Such high concentrations of PVP in the dispersions would affect the composite's thermal and mechanical properties; therefore, this excess of PVP must be removed before melt processing the dispersions with polymer. Repeated vacuum filtration and aqueous washing steps were employed to remove the excess PVP from the aqueous PVP/SWNT dispersion prepared using the procedure of Kayatin et al. [23]. While rinsing

out this excess PVP using a vacuum filtration system, it was found that hydrophilic polycarbonate filter pores were blocked very quickly due to the comparable size of the nanotube bundles, making further filtration very difficult. In an attempt to find an alternative, a small quantity of the repeatedly washed PVP-SWNT sample was taken and analyzed using TGA, as shown in Figure 4.1. A difference of ~ 45 wt % between PVP-SWNT and SWNT TGA curves suggested the presence of non-covalently attached PVP on SWNT surfaces. Composition calculations from TGA data showed that the final PVP to SWNT ratio in these washed PVP-SWNT samples ranged from 0.7 to 1, which was much smaller than initial ratio of 30. This finding revealed that the actual quantity of PVP was much smaller compared to quantity initially used.

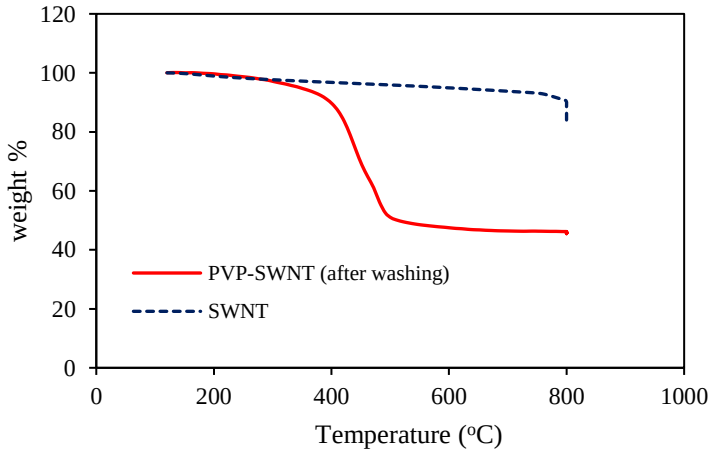

Figure 4.1. Thermogravimetric analysis of SWNT and PVP-SWNT in nitrogen medium.

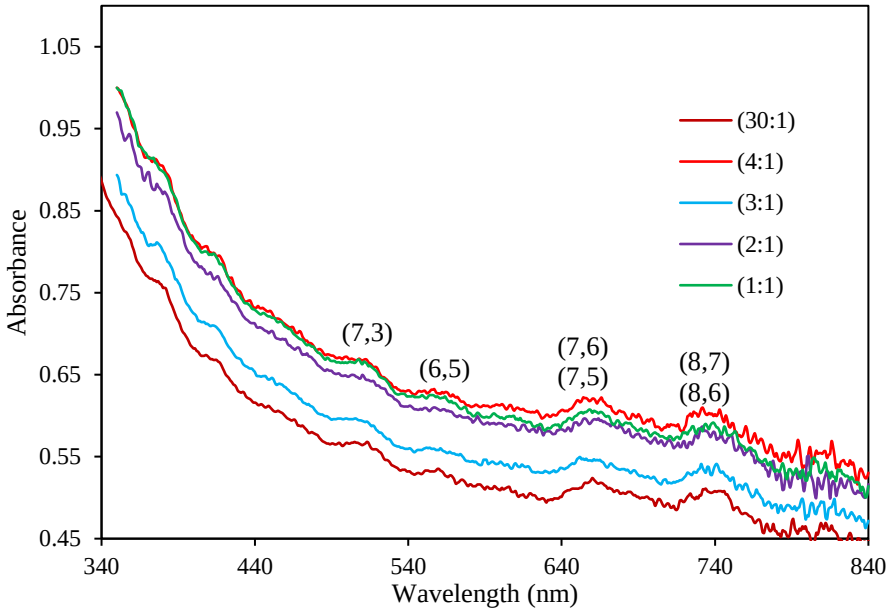

Figure 4.2. UV-Vis spectra for 0.33 mg/ml aqueous SWNT dispersion with varying PVP/SWNT ratios.

Later dispersions were prepared with lower PVP/SWNT ratios of 4, 3, 2 and 1. Figure 4.2 compares the UV-vis spectra for the (0.33 mg/ml) dispersions made with various PVP/SWNT ratios. The UV-vis spectra suggested no significant change in the degree of dispersion since intensities of absorption peaks of aqueous PVP-SWNT dispersions did not change upon reducing PVP/SWNT ratio from 30 to 1. From these findings, the PVP/SWNT ratio was optimized to 1. O'Connell et al. have found a similar ratio of PVP/SWNT (~ 0.7-1) after several washing steps for SDS-PVP/SWNT, which further supports this study [22].

In order to readily produce sufficient SWNT for nanocomposite research, SWNT quantities for making 0.75 vol. % PP nanocomposites, the concentration of SWNT in dispersion was scaled up to 2 mg/ml from its initial lower concentration of 0.33 mg/ml. Figure 4.3 compares the UV-vis spectra for dispersions with 0.33 mg/ml and 2.0 mg/ml concentrations with a 1:1 PVP/SWNT ratio. Dispersions at these concentrations also did not show any difference in intensities of van Hove

singularity peaks. Thus, the PVP-SWNT functionalization procedure used by Kayatin et al was optimized for this research by using a lower PVP/SWNT ratio as well as higher SWNT concentration in dispersion.

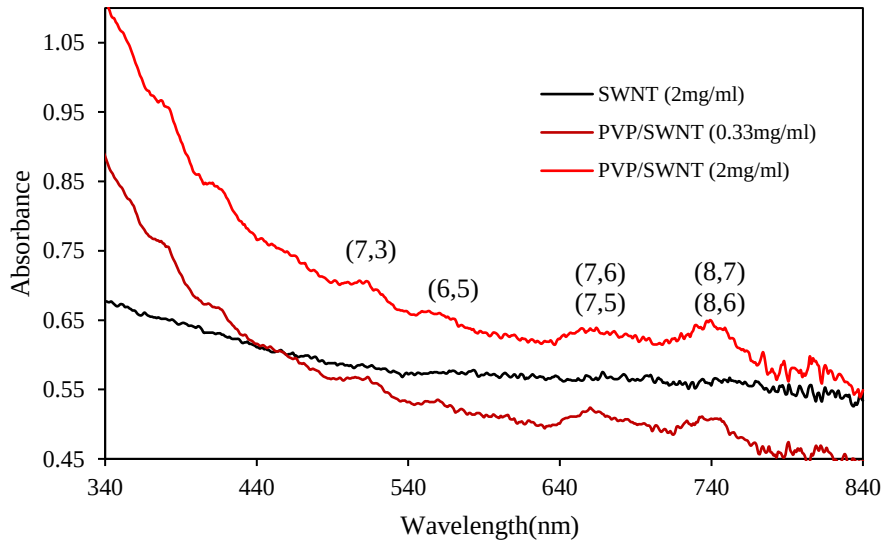

Figure 4.3. Comparison of UV-Vis spectra dispersions with different SWNT concentrations and a 1:1 PVP to SWNT.

4.2 PVP and SDS functionalized SWNT

The PVP functionalization of SWNT was evident from the UV-Vis spectra of its aqueous dispersion, as well as from the TGA runs carried out on rinsed PVP-SWNT samples. Distinct peaks observed in UV-vis spectrum (as shown in Figure 4.4) corresponded to the Van-Hove singularities of different chiralities in SWNT, which was an indication of more individualized nanotubes. PVP functionalized SWNT showed more distinct and sharp peaks, since PVP was an effective dispersing agent. Due to its hydrophilic nature, PVP had a strong thermodynamic drive to wrap

around the SWNT surface, reducing the hydrophobic interphase between nanotubes and aqueous media [22]. In contrast, the SDS functionalized SWNT/water dispersion did not show any peaks, indicating a poor dispersing ability of SDS at a SWNT concentration of 2 mg/ml.

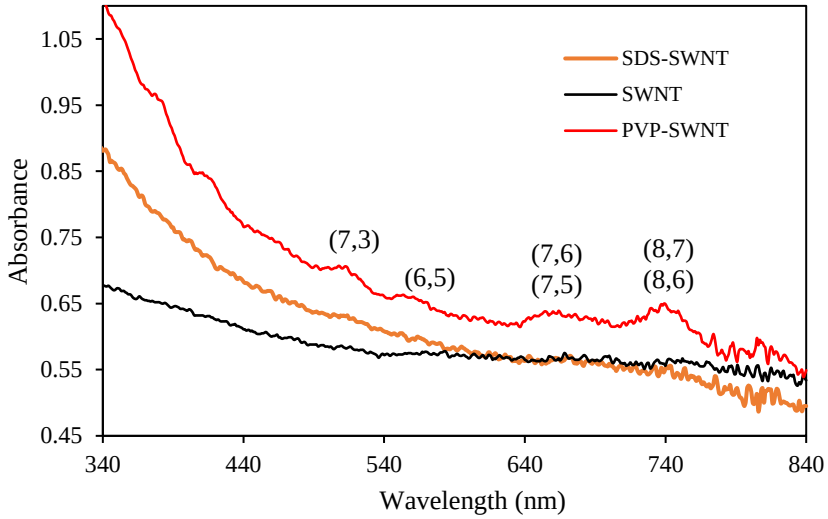

Figure 4.4. UV-vis spectra for 2 mg/ml aqueous dispersions of SWNT, SDS-SWNT, and PVP/SWNT.

TGA runs under a nitrogen medium were performed on PVP-SWNT and SDS-SWNT samples, which were rinsed with water to ensure the removal of any free dispersing agents present in these samples. The difference in weight loss obtained from the samples' TGA curves (Figure 4.5) also gave an estimation of the degree of functionalization in these SWNT samples. A higher degree of functionalization ~ 50 wt. % was observed for PVP-SWNT whereas SDS-SWNT had ~ 30 wt. %.

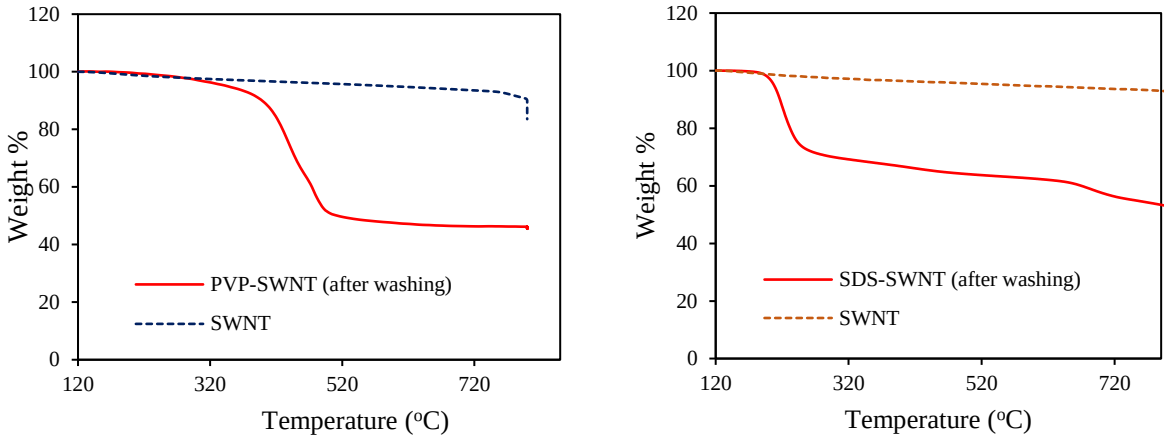

Figure 4.5. TGA curves for SDS and PVP functionalized SWNT.

4.3 Morphology

Optical microscopy images of PP/SWNT and PP/PVP-SWNT nanocomposites prepared using the rotary evaporation method are shown in Figure 4.6 (a) and (b), respectively. It was expected that nanocomposites using PVP functionalized SWNT would result in a more uniform dispersion state compared to pristine SWNT. However, bigger nanotube aggregates were observed in PP/PVP-SWNT nanocomposites, with most of them having a size greater than 50 µm; the average aggregate size was below 50 µm in PP/SWNT nanocomposites.

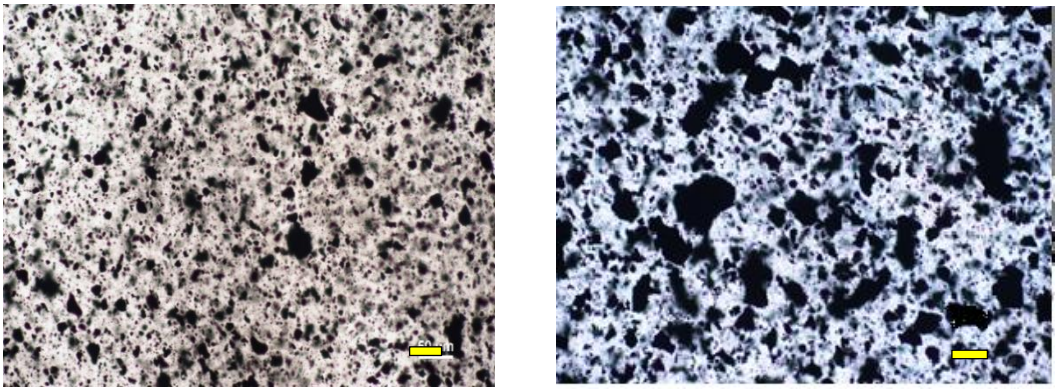

a. PP/SWNT (0.75 vol.%) b. PP/PVP-SWNT (0.75 vol.%)

Figure 4.6. Optical microscopy images for samples extruded at 190 °C and 100 rpm for 30 minutes. (scale bars – 50 µm)

Although PVP-SWNT were dispersed more uniformly in an aqueous dispersion as opposed to pristine SWNT, the increased level of aggregation in PP/PVP-SWNT would have been caused during the rotary evaporation and melt processing steps. In order to investigate the aggregation effect during rotary evaporation, a few drops of PVP-SWNT/water and SWNT/water dispersions were taken on glass slides. These were then subjected to vacuum drying in order to provide similar conditions as the rotary evaporated samples. Figures 4.7 and 4.8 show their dispersion states before and after vacuum drying respectively. The dried PVP/SWNT dispersion had bigger aggregates than the SWNT dispersion, which showed that significant PVP-PVP interactions resulted during the evaporation of water. These interactions formed aggregates as large as ~ 200 µm. Such aggregation might have been due to capillary forces and van der Waals interactions as the dispersion concentrated upon drying. Aggregation was more predominant in PVP functionalized SWNT, as it was a more concentrated system [90, 112]. This investigation showed that aggregation was higher in PP/PVP-SWNT prior to the melt extrusion, although aggregate size was somewhat reduced during melt processing, as shown in Figure 4.6.

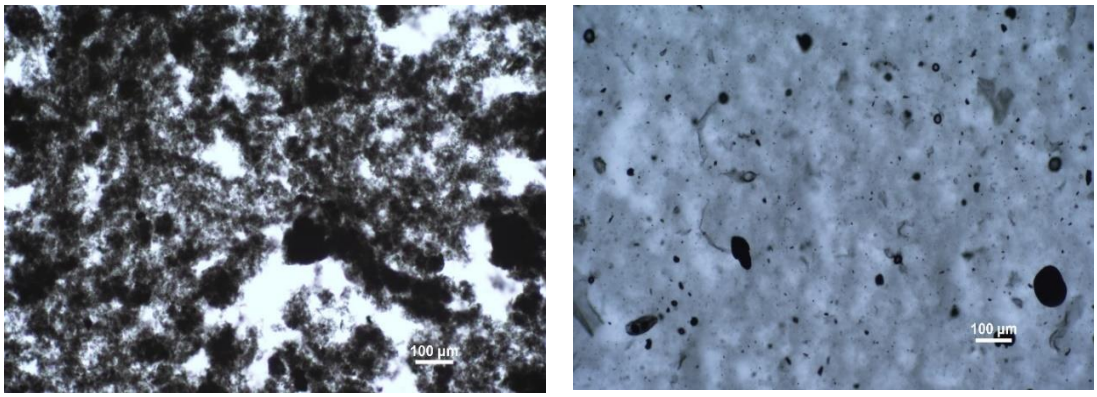

a. SWNT/water dispersion b. PVP-SWNT/water dispersion

Figure 4.7. Optical microscopy images of dispersions before vacuum drying. (scale bars – 100 µm)

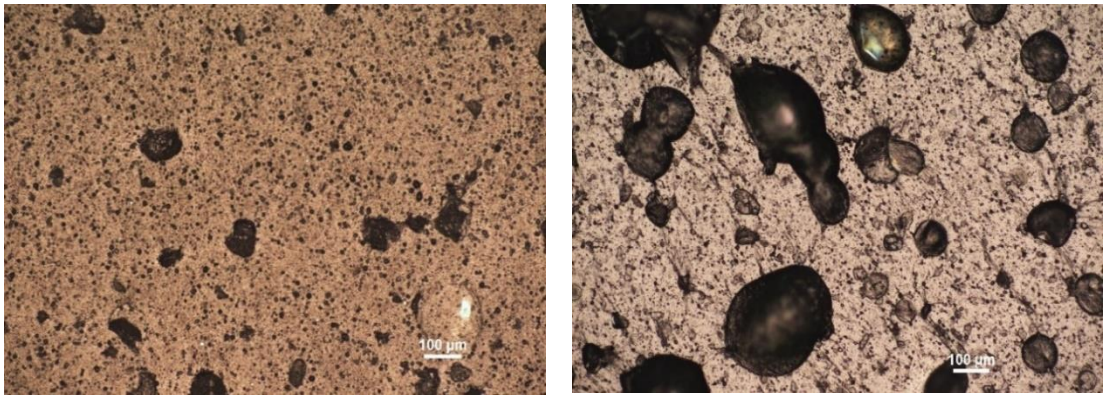

a. SWNT/water dispersion b. PVP-SWNT/water dispersion

Figure 4.8. Optical microscopy images of dispersions after vacuum drying. (scale bars – 100 µm)

Another possible factor leading to aggregation was tested based on thermodynamic compatibility of the PVP and PP during melt processing. Though extrusion helps in mixing PP and PVP-SWNT in molten state due to applied shear, the incompatibility between PVP and PP would lead to bigger aggregates. In order to check this incompatibility, the Flory-Huggins theory was applied as it is used as a guideline for polymer pair miscibility [113]. In order to use this method, solubility parameters were calculated for PVP and PP using Hoftyzer-van Krevelen (VKH) method and Hoys group contribution method respectively [114], as shown in Table 4.1.

Polymer	Solubility parameter	Solubility parameter $(cal/cm^3)^{0.5}$
Polyvinylpyrrolidone	24.3	11.9
Polypropylene	16.7	8.17

Table 4.1. Calculated solubility parameters for PVP and PP.

In order to check the compatibility for pair of polymers (A and B), the interaction parameter (χ_{AB}) as well as the interaction parameter at the spinodal point in the phase diagram $(\chi_{AB})_{sp}$ were calculated and compared. The two polymers would be compatible when $(\chi_{AB}) < (\chi_{AB})_{sp}$

Interaction parameter (χ_{AB}) is given by

$$\chi_{AB} = \frac{V_r(\delta_A - \delta_B)^2}{R.T}$$

Where, V_r – Reference volume, taken as 100 cm^3/mol. (approx. molar volume of smallest possible repeating unit in polymer)

R- Ideal gas constant T- Room temperature (25 ˚C)

A and B corresponds to PVP and PP respectively

$$\chi_{AB} \cong \frac{(\delta_A - \delta_B)^2}{6}$$

$$\chi_{AB} = 2.33$$

In order to check the compatibility of polymers at particular composition, $(\chi_{AB})_{sp}$ is calculated, which is given by

$$(\chi_{AB})_{sp} = 0.5\left(\frac{1}{x_A.(\emptyset_A)_{sp}} + \frac{1}{x_B.(\emptyset_B)_{sp}}\right)$$

Where x_A = Degree of polymerization for PVP $x_A = \frac{Molecular\ weight\ of\ A}{100}$

$(\emptyset_A)_{sp}$ = Volume fraction of polymers in nanocomposite

$$x_A = 400 \qquad x_B = 670$$

For 0.75 vol.% nanocomposite –

$(\emptyset_A)_{sp}$ = 0.009 and $(\emptyset_B)_{sp}$ = 0.991

For polymer to be compatible at this composition

$$\boldsymbol{X_{AB} < (X_{AB})_{sp}}$$

For 0.75 vol.% PP/PVP blend

$(\boldsymbol{X_{AB}})_{sp}$ = 0.14 which is less than $\boldsymbol{X_{AB}}$, therefore phase separation is desired.

Given this, PP-PVP immiscibility was also a plausible reason for the poor state of dispersion observed in PP/PVP-SWNT. Although these calculations predicted phase separation, these kinds of predictions can act as only guidelines; actual compatibility should be tested on the basis of experiments.

Based on these hypothesis, SDS (a low molecular weight anionic surfactant) was tried which was found to be compatible with PP, based on similar calculations shown above. Moreover, SDS functionalized SWNT were expected to reduce the aggregation upon drying, due to the presence of a negative charge. However, as shown in the optical microscopy images of melt pressed PP/SDS-SWNT in Figure 4.9 (c), the dispersion state was slightly improved, yet it still showed the presence of aggregates of ~50 μm in size. In spite of the predicted compatibility of SDS with PP, SDS-SWNT still showed bigger aggregates when compared to SWNT in the PP matrix. This suggests that capillary and van der Waal forces acting between nanotubes during rotary evaporation were dominant factors responsible for the enhanced aggregation in these non-covalently functionalized SWNT and PP nanocomposites.

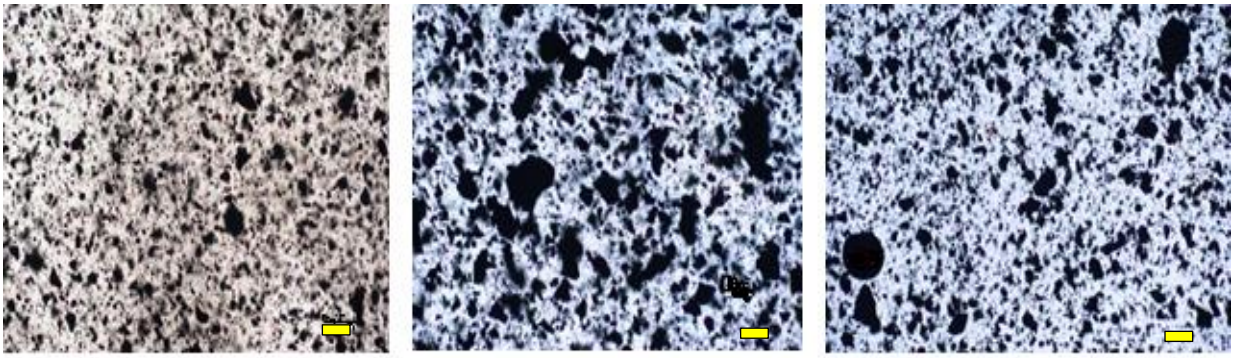

a. PP/SWNT composite (RE) b. PP/PVP-SWNT composite (RE) c. PP/SDS-SWNT composite (RE)

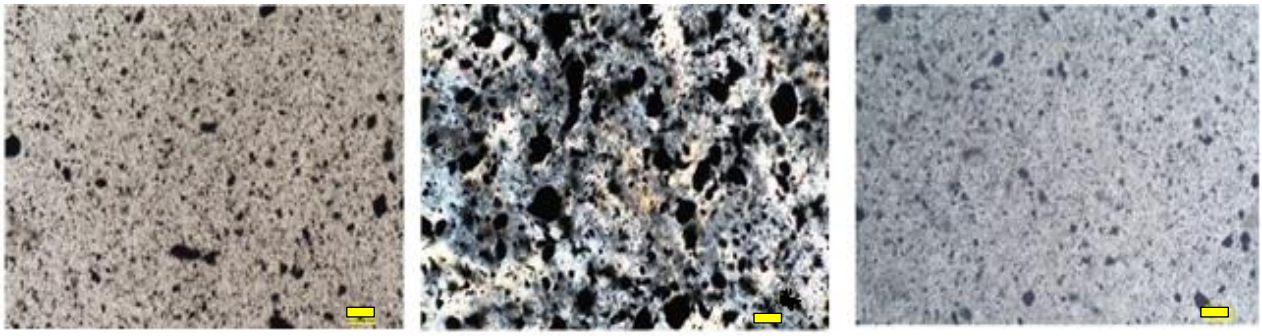

d. PP/SWNT composite (SFD) e. PP/PVP-SWNT composite (SFD) f. PP/SDS-SWNT composite (SFD)

Figure 4.9. Optical microscopy images for nanocomposites by Rotary evaporation method (a) PP/SWNT (b) PP/PVP-SWNT (c) PP/SDS-SWNT, and by spray freeze drying method (d) PP/SWNT (e) PP/PVP-SWNT (f) PP/SDS-SWNT. (scale bars -50 µm)

In the case of the spray freeze dried PP/SWNT and PP/SDS-SWNT nanocomposites shown in Figure 4.9 (d) and 4.9 (f) respectively, the dispersion state was more uniform compared to the rotary evaporated samples. During spray freeze drying, aqueous SWNT dispersion was frozen in the presence of liquid nitrogen and then followed by freeze drying, which helped in avoiding aggregation induced by capillary forces, as was observed during rotary evaporation. Additionally, spray freeze drying also prevented flake like aggregation induced during ice crystal formation, which is usually observed while freeze drying nanomaterial dispersions [90]. However, the spray

freeze dried PP/PVP-SWNT sample still showed bigger aggregates (Figure 4.9 (e)), similar to the rotary evaporated sample, which further supported PP-PVP incompatibility. The dispersion state for spray freeze dried PP/SDS-SWNT looked similar to that of PP/SWNT. The observed similarity in dispersion state might have been due to the poor SWNT dispersing ability of SDS at higher concentrations of 2 mg/ml, as was observed from its UV-Vis spectrum.

SEM images of spray freeze dried and rotary evaporated aqueous SWNT dispersions showed the difference in porosity and nanotube bundle size, as shown in Figures 4.10 and 4.11, respectively. All spray freeze dried aqueous SWNT dispersions had smaller and more porous bundles, as shown in Figure 4.10, whereas compact nanotube bundles (as a result of strong capillary and van der Waals forces) were observed for rotary evaporated samples, shown in Figure 4.11.

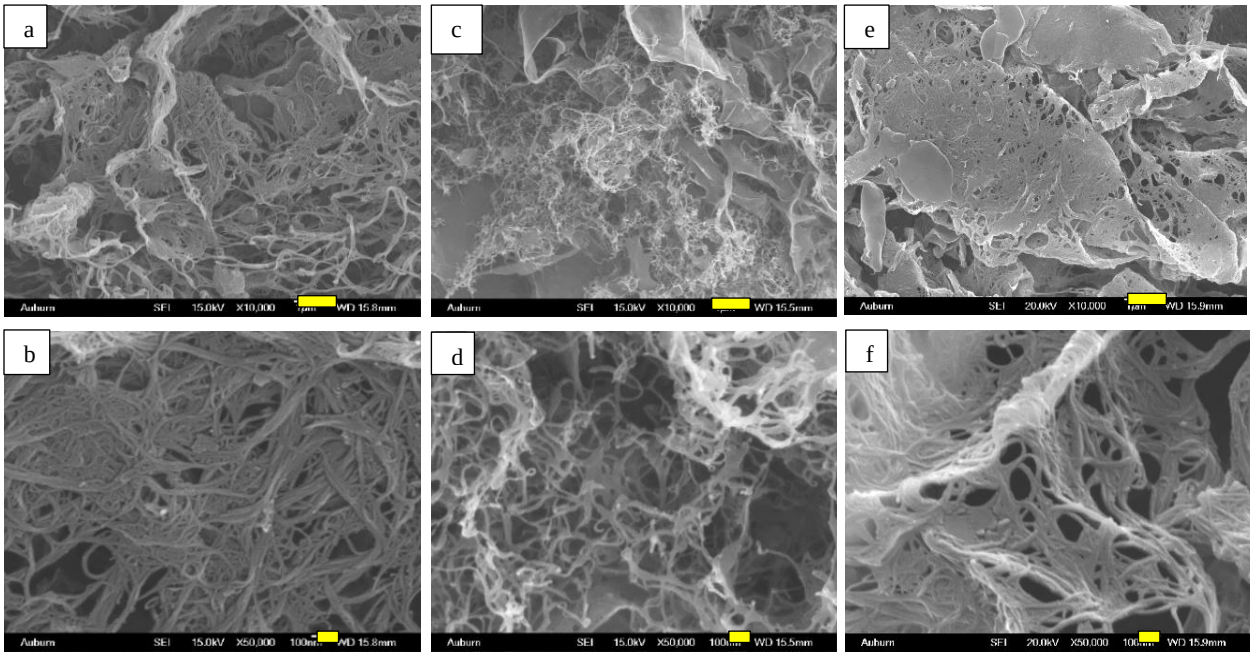

Figure 4.10. (a) and (b) spray freeze dried SWNT, (c) and (d) spray freeze dried PVP-SWNT, (e) and (f) spray freeze dried SDS-SWNT. (scale bars - 1 µm for (a),(c),(e) and 100 nm for (b), (d), (f))

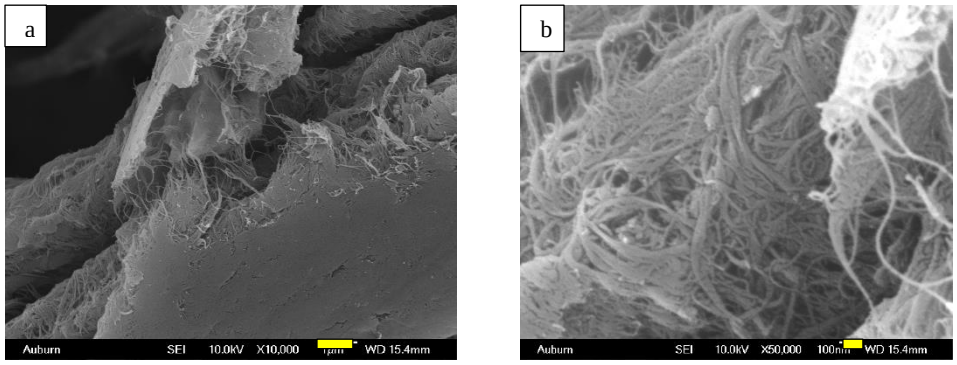

Figure 4.11. Vacuum dried SWNT-water dispersion (equivalent to rotary evaporation) (scale bars - 1 μm for (a) and 100 nm for (b)).

More porous structures in SWNT resulted in easier polymer melt infiltration during processing. Moreover, their low agglomerate strength assisted in breaking bigger aggregates due to applied shear, therefore achieving a much more uniform dispersion state of SWNT in the PP matrix. Figure 4.12 shows SEM images of PP/SWNT and PP/SDS-SWNT using the spray freeze drying method. Since SEM probes only a very small surface area, these images rendered any differences in dispersion state caused by SDS functionalized SWNT undiscernible.

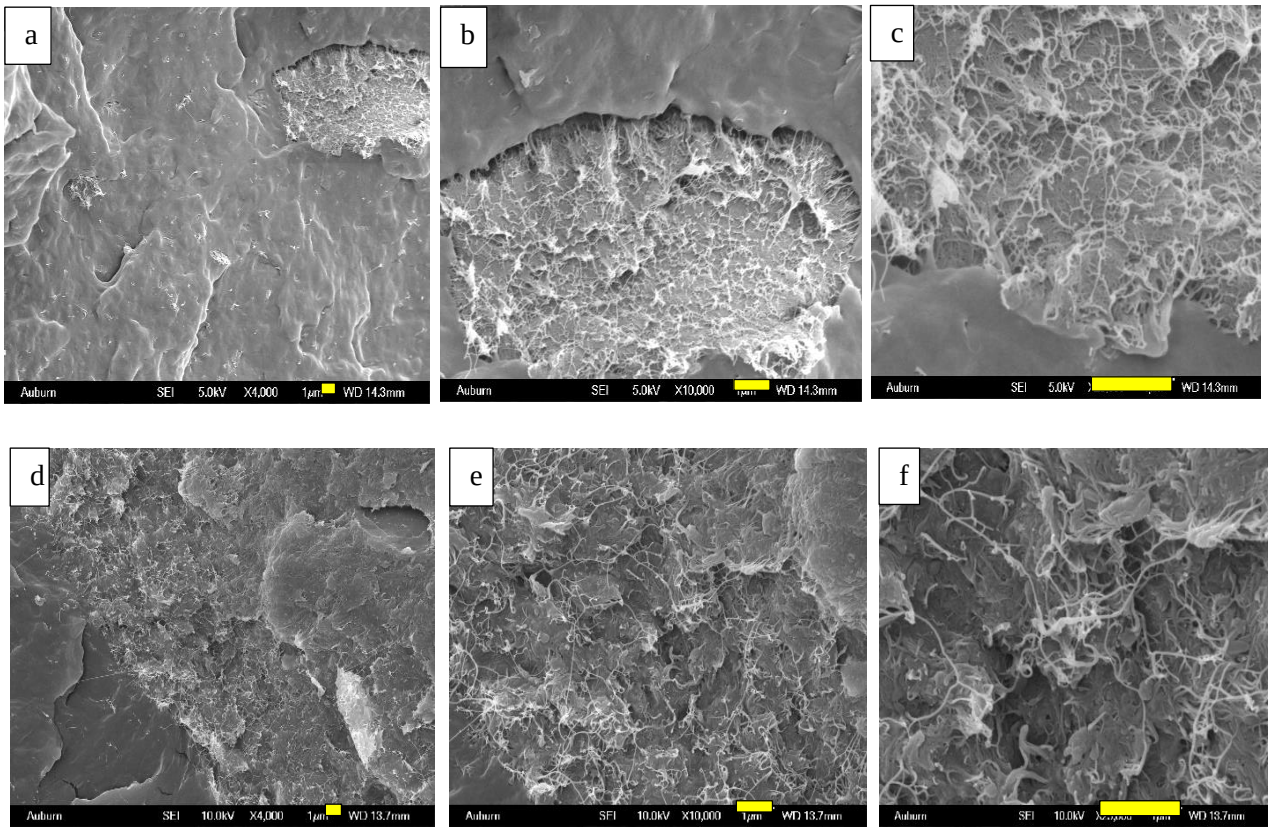

Figure 4.12. SEM images of melt extruded nanocomposites by spray freeze drying (a),(b) and (c) PP/SWNT, (d), (e) and (f) PP/SDS-SWNT nanocomposites. (all scale bars- 1 µm)

4.4 Rheology

Rheological behavior was more sensitive towards the microstructure of polymers and gave a better idea regarding the level of nanotube dispersion in the polymer matrix. The rheological behavior in terms of complex viscosity, storage modulus, loss modulus, and damping factor (ratio of loss modulus to storage modulus) was compared to gain a better understanding of the effect of non-covalent functionalization and pre-processing methods on nanocomposite properties.

Figure 4.13 (a) shows the dependence of complex viscosity on angular frequency within a linear viscoelastic limit. Complex viscosity is a measure of the resistance of the sample to an

oscillatory shear. The effect of non-covalent functionalization and pre-processing methods on the complex viscosity of PP nanocomposites was evident at low frequencies. PP/PVP and PP/SDS blends had a very slight influence on the complex viscosity of neat PP, so the effect of PVP and SDS on the rheological properties of PP will be not taken in account in the following discussion. In the case of rotary evaporated samples, a small enhancement in the complex viscosity η^* of PP/PVP-SWNT than PP/SWNT was indicative of poor dispersion and was consistent with their optical microscopy results. In contrast, the complex viscosity of the spray freeze dried nanocomposites at the same loading was much higher and showed a prominent shear thinning behavior at lower frequencies. This was resulted from the uniform nanotube microstructure formed inside the PP matrix. Such uniform nanotube microstructure was caused by the melt infiltration of polymer chains into porous spray freeze dried nanotube bundles during melt processing. Among these spray freeze dried nanocomposites, PP/SDS-SWNT showed only a slight improvement in complex viscosity over PP/SWNT. This small difference could have been due to favorable SDS-PP interactions, as the dispersion states for both of these nanocomposites looked similar and uniform in microscopic techniques.

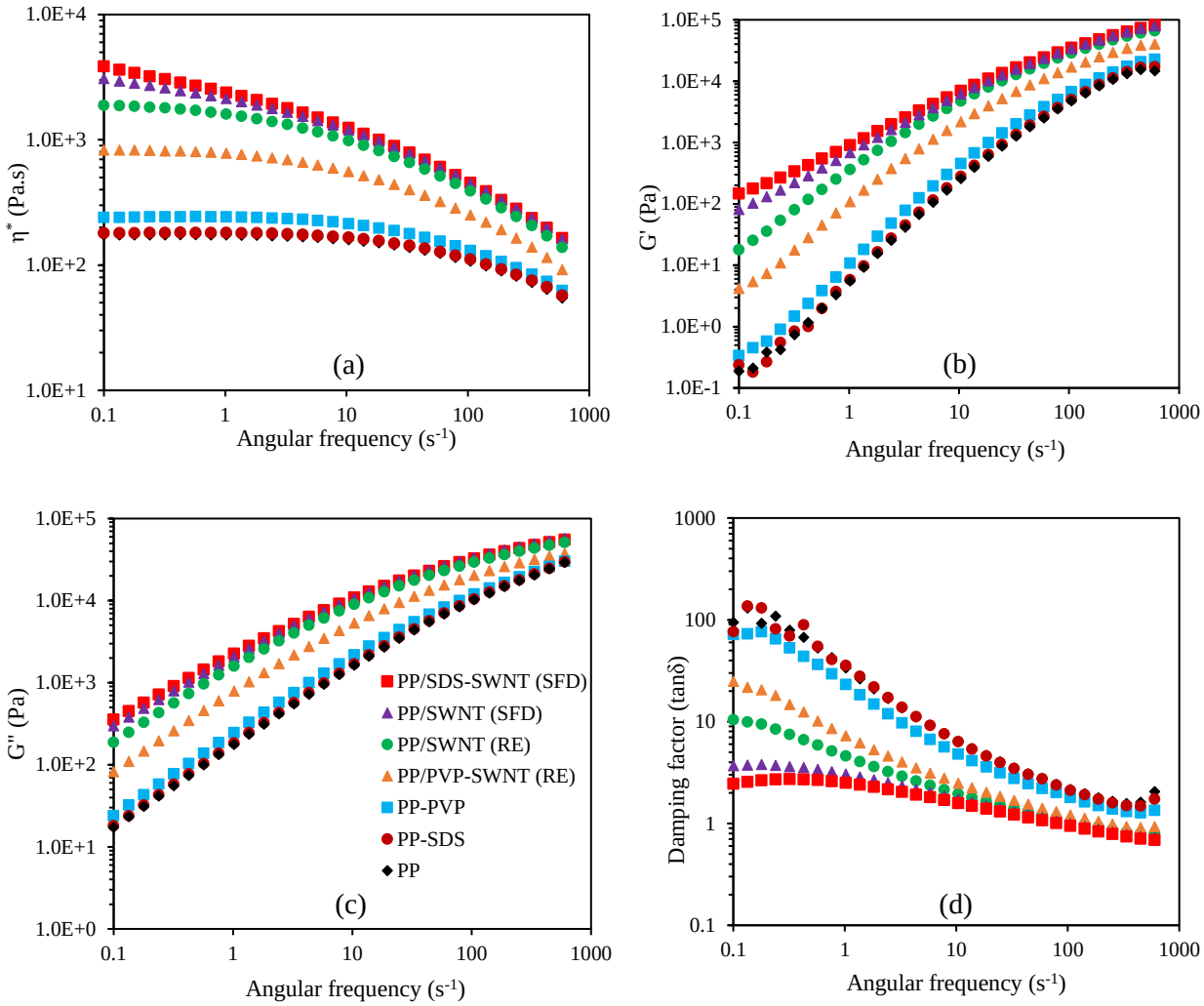

Figure 4.13. (a) Complex Viscosity, (b) Storage modulus, (c) Loss modulus, and (d) Damping factor as a function of angular frequency. Legends shown in 4.13(c) (same for all figures). (Error bars: < 15 %).

The frequency dependence of G' and G" can provide further insight into nanocomposite viscoelasticity. Lower frequencies probe longer time scales which are primarily related to the nanotubes and network formation and higher frequencies probe shorter time scales related to the polymer chains themselves. At low frequencies, PP chains were fully relaxed and exhibited a typical homopolymer-like terminal behavior with G′ roughly proportional to ω^2. However, upon the introduction of nanotubes in concentrations near percolation, this terminal behavior disappeared. The large-scale polymer relaxations in the nanocomposites were effectively restrained by the presence of SWNT. As shown in Figure 4.13 (b), non-terminal behavior was observed in the rotary evaporated PP/SWNT sample, as a result of an effective nanotube coating on the PP surface during its pre-processing. However, rotary evaporated PP/PVP-SWNT showed terminal behavior similar to neat PP and has only an order of magnitude increase in G' compared to neat PP, indicating the absence of an interconnected nanotube network. For all spray freeze dried nanocomposite samples, non-terminal behavior was prominent with ~3 orders of magnitude increase in G' with respect to neat PP, which was an indication of a highly interconnected nanotube network approaching percolation. Similar to the complex viscosity behavior, PP/SDS-SWNT showed a slight increase in low frequency storage modulus over PP/SWNT.

The low frequency dependence of G" (Figure 4.13(c)) showed a similar trend as G'; however, the corresponding increase in the loss modulus of nanocomposites was much lower than that of storage modulus. The damping factor ($\tan \delta = G''/ G'$), provides insight into the relative changes in G' and G" and is shown in Figure 4.13(d); it also provides information regarding the microstructure and interfacial interactions between the nanotubes and the PP matrix [115]. For all nanocomposites, $\tan \delta > 1$ at all frequencies; this indicates the dominance of the viscous response of the PP matrix. However, for the spray freeze dried nanocomposite samples, $\tan \delta$ was close to

1 at low frequencies, which was due to the increased elastic nature of these nanocomposites for long time scales. Moreover, the flatness of the tan δ versus the frequency curve for the spray freeze dried nanocomposite samples indicated significant interfacial interactions between its components. Hence, SDS-SWNT and PP interactions seemed to be more favorable than SWNT and PP interactions.

4.5 Thermal properties

Since SWNT are highly thermally stable, they were expected to improve the thermal stability of polypropylene by stabilizing the polymer chains against thermal energy and reducing the transport of decomposition products [116, 117]. Due to the semi-crystalline nature of PP, it was interesting to see the effect of SWNT on its crystallization behavior. Nanomaterials act as nucleating agents and influence the polymer crystallization process by improving their rate and temperature of crystallization [96].

Table 4.2 presents crystallization, melting temperatures, and crystallization kinetic parameters for PP nanocomposites processed at 190°C and 100 rpm for 30 minutes. Melting temperatures for both spray freeze dried and rotary evaporated nanocomposites showed an increase of only 2 – 4 °C. This small increase in T_m is very close to experimental error of the instrument, but would be consistent with some restriction of polymer chain mobility against the thermal energy in the presence of nanotubes. However, no particular trend was seen among the increased T_m of these samples, as the measurement error for T_m was itself around ±1 °C. Unlike T_m, the crystallization temperature of nanocomposites showed a larger increase compared to neat PP. This observed increment was in accordance with the SWNT dispersion state in these samples. Among rotary evaporated nanocomposites, the largest increase of 14 °C was found for PP/SWNT, while

PP/PVP-SWNT and PP/SDS-SWNT showed increases of 6 °C and 8 °C, respectively. For spray freeze dried nanocomposites, increase in T_c was higher than it was for rotary evaporated nanocomposites, due to a more uniform dispersion state of SWNT achieved in these nanocomposites. T_c was increased by 15 °C and 16 °C for spray freeze dried PP/SWNT and PP/SDS-SWNT, respectively. Spray freeze dried SDS-SWNT did not result in a significant increase in T_c over spray freeze dried pristine SWNT. An increment in the crystallization temperature was due to the presence nanotubes, which acted as heterogeneous nucleation sites during the primary crystallization stage and thus facilitated the PP crystallization at higher temperatures [96]. Similar results have been obtained by other researchers; for a loading of 0.5 vol.% Radhakrishnan et al. observed a 10 °C increase in T_c [25], with 1 wt.% SWNT Bhattacharyya et al. [95] observed an 11 °C increase in T_c, whereas Manchado et al. observed an increase of 5 °C [17].

Method	**Sample**	**T_c (°C)**	**T_m (°C)**	**$t_{1/2}$ (s) (at 133 °C)**	**ΔE_a (kJ/mol)**
	PP	116	162	259	344
RE	PP/SWNT	130	165	32	204
	PP/PVP-SWNT	124	164	131	337
	PP/SDS-SWNT	126	164	108	311
SFD	PP/SWNT	131	165	29	208
	PP/SDS-SWNT	132	166	22	137

Table 4.2. Crystallization and melting temperatures, crystallization half-times, and activation energies of melt extruded PP and nanocomposites. Error in T_c and T_m is about ±1 °C, Rotary evaporation (RE), Spray freeze drying (SFD).

Isothermal crystallization kinetics was studied using the Avrami equation (Equation 4.1), which relates the crystallized fraction of polymer (x) to the overall rate constant of crystallization (k), time (t) and Avrami exponent (n).

$$x = 1 - \exp(-k\,t^n) \tag{4.1}$$

$$\ln[-\ln(1 - x_t)] = \ln k + n \ln t \tag{4.2}$$

By plotting $\ln[-\ln(1 - x_t)]$ vs $\ln t$, the Avrami exponent (n) and crystallization rate constant (k) were obtained from its slope and intercept. The activation energy (E_a) of crystallization was evaluated by using an Arrhenius-type equation

$$\ln k = \ln k_0 - \frac{E_a}{R.\,T} \tag{4.3}$$

where k_0 is the frequency factor and R is the gas constant. The activation energy was calculated from the slope of ln k versus 1/T plot. Half crystallization time, $t_{1/2}$, is the time required to achieve 50% crystallization in the sample and was obtained from the modified form of equation 4.2, as shown below.

$$t_{1/2} = \left(\frac{\ln 2}{k}\right)^{\frac{1}{n}}$$

This analysis further aided the investigation of the effect of pre-processing methods and functionalization on PP nanocomposites. Table 4.2 shows $t_{1/2}$ and E_a values for the neat PP and its nanocomposites. $t_{1/2}$ was significantly reduced for nanocomposites, as compared to neat PP, indicating an enhanced rate of crystallization due to the presence of heterogeneous nucleation sites. The trend for $t_{1/2}$ was in accordance with the morphological and rheological results, as spray freeze dried samples showed faster crystallization rate than that of rotary evaporated samples. The improved SWNT dispersion in spray freeze dried nanocomposites resulted in more nucleation sites and a significant reduction in crystallization half time. As shown in Table 4.2, $t_{1/2}$ was only 22

seconds for spray freeze dried PP/SDS-SWNT, 108 s for the rotary evaporated PP/SDS-SWNT and 259 s for neat PP.

The activation energy of crystallization E_a is a measure of energy barrier to crystallization and is also affected by the presence of heterogeneous nucleation sites. The energy barrier for crystallization process reduces as a result of the presence of nanotubes; however, an increased viscosity and lower polymer chain mobility resulting from these well-dispersed nanotubes tend to increase E_a. The activation energy of crystallization for nanocomposites was lower than that for neat PP. This indicated that the crystallization of PP chains was significantly governed by the presence of heterogeneous nucleation sites and had compensated their lower polymer chain mobility during crystallization. E_a followed a similar trend as $t_{1/2}$, showing the lowest value of 137 kJ/mol for spray freeze dried PP/SDS-SWNT, which was followed by rotary evaporated nanocomposites, while neat PP had an activation energy of 344 kJ/mol.

Pre-processing method	**Sample**	**T_d**	**T_1**
	PP	404	463
RE	PP/PVP	407	463
	PP/SWNT	436	470
	PP/PVP-SWNT	416	464
	PP/SDS-SWNT	424	472
SFD	PP/SWNT	436	474
	PP/PVP-SWNT	421	466
	PP/SDS-SWNT	442	477

Table 4.3. Thermal decomposition (T_d) and temperature of maximum rate of weight% loss (T_1) for neat PP and nanocomposites. Rotary evaporation (RE), Spray freeze drying (SFD).

In order to observe the thermal stabilizing effect of nanotubes, a 5% weight loss temperature (T_d) and temperature of maximum rate of weight% loss (T_1) were measured, as shown in Table 4.3. The observed increase in T_d and T_1 of nanocomposites as compared to neat PP was due to the stabilization of PP chains in the SWNT/polymer interphase and the reduced transport of evolved decomposition products caused by presence of nanotubes [116, 117]. A uniform SWNT dispersion leads to larger interphase volume, as well as more complex nanotube network resulting in more PP chains being stabilized by the nanotubes. In this case, the higher values of T_d and T_1, for the nanocomposites made after spray freeze drying further supports that this preprocessing method resulted in more uniform SWNT dispersion than rotary evaporation or dry mixing. Among the rotary evaporated nanocomposites, a maximum increase of 32 $^{\circ}$C was observed for T_d of PP/SWNT, whereas for PP/PVP-SWNT, T_d was increased by 12 $^{\circ}$C, due to poorly dispersed SWNT in the PP matrix. Unlike PP-PVP, PP-SDS was found to be compatible, hence the slightly improved SWNT dispersion state in PP/SDS-SWNT resulting in a 20 $^{\circ}$C improvement in T_d. Spray freeze dried PP/SDS-SWNT nanocomposites showed the largest increase of 38 $^{\circ}$C, which was due to the stabilization of more PP chains through uniform dispersion state, which resulted from porous and functionalized SWNT. However, PP/SWNT nanocomposites in this case showed similar increase in T_d as rotary evaporated PP/SWNT nanocomposites.

4.6 Conclusions

This investigation showed that non-covalent functionalization and the type of pre-processing method for drying SWNT dispersion prior to melt processing have significant influences on their final dispersion states in PP, thereby influencing thermal and rheological properties. Morphological results showed that pristine and non-covalently functionalized SWNT dispersions

formed compact nanotube bundles upon rotary evaporation (equivalent to vacuum drying); this is likely due to action of capillary and van der Waals forces resulting in bigger nanotube aggregates upon processing. Also this aggregation effect was more prominent in non-covalently functionalized SWNT dispersion since the presence of dispersing agent make system more concentrated. Spray freeze drying of pristine and non-covalently functionalized SWNT dispersion formed porous nanotube bundles upon drying, thus enhancing the melt infiltration during processing. This resulted in a more uniform SWNT dispersion state in the final PP nanocomposites thereby enhancing rheological and thermal properties compared to PP nanocomposites by rotary evaporation method. Although optical microscopy revealed similar SWNT dispersion state for spray freeze dried PP/SDS-SWNT and PP/SWNT (which might be due to poor dispersing ability of SDS at higher SWNT concentrations), smaller enhancements in rheological and thermal properties of PP/SDS-SWNT were observed compared to PP/SWNT. Therefore, spray freeze drying is effective in reducing the aggregation induced by capillary and van der Waals forces during rotary evaporation. Hence, non-covalent functionalization of SWNT using an effective and compatible dispersing agent in conjunction with spray freeze drying can lead to greater improvements in nanocomposite properties.

Chapter 5

Polyvinylpyrrolidone functionalized SWNT – Poly (Ethylene-co-Vinyl alcohol) Nanocomposites

This chapter investigates the effect of polyvinylpyrrolidone (PVP) functionalized SWNT on thermal and rheological properties of poly(ethylene-co-vinyl alcohol) (EVOH) nanocomposites using spray freeze drying as pre-processing method. EVOH has been widely used in packaging as well as in high strength barrier materials for fuel tanks [5, 12, 13]; improving its mechanical and/or barrier properties could extend its potential range of applications. Most efforts to improve these properties by introduction of nanomaterials have been done using a solution processing method [118-120]. In this research, melt processed EVOH nanocomposites were prepared using PVP functionalized SWNT by employing a spray freeze drying technique during pre-processing step. As shown in the previous section, spray freeze drying is a promising pre-processing method for achieving a good SWNT dispersion state in polymer melts and was superior to the rotary evaporation method for the polypropylene composites investigated. PVP is an excellent non-ionic dispersing agent for SWNT and its compatibility with EVOH made it a promising choice for compatibilizing SWNT and EVOH. The results in this chapter show that PVP-SWNT nanocomposites had a more significant effect on EVOH rheological properties than pristine SWNT. The more uniform dispersion of SWNT in EVOH/PVP-SWNT led to a highly interconnected nanotube network than EVOH/SWNT resulting in higher low frequency complex

viscosity η^* and storage modulus G'. The thermal stability and crystallization behavior of EVOH was also influenced, with EVOH/PVP-SWNT achieving enhanced thermal stability and higher crystallization temperature than EVOH/SWNT.

5.1 Polyvinylpyrrolidone functionalized SWNT

SWNT were functionalized with PVP by using the procedure explained in Section 3.2.1. PVP functionalized SWNT were characterized using UV-vis spectroscopy as shown in Figure 5.1. The absorption peaks for the aqueous PVP-SWNT dispersion correspond to different chiralities of SWNT and is an indication of more individualization of SWNT bundles. No distinct peaks were observed in aqueous SWNT dispersion spectrum due to largely aggregated SWNT bundles.

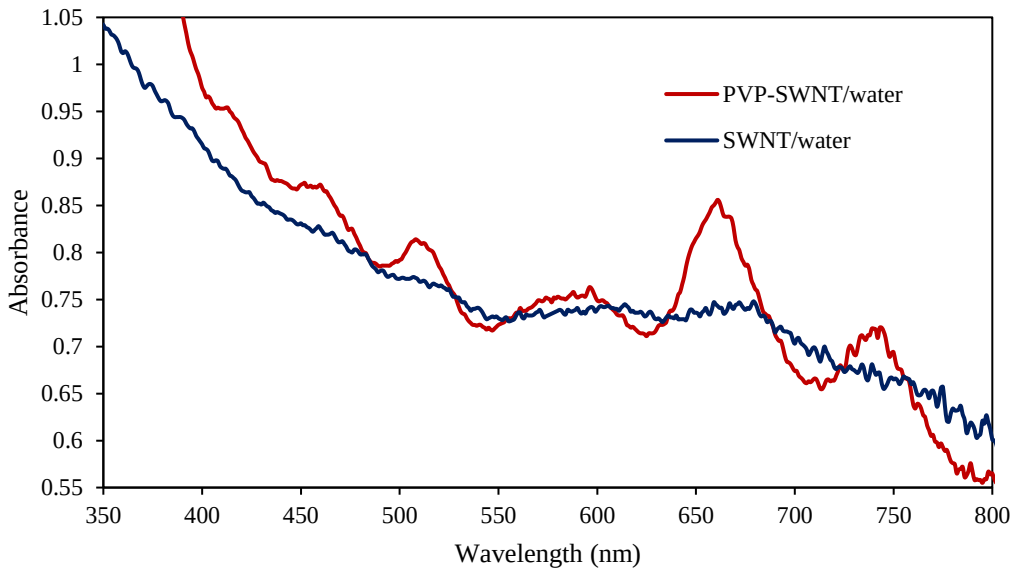

Figure 5.1. UV-Vis spectra for 2mg/ml PVP-SWNT/water and SWNT/water dispersions.

Thermogravimetric analysis of water rinsed PVP-SWNT was also carried out. As shown in Figure 5.2, the difference in weight loss between PVP-SWNT and SWNT TGA curves shows the degree of functionalization. The ~35 wt.% difference at the temperature of ~500°C (where all the PVP is decomposed) largely corresponds to non-covalently attached PVP on SWNT surface.

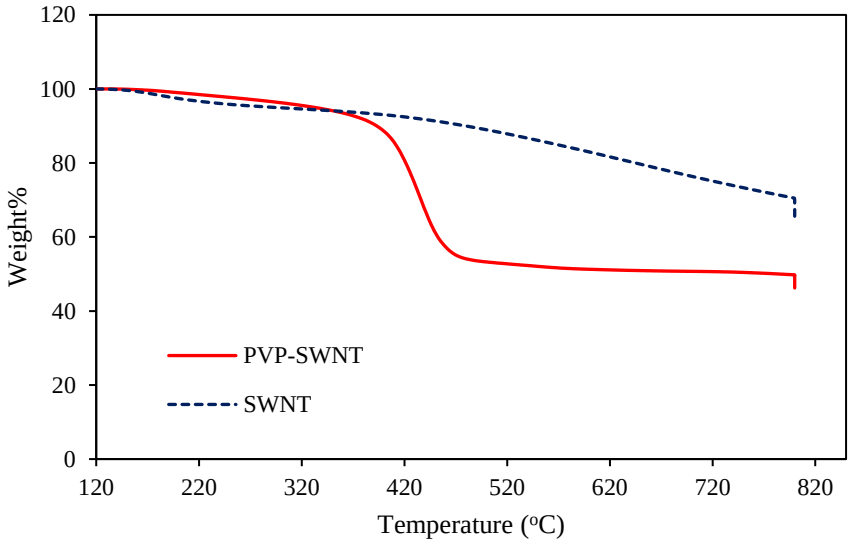

Figure 5.2. TGA curve for PVP functionalized and SWNTs in nitrogen medium.

5.2 Morphology

To achieve a good dispersion state of SWNT in EVOH, these two components need to be compatible. With PVP functionalization of SWNT the dispersion state is expected to be enhanced due to compatibility between PVP and EVOH. The compatibility of these two components was experimentally confirmed using method based on glass transition temperature, as shown in Figure 5.3. According to this method a compatible blend of polymer will show a single glass transition temperature which is between their individual glass transition temperatures. PVP-EVOH blend

exhibited a glass transition T_g = 79 °C which was between that of PVP (T_g = 164 °C) and EVOH (T_g = 49°C) [113]. The EVOH grade used in this research had 52 mol.% vinyl alcohol content which can interact strongly with PVP. The pyrrolidone rings in PVP contain a proton accepting carbonyl moiety, while vinyl alcohol presents hydroxyl group as side group. Therefore, a hydrogen-bonding interaction can take place between these two chemical moieties. Several researchers have studied miscibility of PVA and PVP due to such interactions [121-124]. Zhang et al. reported a significant improvement in tensile yield strength and Young's modulus of 5 wt.% PVP functionalized SWNT and PVA nanocomposites [125]. A similar hydrogen bonding interaction between graphene oxide and EVOH has also led to improved mechanical properties. Yang et al. have found 280% and 400% increase in tensile strength and Young's modulus, respectively for 4 wt. % EVOH/TRG (thermally reduced graphene) nanocomposites [118]. Kim et al. showed a 4 °C improvement in T_g as well as 103% increase in tensile moduli of 0.5 wt.% EVOH/GrO (graphene oxide) nanocomposites [119]. In both of these cases, the EVOH-filler interaction was through hydrogen bonding between hydroxyl in EVOH and oxygen containing TRG and graphene oxide.

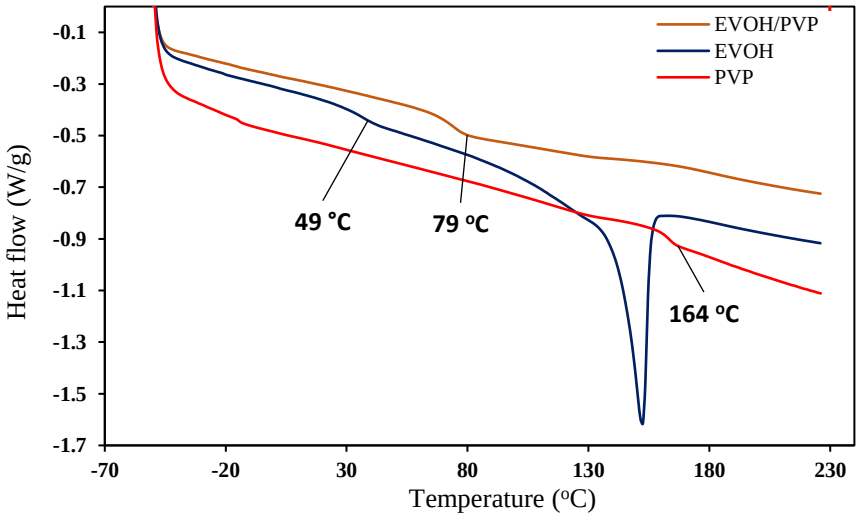

Figure 5.3. DSC thermograms for PVP, EVOH and EVOH/PVP.

As shown in Figure 5.4 (a) and 5.4 (b) optical microscopy images of EVOH/SWNT and EVOH/PVP-SWNT nanocomposites prepared through spray freeze drying showed highly uniform dispersion state with only few aggregates of size ~10-20 µm. In accord with previous findings, rotary evaporated EVOH nanocomposites depicted in Figure 5.4 (c) and (d) showed poor dispersion state compared to spray freeze dried nanocomposites. Unlike for PP nanocomposites, the rotary evaporated EVOH/PVP-SWNT did not have dramatically worse dispersion than rotary evaporated EVOH/SWNT; this may be due to the compatibility between EVOH and PVP. SEM images for EVOH/SWNT and EVOH/PVP-SWNT in Figure 5.5, show uniformly dispersed SWNT bundles in both these nanocomposites without any noticeable difference.

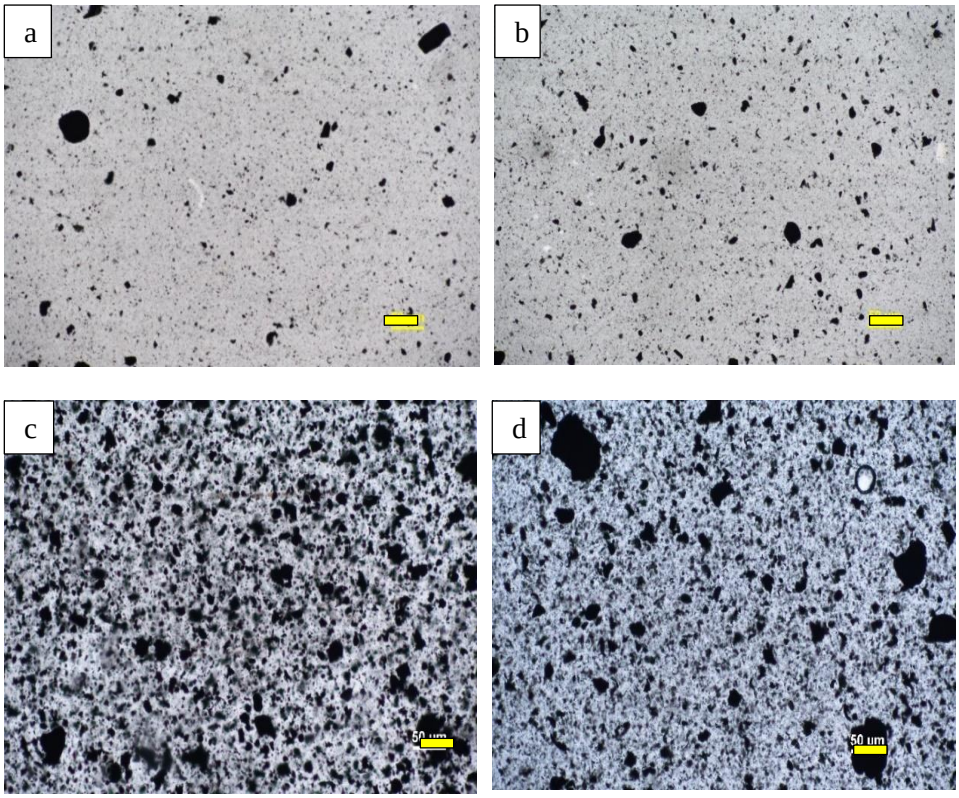

Figure 5.4. Optical images for EVOH nanocomposites extruded at 190 ˚C, 100 rpm, 30 min (0.75 vol.% SWNT). (a) EVOH/SWNT (SFD), (b) EVOH /PVP-SWNT(SFD), (c) EVOH/SWNT (RE), (d) EVOH/PVP-SWNT (RE). (scale bars - 50 µm)

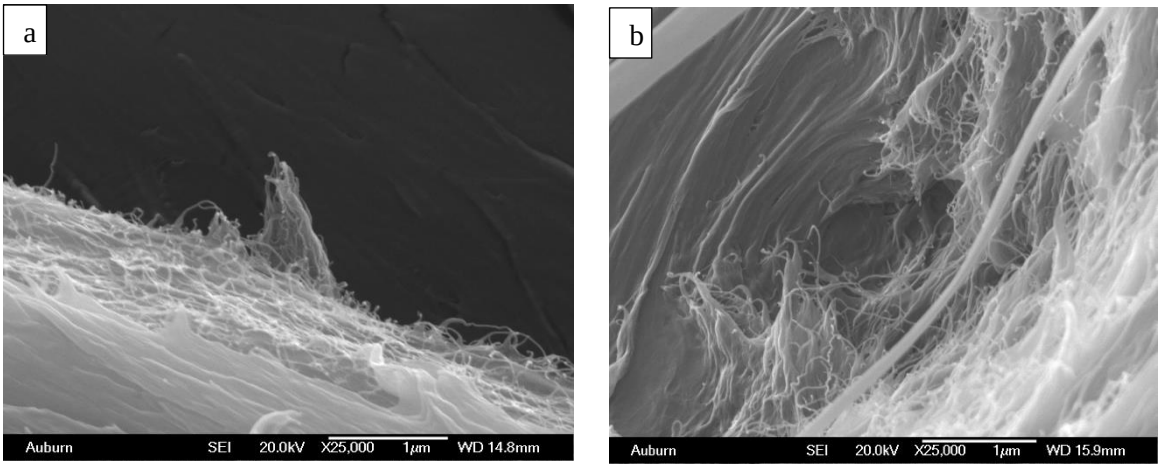

Figure 5.5. SEM images of (0.75 vol.%) EVOH nanocomposites through spray freeze drying extruded at 190 ^{0}C, 100 rpm, 30 min (a) EVOH/SWNT (b) EVOH/PVP-SWNT (scale bars-1μm)

5.3 Rheology

Although PVP is better dispersing agent, no considerable difference was observed between dispersion state of spray freeze dried EVOH/SWNT and EVOH/PVP-SWNT from microscopy techniques. However, a difference could be distinguished based on the more sensitive rheological characterization. Rheological characterization is more sensitive towards microstructure of polymer and especially its low frequency behavior is helpful in comparing SWNT dispersion state inside the polymer matrix. As depicted in Figure 5.6 (a), both EVOH/PVP-SWNT and EVOH/SWNT demonstrated a solid-like behavior at low frequencies characterized by a continuous increase in complex viscosity as frequency decreases, indicating the presence of a SWNT network structure. This characteristic gives the material a better resistance against the applied deformation at a low frequency.

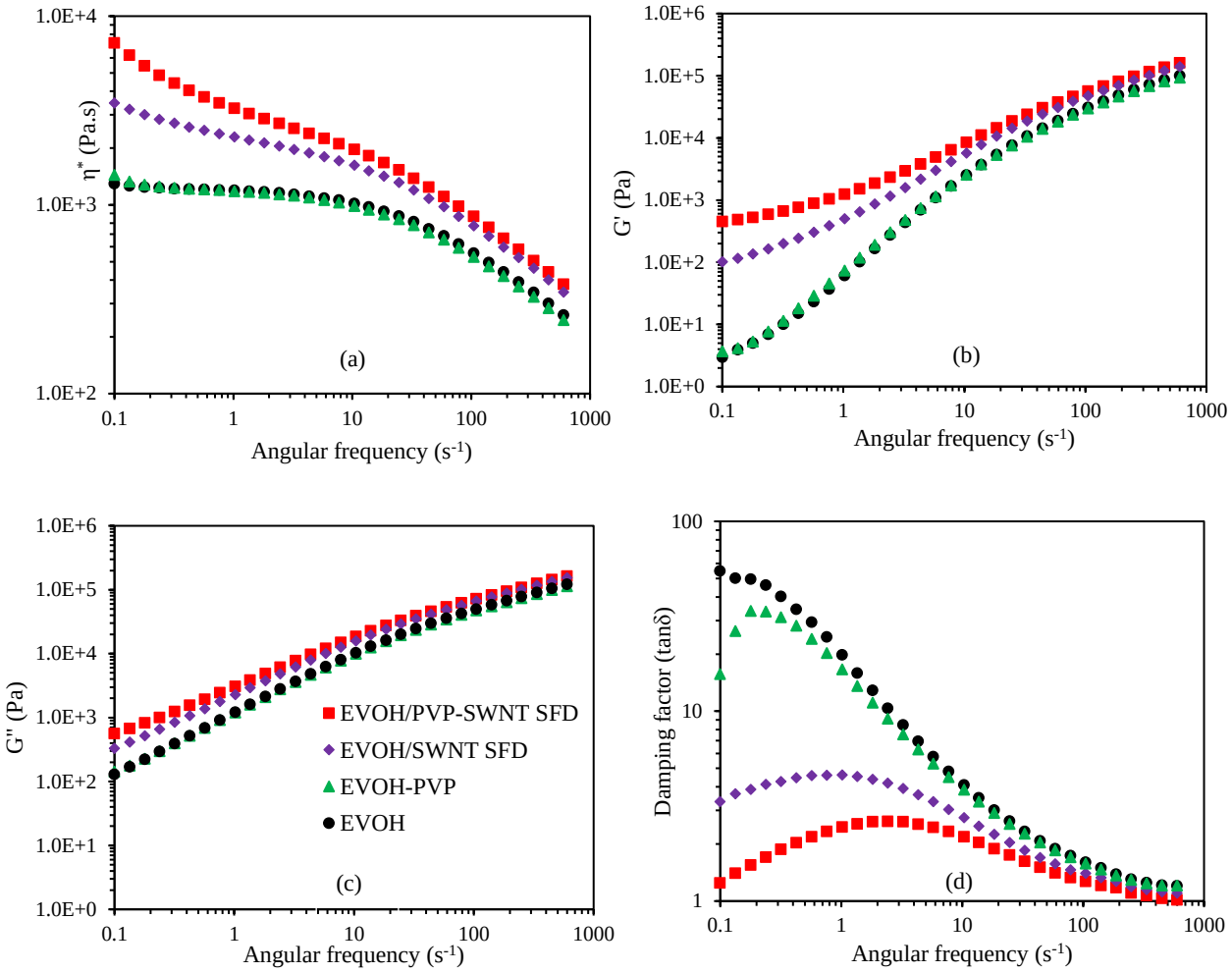

Figure 5.6. (a) Complex Viscosity, (b) Storage modulus, (c) loss modulus, and (d) Damping factor as a function of angular frequency (Error bars < 15%). Legends shown in 5.6 (c) (same for all figures).

The EVOH/PVP-SWNT complex viscosity η^* increased by ~ 400% while the EVOH/SWNT viscosity increased by ~170% relative to the neat EVOH. Figure 5.6 (b) showed a flattening in a low-frequency regime of storage modulus with three orders of magnitude increase in G' for EVOH/PVP-SWNT, which was an indicative of the onset of rheological percolation of the PVP-SWNT. However, this effect was less prominent in EVOH/SWNT. It should be noted

that EVOH/PVP blend did not show any effect on rheological properties. Hence, the effect of small concentrations of PVP (0.75 vol.%) used along with SWNT was considered to be negligible. Damping factor versus frequency plots shown in Figure 5.6 (d) helped in understanding the interfacial interaction between the nanotube network and EVOH matrix, flatter damping factor curves are indicative of interfacial interaction. Thus, a considerable interaction was evident between EVOH and PVP-SWNT compared to EVOH and SWNT due to a distinct difference in their damping factor curves. Differences in nanocomposite microstructure was also evident from the Cole-Cole plot shown in Figure 5.7. The neat EVOH and EVOH/PVP showed a linear relationship between G′ and G″ typical of polymer melts. While all nanocomposites showed a deviation from the linearity with greatest deviation observed for the EVOH/PVP-SWNT indicating more solid like behavior due to presence of a highly complex microstructure.

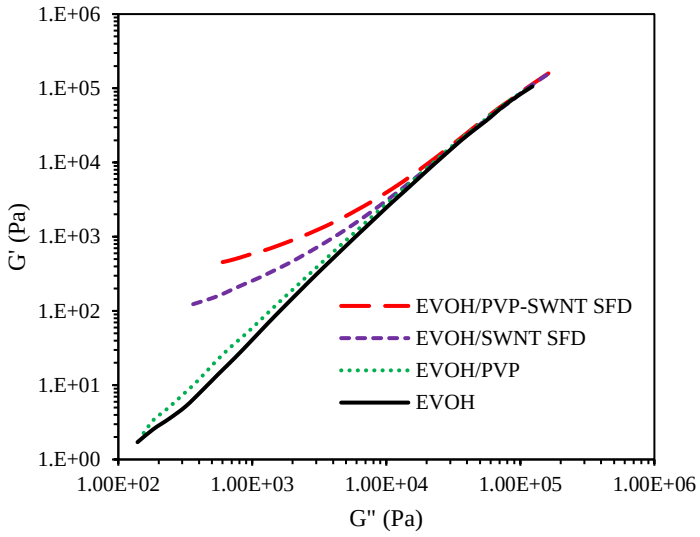

Figure 5.7. Cole-Cole plot for EVOH nanocomposites.

5.4 Thermal Properties

Thermal stability and crystallization behavior of EVOH are important for processing and end use applications. The addition of SWNT is expected to improve the thermal stability of the polymer through interphase stabilization of polymer chains and reducing transport of evolved decomposition products. EVOH shows multistep decomposition behavior, with vinyl component decomposing below 400 ˚C and a more stable ethylene component decomposing above 400 ˚C as shown in Figures 5.8 and 5.9.

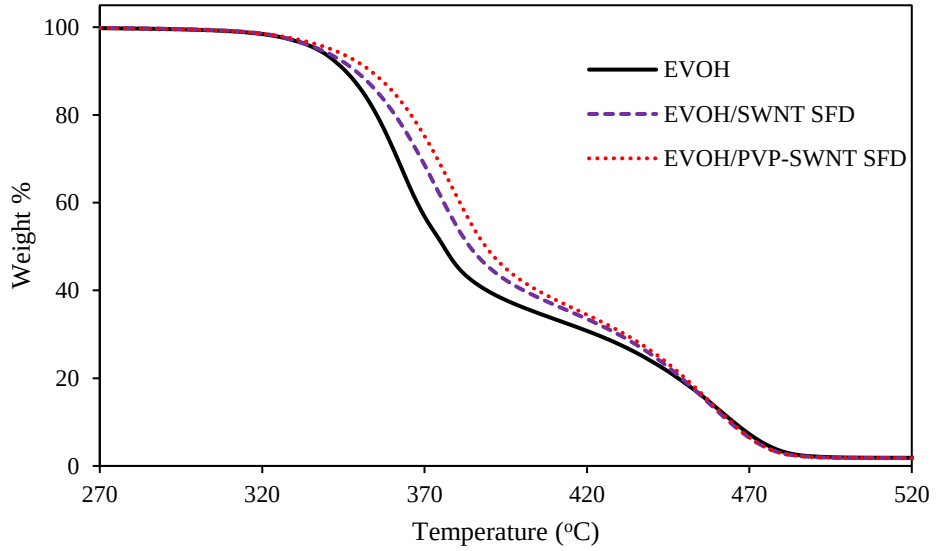

Figure 5.8. TGA curves for neat EVOH and 0.75 vol.% EVOH nanocomposites extruded at 190°C,100 rpm, 30 minutes.

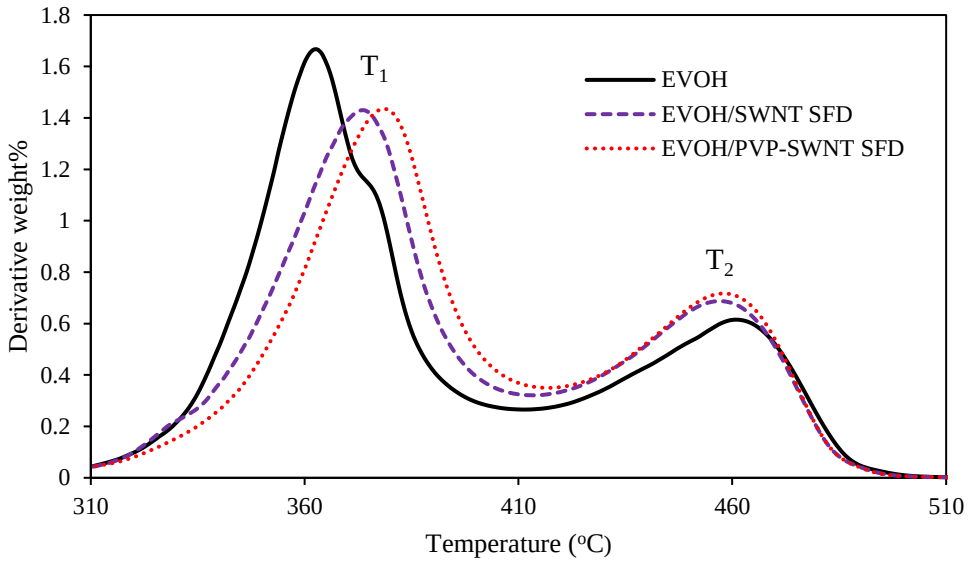

Figure 5.9. Derivative weight % vs temperature plots for neat EVOH and 0.75 vol.% EVOH nanocomposites extruded at 190 °C,100 rpm, 30 minutes.

Thermal stability of EVOH nanocomposites was measured in terms of the temperatures at which there was maximum rate of weight loss. The peak temperatures T_1 and T_2 (Figure 5.9) corresponding to decomposition of vinyl and ethylene components respectively are tabulated in Table 5.1. The stabilizing effect of SWNT on the vinyl component of EVOH was seen from the 12 °C increase in T_1 for the EVOH/PVP-SWNT and 9 °C increase for EVOH/SWNT. These results were consistent with the rheological behavior as discussed in previous section. The temperature T_2, largely corresponding to ethylene decomposition, was not affected by the presence of SWNT. This might be due to poor interaction of PVP with ethylene component in EVOH. Similar behavior was seen in case polyethylene-MWNT nanocomposites where temperature of maximum rate of weight loss was unaffected by addition of different concentrations of MWNT [126].

Sample	Temperature of maximum rate of weight % loss	
	T_1	T_2
EVOH	367	459
EVOH/SWNT (SFD)	376	458
EVOH/PVP-SWNT (SFD)	379	458

Table 5.1. Temperature of maximum rate of weight % loss for neat EVOH and 0.75 vol.% EVOH Nanocomposites.

EVOH is a semi crystalline polymer and incorporation of SWNT should influence its crystallization behavior. As shown in Figure 5.10, a slight increase of 2 to 3 $^{\circ}$C in EVOH nanocomposites crystallization temperatures was observed due to SWNT providing nucleation sites for crystal growth of EVOH polymer chains. Also a ~ 3 $^{\circ}$C increase in glass transition temperature of both nanocomposites was due to the confined mobility of EVOH chains at the EVOH-SWNT interphase. As shown in Table 5.2, there were no clear trends for nanocomposite T_g and T_c. However, melting temperature of EVOH was unaffected by the presence of SWNT.

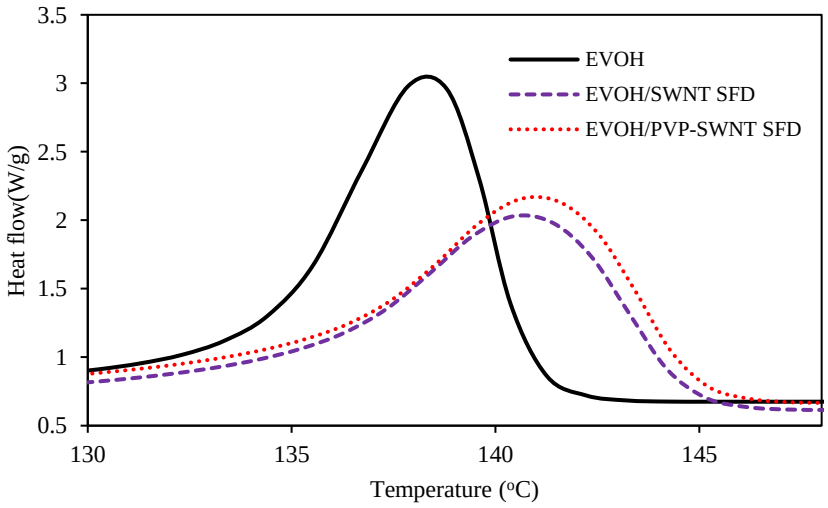

Figure 5.10. DSC thermograms showing crystallization peaks of EVOH nanocomposites.

Sample	T_g (°C)	T_m (°C)	T_c (°C)	H_c (J/g)	H_m (J/g)	% Crystallinity
EVOH	47.8	158	138	59.9	54	42.1
EVOH/SWNT **(SFD)**	51.0	157	140	50.1	46.5	36.6
EVOH/PVP-SWNT **(SFD)**	51.0	158	141	53.6	49	37

Table 5.2. Thermal properties of EVOH nanocomposites. Glass transition temperature (T_g), Melting temperature (T_m), Crystallization temperature (T_c), Enthalpy of crystallization (H_c), Enthalpy of fusion (H_m).

The percent crystallinity of EVOH nanocomposites was reduced due to the presence of SWNT which hindered the regular packing of the EVOH chains into crystal lattices, eventually leading to the diminished crystallite size. Percent crystallinity (X_c) values shown in Table 5.2 were calculated by using equation 5.1

$$X_c = \frac{\Delta H_m}{\Delta H_{m,EVOH}(1-W_f)} \times 100 \quad (5.1)$$

Where, ΔH_m is an enthalpy of melting of the sample and $\Delta H_{m,EVOH}$ is an enthalpy of melting when the sample is 100% crystalline, which was taken as 128.1 J/g [119]. W_f is weight fraction of nanotubes. Such reduction in crystallinity of EVOH caused by the incorporation of nanofillers has also been reported for EVOH/Graphene oxide nanocomposites [119].

5.5 Conclusions

Melt processed EVOH nanocomposites with increased thermal stability and rheological properties (low frequency complex viscosity η^* and storage modulus G') were produced by incorporation of spray freeze dried PVP functionalized SWNT and pristine SWNT. Uniform SWNT dispersion states were achieved in EVOH/PVP-SWNT as well as EVOH/SWNT, significantly increasing

thermal and rheological properties of EVOH. Morphological results did not show difference between EVOH/PVP-SWNT and EVOH/SWNT as was expected due to compatibility between EVOH and PVP. However, thermal and rheological properties of EVOH/PVP-SWNT increased compared to EVOH/SWNT. Higher complex viscosity, storage modulus and thermal stability of the vinyl component in EVOH/PVP-SWNT were the results of better interaction between the vinyl component of EVOH and PVP-SWNT. These enhanced properties of EVOH/PVP-SWNT, suggests that the spray freeze dried PVP functionalized SWNT would be more favorable for the achievement of EVOH-based nanocomposites with increased phase compatibility, thermal and rheological properties.

Chapter 6

Polylactic Acid-Cellulose Nanocrystal Nanocomposites

This chapter explores the direct comparison of some of the most promising methods to produce PLA/CNC nanocomposites based on their thermal and rheological properties. Melt-processed PLA/CNC nanocomposites have been in nascent stage as most efforts have currently been based on the solution processing [45, 108, 127, 128]. Melt processing of PLA/CNC nanocomposites is challenging since the temperature and moisture sensitivity of PLA lead to their degradation during processing. Furthermore, the hydrophobic nature of CNC makes its dispersion difficult in the hydrophilic PLA matrix. To address these issues during melt processing of PLA/CNC nanocomposites, several researchers have employed various methods. Arias et al. studied the effect of applying a miscible carrier with CNC on the morphology, thermal and mechanical properties of PLA/CNC nanocomposites. According to their findings, improved dispersion state was reported using larger PEO/CNC ratios with a noticeable increase in crystallization rate and temperature [24]. Jonoobi et al. used a similar approach using PLA by itself as a carrier for CNC by making PLA/CNC master-batches followed by its melt processing with PLA. They proved that a relatively good dispersion was achieved with enhancing the mechanical properties of final nanocomposites [129]. Khoshkava et al. have prepared PLA nanocomposites using spray freeze-dried CNC and have observed a significant effect on rheological properties of PLA caused by the uniform

dispersion of porous spray freeze-dried CNC [27]. Although various promising methods for preparing the melt-processed PLA/CNC nanocomposites were utilized, it was difficult to compare their results because of the differences in materials used and the processing conditions employed.

In this research, various promising pre-processing methods such as spray drying, freeze drying, spray freeze-drying, and master-batch mixing have been used to prepare PLA/CNC nanocomposites and eventually the morphology, thermal and rheological results of these nanocomposites were compared with solution processed PLA/CNC nanocomposites with similar CNC loading. The detailed experimental materials and procedure employed were described in section 3.4.

6.1 Morphology

6.1.1 Comparison of different CNC types

To compare the effect of CNC types with different surface chemistries on the dispersion state and compatibility with PLA matrix, three different types of CNC were used in this study. Regular unmodified CNC (CNC), sulfonated CNC (SA-CNC) with negatively charged sulfate group and hydrophobic lignin coated CNC (L-CNC). L-CNC is hydrophobic in nature due to the presence of non-covalently attached hydrophobic lignin group on its surface.

For this investigation, all nanocomposites were prepared by extruding PLA with different spray-dried CNC obtained from their aqueous dispersions. Figure 6.1, 6.2 and 6.3 show SEM images of 8 wt.% nanocomposites of PLA and unmodified, sulfonated and lignin coated CNC, respectively. It was observed that 8 wt.% PLA/CNC and PLA/L-CNC nanocomposites showed the aggregates of the size 20 to 50 µm, whereas PLA/SA-CNC had a relatively smaller aggregates of size less than 10 µm. The difference was mainly due to spray drying process which produces

particles of size 2-25 µm in the case of true solutions and those of greater than 25 µm for suspensions [106]. Since SA-CNC are easily soluble in water and form a uniform and stable dispersion due to the presence of negatively-charged sulfate groups on their surfaces, it has resulted in smaller particle sizes and hence the smaller aggregates in the final nanocomposites. Regular CNC and L-CNC, on the other hand, were poorly dispersed in water forming suspensions with bigger particle sizes thereby bigger aggregates in the nanocomposites. Regular CNC/water dispersion was at least kinetically stable until spray drying because of the presence of hydroxyl groups interacting with water, whereas L-CNC/water dispersion settled down soon after sonication was stopped and has to be continuously stirred during spray drying to keep the L-CNC in suspension.

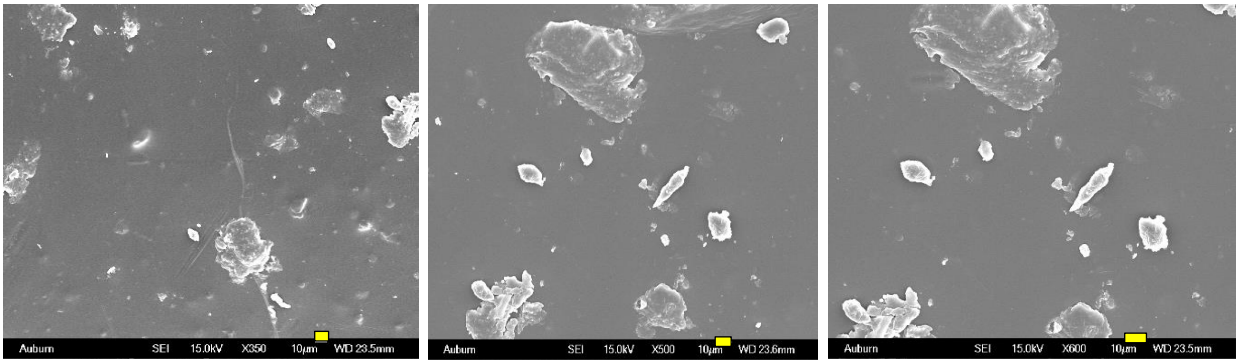

Figure 6.1. SEM images for 8 wt.% PLA/CNCSD (spray dried). (scale bars -10 µm)

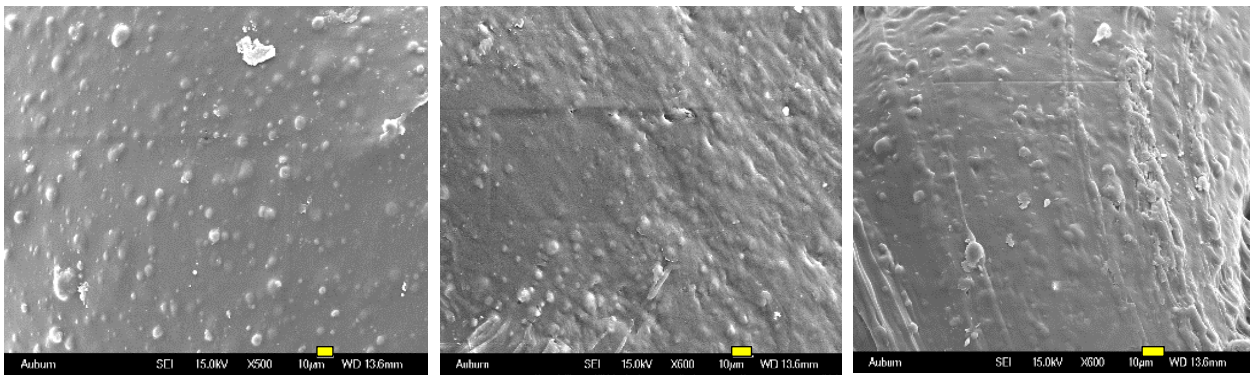

Figure 6.2. SEM images for 8 wt.% PLA/SA-CNCSD (spray dried). (scale bars -10 µm)

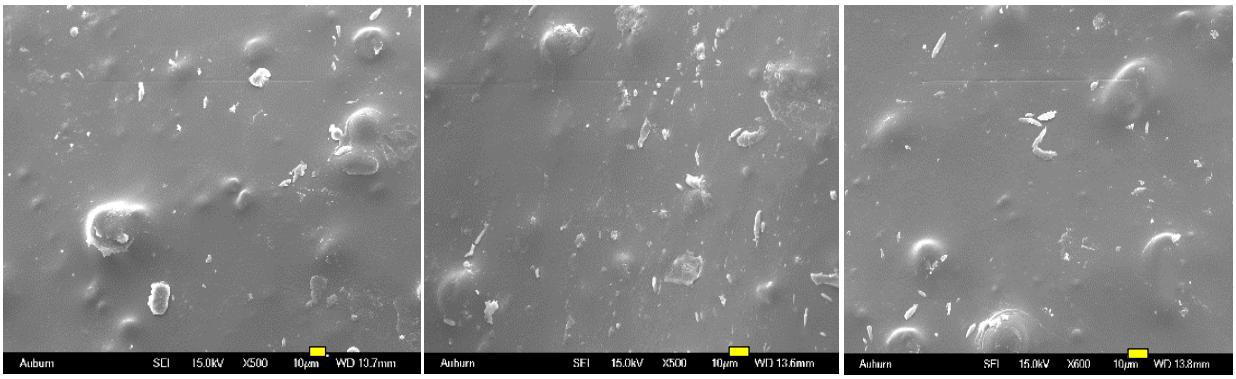

Figure 6.3. SEM images for 8 wt.% PLA/L-CNCSD (spray dried). (scale bars -10 µm)

Lignin coated CNC were expected to be compatible with the PLA matrix due to its hydrophobic nature [45, 130]. However, it was hard to penetrate compact CNC particles produced during spray drying. The spray drying was carried out under vacuum with the temperature above the boiling point of water. The rapid evaporation of water from atomized droplets created large capillary and van der Waal forces on CNC particles pulling them together resulting in compact aggregates. Such aggregates were not easily re-dispersible in PLA matrix since melt infiltration of the polymer became difficult due to high agglomerate strength and absence of porosity in these particles. Due to a relatively more uniform dispersion state obtained in PLA/SA-CNC nanocomposites, SA-CNC was used in further research to improve its dispersion and hence rheological and thermal properties of PLA through various pre-processing approaches.

6.1.2 PLA/SA-CNC nanocomposites through freeze drying

Freeze drying was used to avoid the compact aggregate formation due to capillary forces observed during spray drying. In this procedure, rapid freezing of CNC/water dispersion in liquid nitrogen was carried out before freeze drying to reduce flake-like aggregates induced by ice crystal formation. This type of aggregation was observed upon slow cooling of dispersion before freeze drying resulting in a poor dispersion state in final nanocomposites [90]. Due to this change, a more

uniform dispersion state of SA-CNC in PLA compared to spray-dried SA-CNC was achieved as shown in Figure 6.4 with the average aggregate size ranging between 5-10 µm. Capillary forces were reduced during freeze drying, which was evident from the porous structure of freeze dried CNC. However, significant van der Waal forces prevalent in highly interconnected network of freeze dried CNC could not overcome by applied shear during processing and has led to smaller aggregates in final nanocomposites.

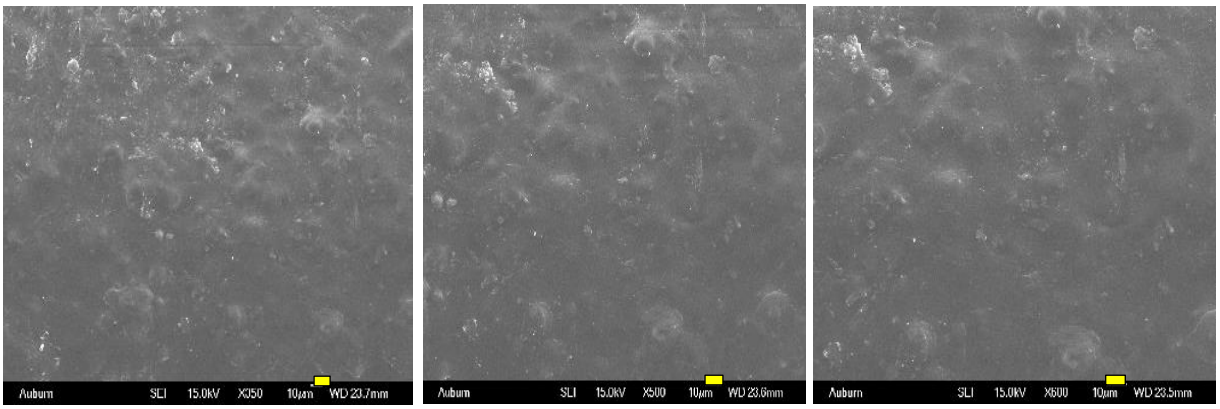

Figure 6.4. SEM images of 8 wt.% PLA/SA-CNCFD (Freeze dried). (scale bars- 10 µm)

6.1.3 PLA/SA-CNC nanocomposites through spray freeze drying

Spray freeze-drying technique was employed as utilized for PP and EVOH nanocomposites in the earlier work. Spray freeze drying is expected to improve the dispersion state of CNC in PLA by reducing the compact aggregates caused due to the capillary and van der Waals forces during spray drying as well as the flake like aggregates induced by ice crystal formation during freeze drying. Khoshkava et al have obtained highly porous CNC particles upon spray freeze drying CNC/water dispersion [90]. Nanocomposites produced from melt processing of spray freeze-dried powder of CNC and PLA have resulted in the highly uniform dispersion of CNC in PLA matrix with aggregates' size less than 5 µm.

SEM images shown in Figure 6.5, display a remarkable difference regarding porosity of spray freeze-dried CNC and spray dried CNC. The pore size of the order of ~ 0.1 µm was observed in spray freeze dried samples whereas spray dried CNC had compact particles with 10 to 20 µm in size.

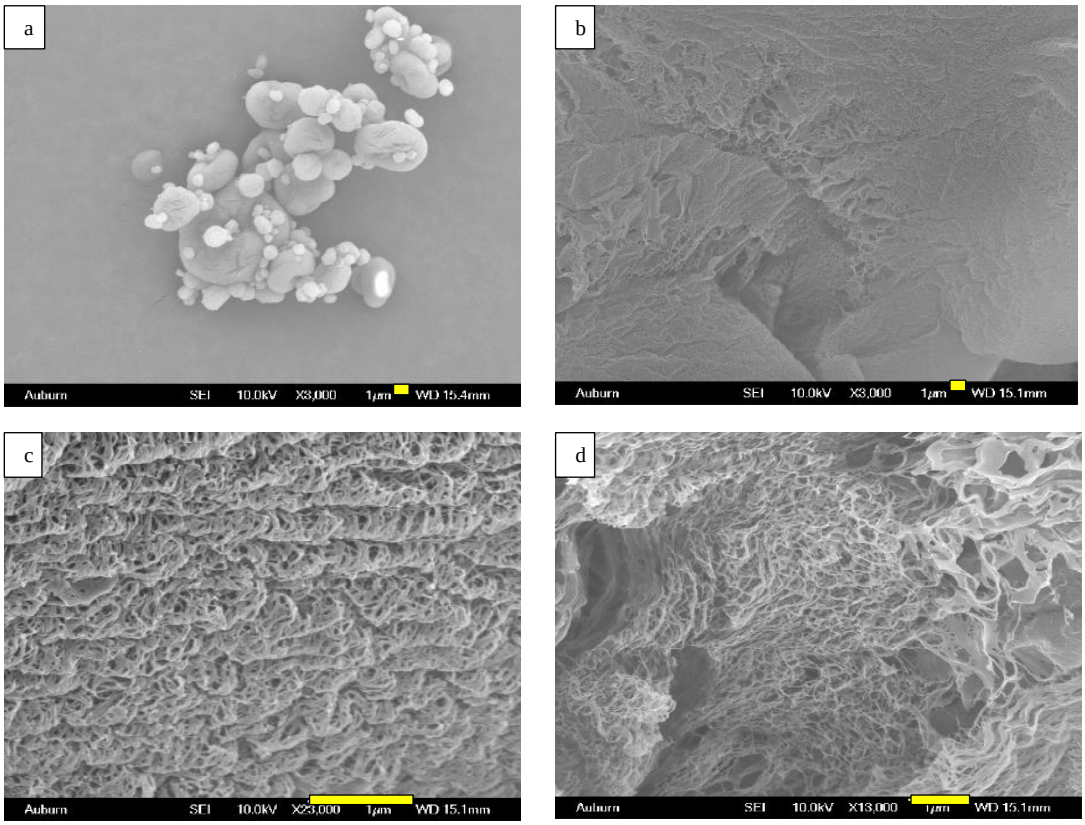

Figure 6.5. SEM images for (a) Spray dried SA-CNC, (b), (c) and (d) Spray freeze dried SA-CNC from 3 wt.% SA-CNC dispersion in water. (all scale bars- 1 µm)

The micro porosity in spray freeze-dried samples leads to an easier PLA melt infiltration into these pores and eventually resulting in improved rheological properties described in the following section. SEM images of 8 wt.% spray freeze-dried CNC, and PLA nanocomposite are

shown in Figure 6.6; a uniform dispersion of SA-CNC was observed with an average aggregate size lower than 10 µm.

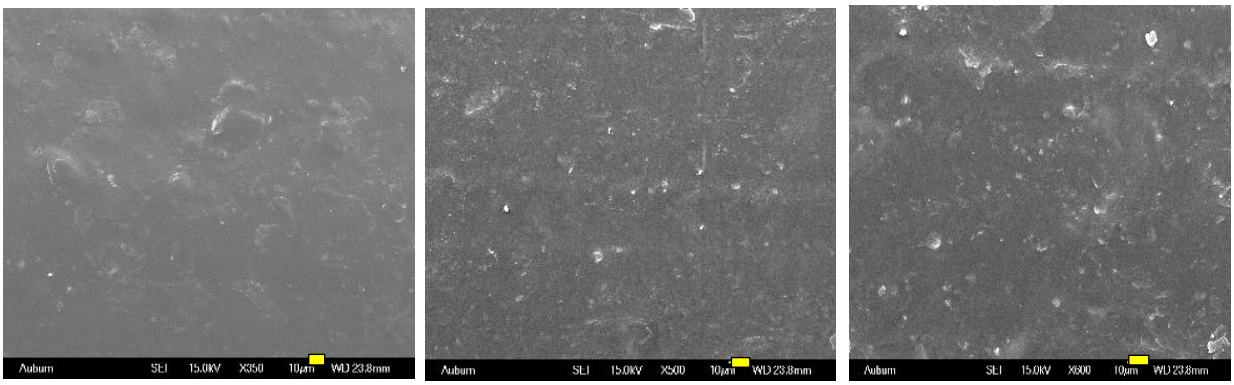

Figure 6.6. SEM images of 8 wt.% PLA/SA-CNCSFD (spray freeze dried). (scale bars- 10 µm).

6.1.4 PLA/SA-CNC nanocomposites through masterbatch mixing

This approach uses a miscible carrier for assisting the incorporation of CNC in PLA matrix. PEO was used as carrier for CNC since it is miscible with PLA at higher concentrations. PEO-CNC masterbatches were prepared using the procedure described in section 3.4.2 and were melt processed with the PLA. The room temperature miscibility of PEO and PLA reduces with an increase in PEO molecular weight. It is reported that for PEO molecular weight of 400 and 10,000 g/mol, the miscibility limits were 30 and 15 wt.% respectively [131, 132]. PEO with molecular weight of 1000 gm/mol was used in this research, and its 10 wt.% concentration with respect to PLA in final nanocomposites was well within miscibility range. As expected, the dispersion state of CNC in this case has improved remarkably compared to other methods as shown in Figure 6.7. Fewer aggregates of CNC with size ~ 1 µm were observed.

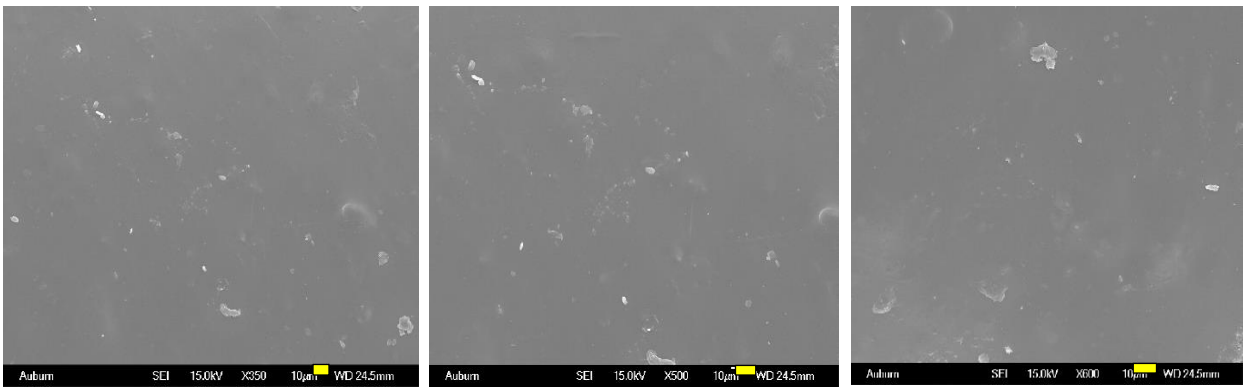

Figure 6.7. SEM images for 8 wt.% PLA/PEO/SA-CNC. (scale bars-10 µm)

6.1.5 PLA/SA-CNC nanocomposites through solution processing

Solution processing has been widely used method for making PLA/CNC nanocomposites but it may not be a viable option in an industrial setting. Solution processed PLA/CNC nanocomposites were produced in this research to compare its dispersion state and properties with melt-processed nanocomposites produced using various promising pre-processing techniques. Solution processing is expected to give a highly uniform dispersion state since the CNC and PLA are initially solubilized in a common solvent followed by a uniform mutual mixing. The detailed solution processing procedure is explained in section 3.4.3. As shown in Figure 6.8, highly uniform dispersion state was observed for 8 wt.% solution processed PLA/SA-CNC with only few aggregates of the size ~ 1 µm.

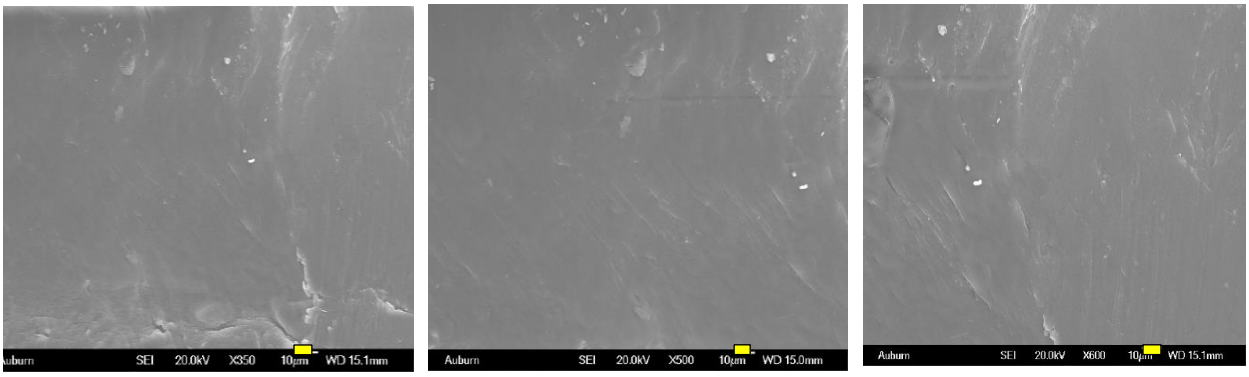

Figure 6.8. SEM images of 8 wt.% PLA/SA-CNC nanocomposite prepared using solution processing. (scale bars-10 µm)

6.2 Rheology

Rheological characterization was performed to provide an insight into the dispersion state of CNC in PLA matrix and nanocomposite microstructure. Also, it was a useful and sensitive tool for detecting degradation caused during processing of moisture-sensitive polymers.

PLA is a condensation polymer, susceptible to hydrolytic degradation from residual moisture and thermal degradation at higher temperatures. Thermal stability for PLA was checked by performing repeated amplitude sweep tests at 190 $^{\circ}$C for the duration of 75 minutes (equivalent to 4 tests) shown in Figure 6.9. A 15 minutes' time interval between the tests was provided for the sample relaxation. The change in storage modulus was monitored to determine the level of degradation in PLA.

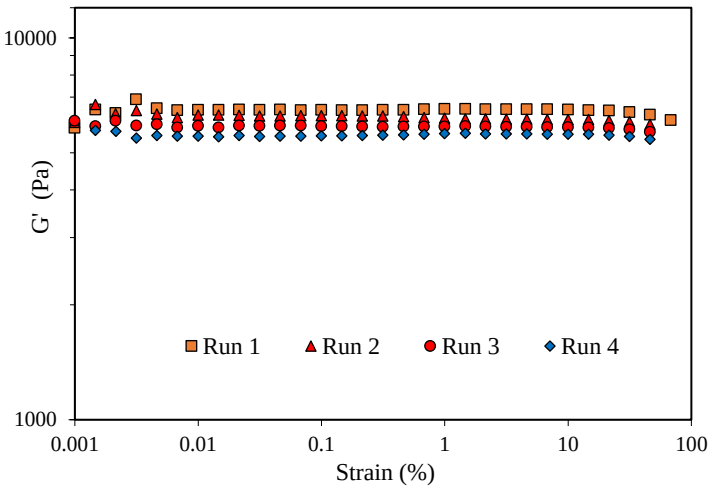

Figure 6.9. Amplitude sweep runs for the PLA pellets performed in air at 190 ˚C and angular frequency of 10 s^{-1}.

The storage modulus of PLA pellets was decreased by 15% percent over the period of 75 minutes indicating the degradation of PLA. This time duration was equivalent to the time required for carrying out all rheological tests on a sample load of PLA nanocomposite. Hence, the average error in rheological properties of PLA nanocomposites was expected to be higher due to degradation of PLA over time. Inert medium was tried instead of air in order to reduce any possible oxidative degradation but as shown in Figure 6.10, complex viscosity of 8 wt.% PLA/L-CNC in presence of inert medium was not significantly different from air medium and lied within 4% limit. Also, use of inline dessicator and vacuum drying of samples before rheology runs reduced the possibility of hydrolytic degradation. Hence the observed decrease in storage modulus can be attributed to poor thermal stability of PLA. Interestingly, the degree of change in storage modulus from repeated amplitude sweep runs as the result of thermal degradation did not correlate with the variations in thermal properties. Thermal degradation temperature and the temperature of maximum rate of weight% loss did not vary for PLA pellets before and after rheology runs.

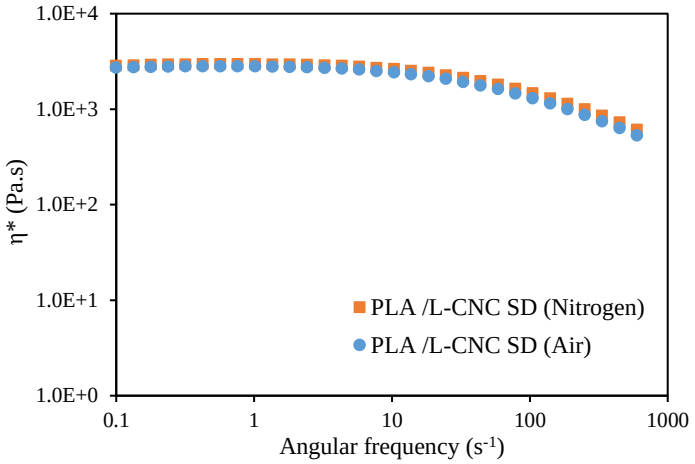

Figure 6.10. Complex viscosity (η*) vs Angular frequency for 8 wt.% PLA/L-CNC (spray dried) nanocomposite under nitrogen and air mediums.

Different methods employed in this research for incorporating CNC into PLA matrix were compared based on rheological behavior of the resulting nanocomposites. Rheological behavior of PLA nanocomposites correlated to their dispersion states except for 8 wt.% PLA/PEO/SA-CNC, where PEO has plasticizing effect. Complex viscosity as a function of frequency is shown in Figure 6.11(a). All nanocomposites except 8 wt.% PLA/PEO/SA-CNC exhibited a non-Newtonian behavior characterized by plateau regime of viscosity at a low frequency up to 10 s^{-1} which was followed by power law drop in viscosity at higher frequencies. In the case of 8 wt.% PLA/PEO/SA-CNC plateau regime was longer extending until an angular frequency of ~ 450 s^{-1} due to presence of 10 wt.% low molecular weight PEO which increased the linear viscoelastic limit of PLA. With reference to neat PLA, complex viscosity of 8 wt.% PLA/SA-CNCSD did not increase because of poorly dispersed CNC in the form of compact aggregates. Similar behavior was reported by Khoshkava et al. [27] in the case of 5 wt.% PLA/CNC nanocomposites prepared from spray dried and freeze dried CNC, where complex viscosity of nanocomposites remain unchanged compared

to neat PLA. However, ~80% increase in complex viscosity of 8 wt.% PLA/SA-CNCFD found in this research might be because of the rapid freezing of CNC/water dispersion in liquid nitrogen unlike slow freezing carried out by Khoshkava et al. [133]. This change in freezing rate reduced the aggregation induced by ice crystal formation. For 8 wt.% PLA/SA-CNCSFD, the highest increase in complex viscosity ~170% was found due to the uniform dispersion of CNC in PLA resulted from easily dispersible porous and weak CNC agglomerates. Complex viscosity of nanocomposites prepared using masterbatches of PEO-CNC diminished by an order of magnitude compared to neat PLA due to plasticization caused by PEO. Free volume inside the nanocomposite increased in presence of PEO, lowering friction between the PLA chains.

Frequency sweep for PLA showed a classical viscoelastic behavior of polymer melts where in a low-frequency regime G" > G', with G" and G' having a linear and square dependence on angular frequency, respectively. In Figure 6.11 (b) neat PLA represents an expected terminal behavior also the 8 wt.% PLA/SA-CNCSD and PLA/SA-CNCFD showed similar behavior as neat PLA suggesting poorly dispersed CNC without any interconnected network. Whereas 8wt.% PLA/SA-CNCSFD showed an order of magnitude increase in storage modulus indicating more uniform dispersion of CNC approaching percolation.

Using similar processing conditions for 7 wt.% PLA and spray freeze dried CNC nanocomposites, Khoshkava et al [27] have observed about four orders of magnitude increase in storage modulus. An order of magnitude increase in this case can be attributed to the low thermal stability of sulfonated CNC. For 8 wt.% PLA/PEO/SA-CNC storage modulus' values remained lower than those for neat PLA and showed a weak dependence on angular frequency (which extended until larger frequency values) because of plasticizing effect of PEO.

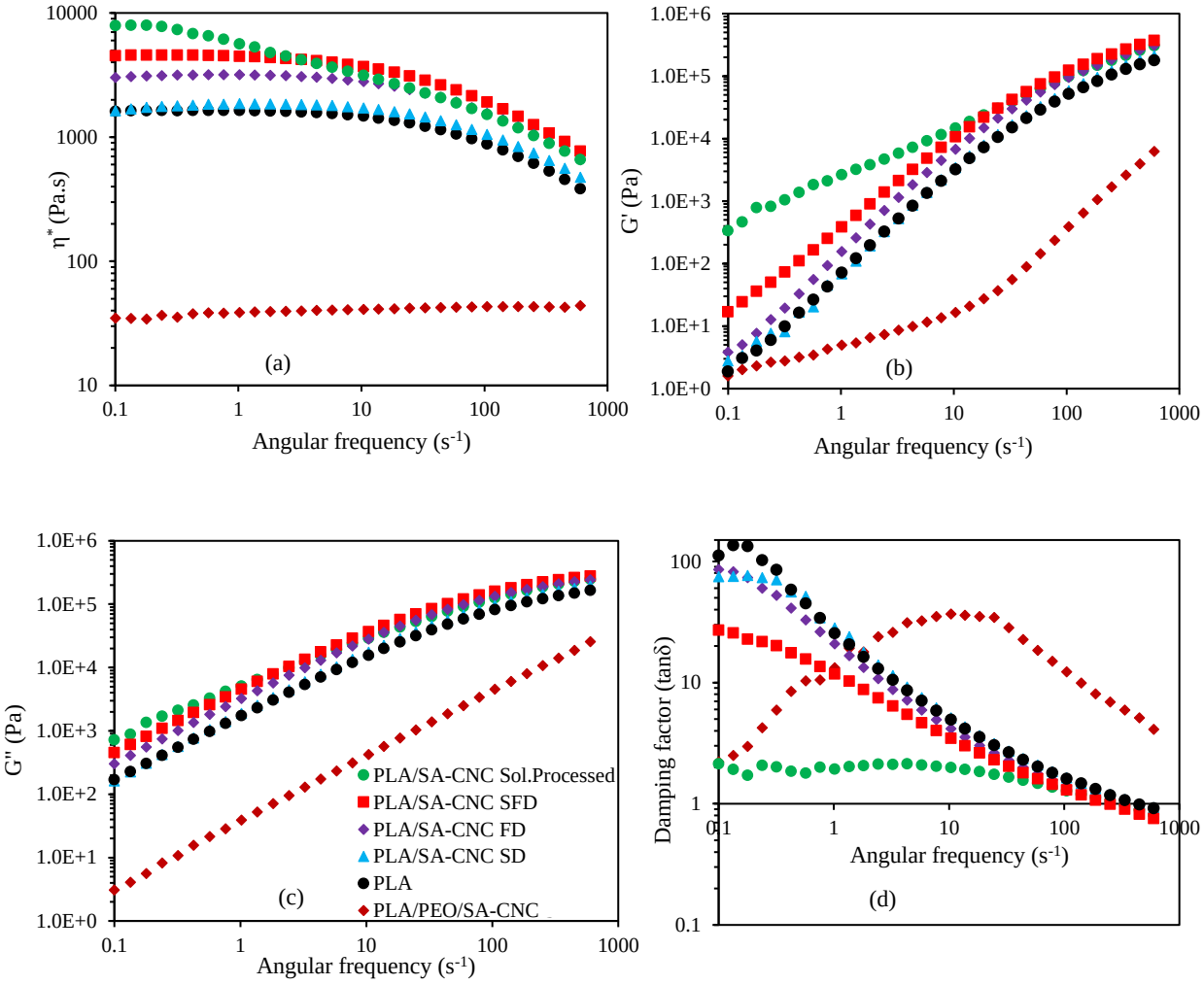

Figure 6.11. (a) Complex Viscosity, (b) Storage modulus, (c) Loss modulus, and (d) Damping factor as a function of angular frequency. Legends shown in 6.11(c) (same for all figures). (Error bars < 20%)

Damping factor versus frequency plot were shown in Figure 6.11 (d). The transition from liquid-like to solid-like behavior occurs at the crossover frequency (ω_c) at which damping factor equals 1. The inverse of this crossover frequency is equivalent to the characteristic relaxation time of the polymer chains (λ_c) [134]. For the PLA matrix ω_c and λ_c were 440 s^{-1} and 0.002 s,

respectively. The crossover frequency decreased to 225 s^{-1} for 8 wt.% PLA/SA-CNCSFD, indicated that the presence of CNC has significantly retarded polymer chain relaxation. For 8 wt.% PLA/PEO/SA-CNC, no crossover frequency was seen as the liquid-like behavior dominated in entire frequency range tested.

6.3 Thermal properties

CNC did not improve the thermal stability of PLA, instead, a decrease in the thermal degradation temperature (T_d) of PLA was observed upon incorporating CNC. As shown in Figure 6.12, more weight loss occurred for nanocomposites than neat PLA due to the decomposition of CNC by itself; this effect was prominent for PLA/SA-CNC due to the presence of acid sulfate groups which have lower thermal stability. Interestingly, PLA/SA-CNC have shown more thermal stability at temperatures higher than ~350 ^oC as seen from the TGA plots in Figure 6.13.

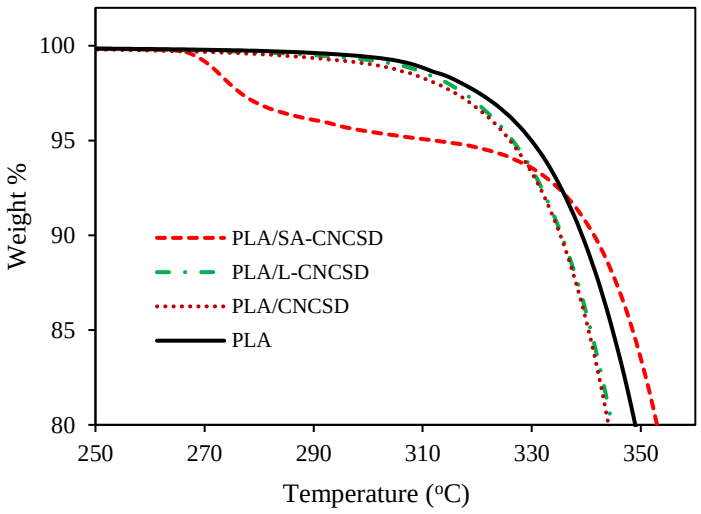

Figure 6.12. TGA curves for 8 wt.% PLA nanocomposites using different spray dried CNC.

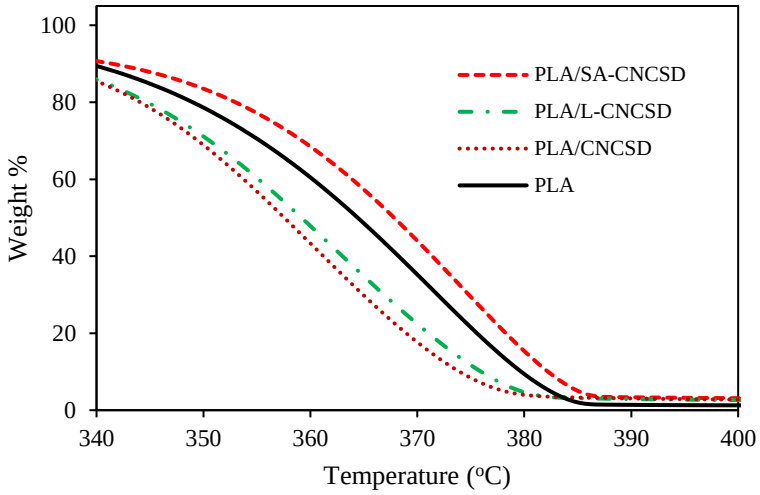

Figure 6.13**.** TGA curves for 8 wt.% PLA nanocomposites using different spray dried CNC.

Thermal degradation temperature (T_d) of 8 wt.% PLA/SA-CNCSD was reduced from 331 °C for neat PLA to 312 °C, whereas 8 wt.% PLA/CNCSD and 8 wt.% PLA/L-CNCSD did not show significant loss in weight as their observed T_d were 326 °C and 327 °C, respectively as shown in Table 6.1. Derivative weight (%/°C) vs temperature plots in Figure 6.14, clearly illustrates distinct peaks corresponding to various weight loss events. Also, peak temperatures from such plots are more sensitive to the decomposition behavior of the samples [135]. All nanocomposites have a peak between 320 °C to 400 °C which corresponds to significant weight loss of PLA and CNC. However, in the case of 8 wt.% PLA/SA-CNCSD, an additional peak corresponding to the decomposition of sulfate groups can be found in the lower temperature range between 260 °C to 280 °C.

Sample	5%weight loss temperature (T_d)	Temperature of maximum rate of weight% loss
PLA	331	372
PLA/L-CNCSD	327	362
PLA/SA-CNCSD	312	374
PLA/CNCSD	326	361

Table 6.1. T_d and temperature of maximum rate of weight% loss for 8 wt.% PLA nanocomposites using different spray dried CNC.

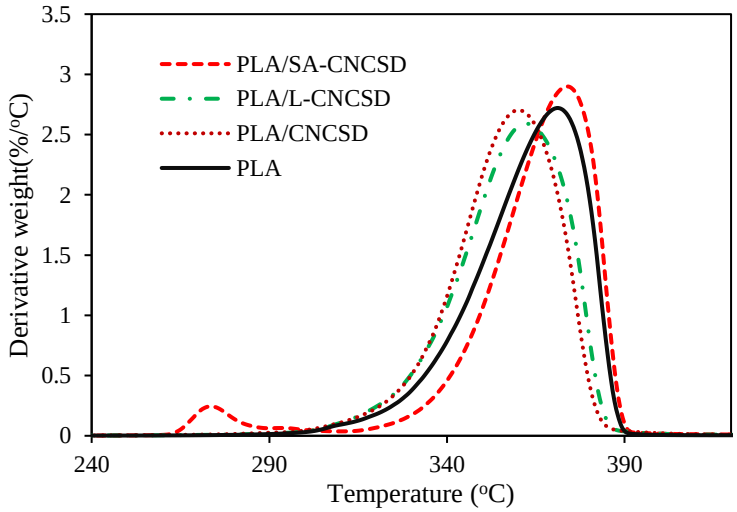

Figure 6.14. Derivative weight (%/°C) vs Temperature plots for 8 wt.% PLA nanocomposites using different spray dried CNC.

Thermal properties of 8 wt.% PLA/SA-CNC nanocomposites using different pre-processing methods were tabulated in Table 6.2. Interestingly, the T_d of the 8 wt.% PLA/SA-CNCSFD, 8 wt.% PLA/PEO/SA-CNC and solution processed 8 wt.% PLA/SA-CNC have further reduced compared to 8 wt.% PLA/SA-CNCSD. This might be due to the enhanced rate of the degradation of sulfate groups resulting from its more uniform dispersion state inside the PLA

matrix. However, the temperature of maximum rate of weight % loss was not significantly affected indicating that the presence of CNC did not have any effect on PLA thermal stability.

Sample	5% weight loss temperature	Temperature of maximum rate of weight% loss
PLA	331	372
PLA/SA-CNCSFD	294	374
PLA/PEO/SA-CNC	304	369
PLA/SA-CNC Sol.Processed	295	370

Table 6.2. T_d and temperature of maximum rate of weight% loss for 8 wt.% PLA nanocomposites using different pre-processing methods.

As shown in Table 6.3, the cold crystallization (crystallization upon heating) temperature (T_{cc}) of 8 wt.% PLA nanocomposites was increased for solution processed 8 wt.% PLA/SA-CNC and 8 wt.% PLA/SA-CNCSFD, however 8 wt.% PLA/PEO/SA-CNC has lower T_{cc} than the neat PLA. Since the overall crystallization is governed by the competition between the nucleation effect and polymer chain mobility during crystalline growth. The observed change of cold crystallization behavior in PLA nanocomposites indicated the polymer chain mobility to be dominating factor responsible for crystallization than the nucleation effect of SA-CNC. Presence of PEO increased the PLA chain mobility thus reduced its $T_{cc,}$ whereas presence of 8 wt.% SA-CNC reduced the mobility thereby increasing $T_{cc.}$ Similar behavior was observed in case of PLA/PEO/graphene nanoplatelets by Chieng et al.[136]. The presence of CNC has also increased the crystallite size which was seen from a slight improvement in percent crystallinity of nanocomposites. Glass transition temperature was influenced by the restriction in the chain mobility and showed a small increase in T_g for all nanocomposites except 8 wt.% PLA/PEO/SA-

CNC where a decrease in T_g was observed due to the plasticization effect of PEO. The melting temperature of nanocomposites was not affected by the presence of CNC.

Sample	**T_g (°C)**	**T_{cc} (°C)**	**T_m (°C)**	**H_m (J/g)**	**H_{cc} (J/g)**	**X_c (%)**
PLA	58.5	114	148	28.8	26.0	3.0
PLA/SA-CNCSFD	60.0	118	149	25.6	21.4	4.8
PLA/PEO/SA-CNC	42.4	93	150	24.7	29.4	6.0
PLA/SA-CNC Sol.Processed	60.1	121	149	22.5	18.7	4.4

Table 6.3. Transition temperatures, enthalpies and percent crystallinity of 8 wt.% PLA/SA-CNC nanocomposites.

Isothermal cold crystallization kinetics of PLA nanocomposites was studied at 4 different temperatures using avrami equation. Parameters obtained from this analysis are tabulated in Table 6.4. Avrami exponent (n) for PLA and its nanocomposites was between 2 and 3, indicating spherulitic morphology of the PLA crystals. Half time of crystallization (i.e., time required for 50% crystallization) was increased by adding 8 wt.% SA-CNCSFD. For example, at 90°C half time for 8 wt.% PLA/SA-CNCSFD was increased by 48 seconds while it has drastically decreased in case of 8 wt.% PLA/PEO/SA-CNC. Half time for crystallization was only 44 seconds for 8 wt.% PLA/PEO/SA-CNC which has PEO to SA-CNC ratio of 1.25 (by weight). Presence of 8 wt.% SA-CNC generated more nucleation sites for crystallization, however it has reduced the PLA chain mobility thus lowering the rate of cold crystallization process in 8 wt.% PLA/SA-CNCSFD. This effect was less prominent at higher temperatures due to increased polymer chain mobility. In 8 wt.% PLA/PEO/SA-CNC, PEO acted as a plasticizer and increased the free volume inside the PLA

matrix. This reduced the friction between the PLA polymer chains resulting in their easy movement during crystallization thereby achieving higher crystallization rate.

Sample	Temperature	n	k	$t_{0.5}$ (sec)
PLA	90	2.2	3.10E-06	251
	95	2.4	2.30E-06	192
	100	2.4	3.50E-06	158
	105	2.4	7.20E-06	132
PLA/SA-CNCSFD	90	2.1	3.70E-06	299
	95	2.3	1.90E-06	238
	100	2.2	6.20E-06	179
	105	2.2	1.10E-05	139
PLA/PEO/SA-CNC	90	3	8.50E-06	44
	95	2.7	4.20E-05	35
	100	2.6	9.62E-05	33
	105	2.3	2.39E-04	31

Table 6.4. Crystallization kinetic parameters for the 8 wt.% PLA nanocomposites.

6.4 Conclusions

A direct comparison carried out for PLA/SA-CNC nanocomposites prepared from pre-processing methods such as spray drying, freeze drying, spray freeze drying, and master-batch mixing showed considerable differences between the morphology, thermal and rheological properties of final nanocomposites. Among different pre-processing methods spray freeze drying and masterbatch mixing methods have resulted in more uniform dispersion states. Rheological characterizations showed that 8 wt.% PLA/SA-CNCSFD nanocomposites had given an order of magnitude increase in storage modulus as well a noticeable enhancement in the complex viscosity compared to the neat PLA, however, the complex viscosity and storage modulus of 8 wt.% PLA/PEO/SA-CNC nanocomposites were reduced significantly due to the plasticization effect of PEO.

Nanocomposites prepared using spray drying and freeze drying methods showed a similar rheological behavior as neat PLA due to their poor dispersion states as evident from morphology. Uniform dispersion of SA-CNC in nanocomposites through spray freeze drying and masterbatch mixing method influenced the crystallization behavior of PLA. Crystallization rate of 8 wt.% PLA/SA-CNCSFD was reduced due to reduction in polymer chain mobility in presence of SA-CNC, whereas in case of 8 wt.% PLA/PEO/SA-CNC this effect was dominated by plasticizing effect of PEO which enhanced the polymer chain mobility and hence the crystallization rate. Moreover, the thermal stability of neat PLA was deteriorated by the incorporation of SA-CNC.

It is evident that use of thermally stable CNC is crucial in achieving the maximum increase in thermal and rheological properties of PLA nanocomposites. Choice of relatively more thermally stable CNC (unmodified CNC and Lignin coated CNC) is limited by their poor dispersion state in solvents but perhaps functionalization of their surface in conjunction with spray freeze drying method can maximize the thermal as well as the rheological properties of PLA. Also masterbatch mixing method using lower quantities of PEO along with thermally stable CNC might also be a promising option to explore in future studies.

Chapter 7

Conclusions

This research has shown the importance of pre-processing methods and non-covalent functionalization for effectively dispersing SWNT and CNC through melt processing. The poor dispersion state of SWNT achieved in melt processed polymer nanocomposites was largely due to their aggregation during pre-processing and incompatibility with the polymer matrix. While compatibility can be improved using surface modification of SWNT through non-covalent functionalization, a poor SWNT dispersion state in final nanocomposites persists due to their aggregation during pre-processing. Rotary evaporation is one of the promising methods for incorporation of SWNT compared to dry mixing. It has resulted in uniform SWNT dispersion in PP matrix, while showing an unexpectedly higher aggregation for non-covalently functionalized SWNT. This type of aggregation was the result of capillary and van der Waal forces which pulls nanotube bundles together during drying, forming bigger agglomerates. Spray freeze drying in this case was proved to be an effective drying (pre-processing) method, since porous and low agglomerate strength spray freeze dried nanotube bundles were easily dispersed due to melt infiltration and applied shear during processing. Thus, the initial uniform dispersion state in non-covalently functionalized SWNT dispersion was successfully translated to final PP and EVOH nanocomposites consequently achieving maximum improvement in their thermal and rheological

properties. PLA/CNC nanocomposites prepared using various promising methods has further reinforced the effectiveness of spray freeze drying over other methods such as spray drying, freeze drying and masterbatch mixing. Moreover, the rheological and thermal properties of PLA nanocomposites prepared using spray freeze drying closely followed the solution processed nanocomposites with a similar loading. It was also observed that the extent of changes in rheological properties of nanocomposites did not necessarily correlate with the changes in their thermal stability. This might be due to differences in the thermal stability of dispersing agents and/or nanomaterials. The thermal stability of neat polymer can even deteriorate due to poor thermal stability of nanomaterials as was seen for PLA/SA-CNC nanocomposites.

The results of this research show that spray freeze drying method results in a more uniform dispersion state than the other pre-processing methods. However, it should be noted that this investigation used a relatively low shear extruder without distributive or dispersive mixing elements. Using spray freeze drying method in conjunction with thermally stable, non-covalently functionalized nanomaterials can be even more promising for producing melt processed nanocomposites. Such an approach is helpful for future research in order to achieve the greatest improvements in thermal, rheological and mechanical properties of thermoplastic polymer nanocomposites.

References

1. Ibeh, C.C., *Thermoplastic materials: properties, manufacturing methods, and applications*. 2011: CRC Press.
2. Avérous, L., *Polylactic acid: synthesis, properties and applications*. 2008: Elsevier: Oxford, UK.
3. Moore, E.P., *Polypropylene handbook: polymerization, characterization, properties, processing, applications*. 1996: Hanser.
4. Hamad, K., et al., *Properties and medical applications of polylactic acid: A review.* Express Polymer Letters, 2015. **9**(5): p. 435-455.
5. Zhao, J., et al., *Permeability of EVOH Barrier Material Used in Automotive Applications: Metrology Development for Model Fuel Mixtures.* Oil & Gas Science and Technology–Revue d'IFP Energies nouvelles, 2015. **70**(2): p. 353-366.
6. Karger-Kocsis, J., *Polypropylene: an AZ reference*. Vol. 2. 2012: Springer Science & Business Media.
7. *http://www.matterhackers.com/3d-printer-filament-compare*.
8. Moritomi, S., T. Watanabe, and S. KANZAKI, *Polypropylene compounds for automotive applications.* R&D Report, Sumimoto Kagaku, 2010. **2010**: p. 1-16.
9. P Pawar, R., et al., *Biomedical applications of poly (lactic acid).* Recent Patents on Regenerative Medicine, 2014. **4**(1): p. 40-51.
10. Hongling, Y., et al., *Nanosilica and Polyethylene Based Artificial Turf-abrasion Resistance and Mechanical Properties.* Procedia Engineering, 2014. **72**: p. 901-906.
11. *http://www.statista.com/statistics/203398/total-us-resin-production-from-2008/*.
12. Martínez-Abad, A., J.M. Lagaron, and M.J. Ocio, *Development and characterization of silver-based antimicrobial ethylene–vinyl alcohol copolymer (EVOH) films for food-packaging applications.* Journal of agricultural and food chemistry, 2012. **60**(21): p. 5350-5359.
13. Delimoy, D. and P. De Longree, *Multilayer composites coextruded with the use of impact-reinforced impervious resin compositions and their use for the manufacture of fuel storage vessels*, 1993, Google Patents.
14. Auras, R.A., et al., *Poly (lactic acid): synthesis, structures, properties, processing, and applications*. Vol. 10. 2011: John Wiley & Sons.
15. Lunt, J., *Large-scale production, properties and commercial applications of polylactic acid polymers.* Polymer degradation and stability, 1998. **59**(1): p. 145-152.
16. Radhakrishnan, V.K., *Structure-Processing-Property Interrelationships of Vapor Grown Carbon Nanofiber, Single-Walled Carbon Nanotube and Functionalized Single-Walled Carbon Nanotube–Polypropylene Nanocomposites*, 2010, Auburn University.
17. Manchado, M.L., et al., *Thermal and mechanical properties of single-walled carbon nanotubes–polypropylene composites prepared by melt processing.* Carbon, 2005. **43**(7): p. 1499-1505.
18. Dondero, W.E. and R.E. Gorga, *Morphological and mechanical properties of carbon nanotube/polymer composites via melt compounding.* Journal of Polymer Science Part B: Polymer Physics, 2006. **44**(5): p. 864-878.
19. Fornes, T., et al., *Morphology and properties of melt-spun polycarbonate fibers containing single-and multi-wall carbon nanotubes.* Polymer, 2006. **47**(5): p. 1704-1714.

20. Lee, S.H., et al., *Rheological and electrical properties of polypropylene composites containing functionalized multi-walled carbon nanotubes and compatibilizers.* Carbon, 2007. **45**(14): p. 2810-2822.
21. Sung, Y., et al., *Rheological and electrical properties of polycarbonate/multi-walled carbon nanotube composites.* Polymer, 2006. **47**(12): p. 4434-4439.
22. O'Connell, M.J., et al., *Reversible water-solubilization of single-walled carbon nanotubes by polymer wrapping.* Chemical Physics Letters, 2001. **342**(3): p. 265-271.
23. Kayatin, M.J., *Chemical Functionalization of Single-walled Carbon Nanotubes for Compatibilization with Unsaturated Polyester Resin*, 2012, Auburn University.
24. Arias, A., et al., *Enhanced dispersion of cellulose nanocrystals in melt-processed polylactide-based nanocomposites.* Cellulose, 2015. **22**(1): p. 483-498.
25. Radhakrishnan, V.K., E.W. Davis, and V.A. Davis, *Influence of initial mixing methods on melt-extruded single-walled carbon nanotube–polypropylene nanocomposites.* Polymer Engineering & Science, 2010. **50**(9): p. 1831-1842.
26. Radhakrishnan, V.K., V.A. Davis, and E.W. Davis, *The Effect of Melt Extrusion Process Parameters on Rotary-Evaporated Poly (propylene) Nanocomposites.* Macromolecular Materials and Engineering, 2012. **297**(9): p. 864-874.
27. Kamal, M.R. and V. Khoshkava, *Effect of cellulose nanocrystals (CNC) on rheological and mechanical properties and crystallization behavior of PLA/CNC nanocomposites.* Carbohydrate polymers, 2015. **123**: p. 105-114.
28. Iijima, S., *Helical microtubules of graphitic carbon.* Nature, 1991. **354**(6348): p. 56-58.
29. Monthioux, M. and V.L. Kuznetsov, *Who should be given the credit for the discovery of carbon nanotubes?* Carbon, 2006. **44**(9): p. 1621-1623.
30. Radushkevich, L. and V. Lukyanovich, *O strukture ugleroda, obrazujucegosja pri termiceskom razlozenii okisi ugleroda na zeleznom kontakte.* Zurn Fisic Chim, 1952. **26**(1): p. 88-95.
31. Kim, P., et al., *Thermal transport measurements of individual multiwalled nanotubes.* Physical review letters, 2001. **87**(21): p. 215502.
32. Che, J., T. Cagin, and W.A. Goddard III, *Thermal conductivity of carbon nanotubes.* Nanotechnology, 2000. **11**(2): p. 65.
33. Baughman, R.H., A.A. Zakhidov, and W.A. de Heer, *Carbon nanotubes--the route toward applications.* Science, 2002. **297**(5582): p. 787-792.
34. Krishnan, A., et al., *Young's modulus of single-walled nanotubes.* Physical Review B, 1998. **58**(20): p. 14013.
35. Yu, M.-F., et al., *Tensile loading of ropes of single wall carbon nanotubes and their mechanical properties.* Physical review letters, 2000. **84**(24): p. 5552.
36. Walters, D., et al., *Elastic strain of freely suspended single-wall carbon nanotube ropes.* Applied Physics Letters, 1999. **74**(25): p. 3803-3805.
37. Saito, R., et al., *Electronic structure of chiral graphene tubules.* Applied Physics Letters, 1992. **60**(18): p. 2204-2206.
38. Wilder, J.W., et al., *Electronic structure of atomically resolved carbon nanotubes.* Nature, 1998. **391**(6662): p. 59-62.
39. White, C.T. and T.N. Todorov, *Quantum electronics: Nanotubes go ballistic.* Nature, 2001. **411**(6838): p. 649-651.
40. Ouyang, M., et al., *Energy gaps in" metallic" single-walled carbon nanotubes.* Science, 2001. **292**(5517): p. 702-705.

41. Louie, S.G., *Electronic properties, junctions, and defects of carbon nanotubes*, in *Carbon Nanotubes*. 2001, Springer. p. 113-145.
42. Habibi, Y., L.A. Lucia, and O.J. Rojas, *Cellulose nanocrystals: chemistry, self-assembly, and applications.* Chemical reviews, 2010. **110**(6): p. 3479-3500.
43. Lu, P. and Y.-L. Hsieh, *Preparation and properties of cellulose nanocrystals: rods, spheres, and network.* Carbohydrate polymers, 2010. **82**(2): p. 329-336.
44. Siqueira, G., J. Bras, and A. Dufresne, *Luffa cylindrica as a lignocellulosic source of fiber, microfibrillated cellulose and cellulose nanocrystals.* BioResources, 2010. **5**(2): p. 727-740.
45. Fortunati, E., et al., *Effects of modified cellulose nanocrystals on the barrier and migration properties of PLA nano-biocomposites.* Carbohydrate polymers, 2012. **90**(2): p. 948-956.
46. Gårdebjer, S., A. Bergstrand, and A. Larsson, *A mechanistic approach to explain the relation between increased dispersion of surface modified cellulose nanocrystals and final porosity in biodegradable films.* European Polymer Journal, 2014. **57**: p. 160-168.
47. George, J. and S. Sabapathi, *Cellulose nanocrystals: synthesis, functional properties, and applications.* Nanotechnology, science and applications, 2015. **8**: p. 45.
48. *http://www.pire-renew.com/wind-energy.html*
49. *http://www.statista.com/statistics/320430/leading-polypropylene-producing-regions/.*
50. Zhang, S. and A.R. Horrocks, *A review of flame retardant polypropylene fibres.* Progress in Polymer Science, 2003. **28**(11): p. 1517-1538.
51. Natta, G., et al., *Crystalline high polymers of α-olefins.* Journal of the American Chemical Society, 1955. **77**(6): p. 1708-1710.
52. Cowie, J.M.G. and V. Arrighi, *Polymers: chemistry and physics of modern materials*. 2007: CRC press.
53. Maier, C. and T. Calafut, *Polypropylene: the definitive user's guide and databook*. 1998: William Andrew.
54. Klein, E., V. Lukes, and Z. Cibulková, *On the energetics of phenol antioxidants activity.* Petrol Coal, 2005. **47**: p. 33-9.
55. *Kuraray Co. Ltd. (2011). EVAL EVOH Resins Technical Brochure.*
56. *Ethylene-Vinyl Alcohol Resins. (2011). Chemical Insight and Forecasting: HIS Chemical.*
57. *Properties and medical applications of polylactic acid.*
58. Drumright, R.E., P.R. Gruber, and D.E. Henton, *Polylactic acid technology.* Advanced Materials, 2000. **12**(23): p. 1841-1846.
59. Ma, P.-C., et al., *Dispersion and functionalization of carbon nanotubes for polymer-based nanocomposites: a review.* Composites Part A: Applied Science and Manufacturing, 2010. **41**(10): p. 1345-1367.
60. Girifalco, L., M. Hodak, and R.S. Lee, *Carbon nanotubes, buckyballs, ropes, and a universal graphitic potential.* Physical Review B, 2000. **62**(19): p. 13104.
61. O'connell, M.J., et al., *Band gap fluorescence from individual single-walled carbon nanotubes.* Science, 2002. **297**(5581): p. 593-596.
62. Hersam, M.C., *Progress towards monodisperse single-walled carbon nanotubes.* Nature Nanotechnology, 2008. **3**(7): p. 387-394.
63. Hirsch, A., *Functionalization of single-walled carbon nanotubes.* Angewandte Chemie International Edition, 2002. **41**(11): p. 1853-1859.
64. Backes, C., *Noncovalent functionalization of carbon nanotubes: Fundamental aspects of dispersion and separation in water*. 2012: Springer Science & Business Media.

65. Nepal, D. and K.E. Geckeler, *Proteins and carbon nanotubes: close encounter in water.* Small, 2007. **3**(7): p. 1259-1265.
66. Zheng, M., et al., *DNA-assisted dispersion and separation of carbon nanotubes.* Nature materials, 2003. **2**(5): p. 338-342.
67. Nakashima, N., Y. Tomonari, and H. Murakami, *Water-Soluble Single-Walled Carbon Nanotubes via Noncovalent Sidewall-Functionalization with a Pyrene-Carrying Ammonium Ion.* Chemistry Letters, 2002(6): p. 638-639.
68. Wenseleers, W., et al., *Efficient isolation and solubilization of pristine single-walled nanotubes in bile salt micelles.* Advanced Functional Materials, 2004. **14**(11): p. 1105-1112.
69. Chen, Z., W. Thiel, and A. Hirsch, *Reactivity of the Convex and Concave Surfaces of Single-Walled Carbon Nanotubes (SWCNTs) towards Addition Reactions: Dependence on the Carbon-Atom Pyramidalization.* ChemPhysChem, 2003. **4**(1): p. 93-97.
70. Pötschke, P., T. Fornes, and D. Paul, *Rheological behavior of multiwalled carbon nanotube/polycarbonate composites.* Polymer, 2002. **43**(11): p. 3247-3255.
71. Chen, J., et al., *Dissolution of full-length single-walled carbon nanotubes.* The Journal of Physical Chemistry B, 2001. **105**(13): p. 2525-2528.
72. Chen, J., et al., *Solution properties of single-walled carbon nanotubes.* Science, 1998. **282**(5386): p. 95-98.
73. Banerjee, S., T. Hemraj-Benny, and S.S. Wong, *Covalent surface chemistry of single-walled carbon nanotubes.* Advanced Materials, 2005. **17**(1): p. 17-29.
74. Liang, F., et al., *A convenient route to functionalized carbon nanotubes.* Nano Letters, 2004. **4**(7): p. 1257-1260.
75. Banerjee, S., T. Hemraj-Benny, and S.S. Wong, *Covalent Surface Chemistry of Single-Walled Carbon Nanotubes.* Advanced Materials, 2005. **17**(1): p. 17-29.
76. Braun, B. and J.R. Dorgan, *Single-step method for the isolation and surface functionalization of cellulosic nanowhiskers.* Biomacromolecules, 2008. **10**(2): p. 334-341.
77. Sobkowicz, M.J., B. Braun, and J.R. Dorgan, *Decorating in green: surface esterification of carbon and cellulosic nanoparticles.* Green Chemistry, 2009. **11**(5): p. 680-682.
78. Goussé, C., et al., *Stable suspensions of partially silylated cellulose whiskers dispersed in organic solvents.* Polymer, 2002. **43**(9): p. 2645-2651.
79. de Menezes, A.J., et al., *Extrusion and characterization of functionalized cellulose whiskers reinforced polyethylene nanocomposites.* Polymer, 2009. **50**(19): p. 4552-4563.
80. Lafuente, E., et al., *Polyazomethine/carbon nanotube composites.* Materials Science and Engineering: C, 2006. **26**(5): p. 1198-1201.
81. Funck, A. and W. Kaminsky, *Polypropylene carbon nanotube composites by in situ polymerization.* Composites Science and Technology, 2007. **67**(5): p. 906-915.
82. Zeng, J., et al., *Processing and properties of poly (methyl methacrylate)/carbon nano fiber composites.* Composites Part B: Engineering, 2004. **35**(2): p. 173-178.
83. Abu-Zurayk, R., et al., *Biaxial deformation behavior and mechanical properties of a polypropylene/clay nanocomposite.* Composites Science and Technology, 2009. **69**(10): p. 1644-1652.
84. Jiang, X. and L.T. Drzal, *Multifunctional high density polyethylene nanocomposites produced by incorporation of exfoliated graphite nanoplatelets 1: Morphology and mechanical properties.* Polymer composites, 2010. **31**(6): p. 1091-1098.

85. Moore, A.L., et al., *Thermal conductivity measurements of nylon 11-carbon nanofiber nanocomposites.* Journal of Heat Transfer, 2009. **131**(9): p. 091602.
86. Kamal, M. and V. Khoshkava, *SPRAY FREEZE-DRIED NANOPARTICLES AND METHOD OF USE THEREOF*, 2015, US Patent 20,150,307,692.
87. Cheow, W.S., et al., *Spray-freeze-drying production of thermally sensitive polymeric nanoparticle aggregates for inhaled drug delivery: effect of freeze-drying adjuvants.* International journal of pharmaceutics, 2011. **404**(1): p. 289-300.
88. Wang, Z., et al., *Powder formation by atmospheric spray-freeze-drying.* Powder Technology, 2006. **170**(1): p. 45-52.
89. Maa, Y.-F., et al., *Protein inhalation powders: spray drying vs spray freeze drying.* Pharmaceutical Research, 1999. **16**(2): p. 249-254.
90. Khoshkava, V. and M. Kamal, *Effect of drying conditions on cellulose nanocrystal (CNC) agglomerate porosity and dispersibility in polymer nanocomposites.* Powder Technology, 2014. **261**: p. 288-298.
91. *http://mashable.com/category/3d-printing/*.
92. *http://3dprintingfromscratch.com/common/types-of-3d-printers-or-3d-printing-technologies-overview/*
93. Kataura, H., et al., *Optical properties of single-wall carbon nanotubes.* Synthetic metals, 1999. **103**(1): p. 2555-2558.
94. Grossiord, N., et al., *Time-dependent study of the exfoliation process of carbon nanotubes in aqueous dispersions by using UV-visible spectroscopy.* Analytical chemistry, 2005. **77**(16): p. 5135-5139.
95. Bhattacharyya, A.R., et al., *Crystallization and orientation studies in polypropylene/single wall carbon nanotube composite.* Polymer, 2003. **44**(8): p. 2373-2377.
96. Valentini, L., et al., *Effects of carbon nanotubes on the crystallization behavior of polypropylene.* Polymer Engineering & Science, 2004. **44**(2): p. 303-311.
97. Sahoo, N.G., et al., *Effect of functionalized carbon nanotubes on molecular interaction and properties of polyurethane composites.* Macromolecular chemistry and physics, 2006. **207**(19): p. 1773-1780.
98. Smith, E. and G. Dent, *Modern Raman spectroscopy: a practical approach*. 2013: John Wiley & Sons.
99. Basu-Dutt, S., et al., *Chemistry of Carbon Nanotubes for Everyone.* Journal of Chemical Education, 2011. **89**(2): p. 221-229.
100. Souza Filho, A., et al., *Raman spectroscopy for probing chemically/physically induced phenomena in carbon nanotubes.* Nanotechnology, 2003. **14**(10): p. 1130.
101. Kharchenko, S.B., et al., *Flow-induced properties of nanotube-filled polymer materials.* Nature materials, 2004. **3**(8): p. 564-568.
102. Huang, Y., S. Ahir, and E. Terentjev, *Dispersion rheology of carbon nanotubes in a polymer matrix.* Physical Review B, 2006. **73**(12): p. 125422.
103. Pötschke, P., T.D. Fornes, and D.R. Paul, *Rheological behavior of multiwalled carbon nanotube/polycarbonate composites.* Polymer, 2002. **43**(11): p. 3247-3255.
104. Celzard, A., et al., *Critical concentration in percolating systems containing a high-aspect-ratio filler.* Physical Review B, 1996. **53**(10): p. 6209.
105. Vehring, R., *Pharmaceutical particle engineering via spray drying.* Pharmaceutical Research, 2008. **25**(5): p. 999-1022.
106. *Mini Spray Dryer B-290 Technical data sheet.*

107. *http://www.natureworksllc.com/~/media/Technical_Resources/Processing_Guides/ProcessingGuide_Crystallizing-and-Drying_pdf.pdf.*
108. Fortunati, E., et al., *Microstructure and nonisothermal cold crystallization of PLA composites based on silver nanoparticles and nanocrystalline cellulose.* Polymer degradation and stability, 2012. **97**(10): p. 2027-2036.
109. Fortunati, E., et al., *Combined effects of cellulose nanocrystals and silver nanoparticles on the barrier and migration properties of PLA nano-biocomposites.* Journal of Food Engineering, 2013. **118**(1): p. 117-124.
110. Zhang, Q., et al., *Low percolation threshold in single-walled carbon nanotube/high density polyethylene composites prepared by melt processing technique.* Carbon, 2006. **44**(4): p. 778-785.
111. Wajid, A.S., et al., *Polymer-stabilized graphene dispersions at high concentrations in organic solvents for composite production.* Carbon, 2012. **50**(2): p. 526-534.
112. Thill, A. and O. Spalla, *Aggregation due to capillary forces during drying of particle submonolayers.* Colloids and Surfaces A: Physicochemical and Engineering Aspects, 2003. **217**(1): p. 143-151.
113. Krause, S. and P.-P. Compatibility, *Polymer Blends 1*, 1978, Academic Press, New York.
114. Van Krevelen, D.W. and K. Te Nijenhuis, *Properties of polymers: their correlation with chemical structure; their numerical estimation and prediction from additive group contributions*. 2009: Elsevier.
115. Xu, D.-H., Z.-G. Wang, and J.F. Douglas, *Influence of carbon nanotube aspect ratio on normal stress differences in isotactic polypropylene nanocomposite melts.* Macromolecules, 2008. **41**(3): p. 815-825.
116. Marosfői, B., et al., *Thermal and spectroscopic characterization of polypropylene-carbon nanotube composites.* Journal of thermal analysis and calorimetry, 2006. **86**(3): p. 669-673.
117. Kashiwagi, T., et al., *Thermal degradation and flammability properties of poly (propylene)/carbon nanotube composites.* Macromolecular rapid communications, 2002. **23**(13): p. 761-765.
118. Yang, J., et al., *Thermal reduced graphene based poly (ethylene vinyl alcohol) nanocomposites: enhanced mechanical properties, gas barrier, water resistance, and thermal stability.* Industrial & Engineering Chemistry Research, 2013. **52**(47): p. 16745-16754.
119. Kim, S.W. and H.M. Choi, *Enhancement of thermal, mechanical, and barrier properties of ethylene vinyl alcohol copolymer by incorporation of graphene nanosheets effect of functionalization of graphene oxide.* High Performance Polymers, 2015. **27**(6): p. 694-704.
120. Kim, S.W. and S.H. Cha, *Thermal, mechanical, and gas barrier properties of ethylene–vinyl alcohol copolymer-based nanocomposites for food packaging films: Effects of nanoclay loading.* Journal of Applied Polymer Science, 2014. **131**(11).
121. Cassu, S.N. and M.I. Felisberti, *Poly (vinyl alcohol) and poly (vinyl pyrrolidone) blends: miscibility, microheterogeneity and free volume change.* Polymer, 1997. **38**(15): p. 3907-3911.
122. Feng, H., Z. Feng, and L. Shen, *A high resolution solid-state nmr and dsc study of miscibility and crystallization behaviour of poly (vinyl alcohol) poly (N-vinyl-2-pyrrolidone) blends.* Polymer, 1993. **34**(12): p. 2516-2519.

123. Zhang, X., K. Takegoshi, and K. Hikichi, *High-resolution solid-state 13 C nuclear magnetic resonance study on poly (vinyl alcohol)/poly (vinylpyrrolidone) blends.* Polymer, 1992. **33**(4): p. 712-717.
124. Ping, Z.H., Q.T. Nguyen, and J. Néel, *Investigations of poly (vinyl alcohol)/poly (N-vinyl-2-pyrrolidone) blends, 1. Compatibility.* Die Makromolekulare Chemie, 1989. **190**(2): p. 437-448.
125. Zhang, X., et al., *Poly (vinyl alcohol)/SWNT composite film.* Nano Letters, 2003. **3**(9): p. 1285-1288.
126. Kanagaraj, S., et al., *Mechanical properties of high density polyethylene/carbon nanotube composites.* Composites Science and Technology, 2007. **67**(15): p. 3071-3077.
127. Shi, Q., et al., *Mechanical properties and in vitro degradation of electrospun bio-nanocomposite mats from PLA and cellulose nanocrystals.* Carbohydrate polymers, 2012. **90**(1): p. 301-308.
128. Salmieri, S., et al., *Antimicrobial nanocomposite films made of poly (lactic acid)–cellulose nanocrystals (PLA–CNC) in food applications—part B: effect of oregano essential oil release on the inactivation of Listeria monocytogenes in mixed vegetables.* Cellulose, 2014. **21**(6): p. 4271-4285.
129. Jonoobi, M., et al., *Mechanical properties of cellulose nanofiber (CNF) reinforced polylactic acid (PLA) prepared by twin screw extrusion.* Composites Science and Technology, 2010. **70**(12): p. 1742-1747.
130. Pouteau, C., et al., *Lignin–polymer blends: evaluation of compatibility by image analysis.* Comptes rendus biologies, 2004. **327**(9): p. 935-943.
131. Baiardo, M., et al., *Thermal and mechanical properties of plasticized poly (L-lactic acid).* Journal of Applied Polymer Science, 2003. **90**(7): p. 1731-1738.
132. Sheth, M., et al., *Biodegradable polymer blends of poly (lactic acid) and poly (ethylene glycol).* Journal of Applied Polymer Science, 1997. **66**(8): p. 1495-1505.
133. Khoshkava, V. and M.R. Kamal, *Effect of cellulose nanocrystals (CNC) particle morphology on dispersion and rheological and mechanical properties of polypropylene/CNC nanocomposites.* ACS applied materials & interfaces, 2014. **6**(11): p. 8146-8157.
134. Larson, R.G., *The structure and rheology of complex fluids*. Vol. 150. 1999: Oxford university press New York.
135. *http://www.tainstruments.com/pdf/literature/TA127.pdf*.
136. Chieng, B.W., et al., *Poly (lactic acid)/poly (ethylene glycol) polymer nanocomposites: effects of graphene nanoplatelets.* Polymers, 2013. **6**(1): p. 93-104.